Aus dem

Hertie Institute für klinische Hirnforschung

Influence of the glioblastoma-induced vessel-associated mural cell specific expression of the EMT-factor SLUG on tumor-neoangiogenesis – in vivo examinations

Inaugural-Dissertation
zur Erlangung des Doktorgrades
der Medizin

der Medizinischen Fakultät
der Eberhard Karls Universität
zu Tübingen

vorgelegt von

Merk, Luisa

2025

Dekan:	Professor Dr. B. Pichler
1. Berichterstatter:	Professorin Dr. U. Naumann
2. Berichterstatter:	Professorin Dr. K. Schilbach-Stückle
3. Berichterstatter:	Professorin L. Sorokin, PhD

Tag der Disputation: 21.05.2025

Table of Contents

Index of figures

List of abbreviations

%Area	Percent area
°C	Degree celsius
3D	Three-dimensional
ANG	Angiopoetin
BBB	Blood brain barrier
BM	Basement membrane
BSA	Bovine serum albumine
BW	Body weight
CD31	Endothelial cell marker
CLARITY	Clear Lipid-exchanged Acrylamide-hybridized Rigid Imaging/ Immunostaining/ in situ-hybridization-compatible Tissue hYdrogel
cm	Centimeter
CNS	Central nervous system
CO_2	Carbon dioxide
DAPI	4',6-diamidino-2-phenylindole
DBE	Dibenzylether
DCM	Dichloromethane
ddH_2O	double distilled water
DMEM	Dulbeccos Modified Eagle Medium
DMSO	Dimethylsulfoxide
DNA	Desoxyribonucleic acid
DRAQ5	DNA stain for fluorescent cellular imaging
E.coli	Escherichia coli
EANO	European Association for Neuro-Oncology
$EBM2^+$	Endothelial basal medium-2
EBSS	Earle's balanced salt solution
EC	Endothelial cell
ECM	Extracellular matrix
EGFR	Epidermal growth factor receptor
ELISA	Enzyme-linked immunosorbent assay
EMT	Epithelial-to-mesenchymal transition
ERK	Extracellular-signal regulated kinases
FCS	Fetal calf serum
GBM	Glioblastoma
GFP	Green fluorescent protein
GL261	Murine glioma cell line
GL261mCherry	Genetically modified murine glioma cell line
gRNA	Guide RNA
GTPase	family of hydrolase enzymes with specificity for the nucleotide guanosine triphosphate

h	Hour
H_2O	Water
H_2O_2	Hydrogenperoxide
HBVP	Human brain microvascular pericyte
HCl	Hydrochloric acid
HIF	Hypoxia-inducible factor
HIH	Hertie Institute for Clinical Brain Research
HIV	Human immunodeficiency virus
HM	Hydrogen monomers
i.p.	Intraperitoneal
ICAM-1	Intracellular adhesion molecule 1
IDH1	Isocitrate dehydrogenase 1
iDISCO	Immunolabeling-enabled three-dimensional imaging of solvent-cleared organs
IF	Immunofluorescence
IgG	Immunglobuline G
IHC	Immunohistochemistry
IL	Interleukin
IMDM	Iscove´s Modified Dulbecco´s Medium
IVC	Individually ventilated cages
JNK	c-Jun N-terminal kinases
KO	Knockout
KPS	Karnofsky Performance Score
Lenti-SLUG-KO	Mixture of Lenti-RGS5-CRISPR-SLUG 1, 4 and 5
Lenti-V2	Lenti-CRISPR V2
LOH	Loss of heterozygosity
LP	Lentiviral particles
LSM	Laser scanning microscope
MBVP	Murine brain vascular pericyte
MEM	Minimal Essential Medium
mg	Milligram
MGMT	O(6)-methylguanine-DNA methyltransferase
MHC	Major histocompability complex
min	Minutes
ml	Mililiter
mM	Milimolar
MMP	Matrix metalloproteinase
mRNA	Messenger RNA
MV	Microvessel
NaCl	Sodium chloride
NaN_3	Sodium acide
ng	Nanogram

NG-2	Nerve growth factor 2
NVU	Neurovascular unit
OS	Overall survival
P/S	Penicillin-streptomycin
p24	HIV protein
p38 MAP kinase	p38 mitogen-activated protein kinases
PACT	Passive clarity technique
PAR GBM	Glioblastoma developed from GL261mCherry cells
PBS	Phosphate buffered saline
PDGF-B	Platelet-derived growth factor B
PDGRFRβ	Platelet-derived growth factor receptor beta
PECAM-1	Platelet endothelial cell adhesion molecule 1
PEG	Polyethylene glycol
PFA	Paraformaldehyde
PFS	Progression free survival
pg	Picogram
PI3K	Phosphatidyl-inositol-3-kinase
PLL	Poly-L-Lysin
PTEN	Phosphatase and tensin homolog gene
RGS5	Regulator of G Protein Signaling 5
RNA	Ribonucleinacid
rpm	Rounds per minute
RT	Room temperature
s.c.	Subcutaneous
SDS	Sodium dodecyl sulfate
sgRNA	single guide RNA
SLUG	EMT transcription regulator
SLUG-KO	SLUG-Knockout
SMAD	Small worm phenotype mothers against decapentaplegic
SN	Supernatant
SNAI1	EMT-associated gene, coding for SNAIL
SNAI2	EMT-associated gene, coding for SLUG
SNAIL	EMT transcription regulator
SOC	Super optimal broth with catabolite repression
TBS	Tris-buffered saline
TBST	Tris-buffered saline with Tween20
TCGA	The Cancer Genome Atlas
TGF-β	Transforming growth factor beta
TGF-β-KO	TGFβ-1 plus TGFβ-2 knockdown
TGF-βR	Transforming growth factor beta receptor
TMZ	Temozolomide

TP53	Cellular tumor antigen p53
Twist	Basic helix loop factor
TWIST	EMT transcription regulator
UK	United Kingdom
USA	United States of America
VA-044	Polymerization initiator
VAMCs	Vessel-associated mural cells
VCAM-1	Vascular cell adhesion molecule
VEGF	Vascular endothelial growth factor
VEGFR	Vascular endothelial growth factor receptor
VP	Virus particles
VSV-G	Vesicular stomatitis virus G glycoprotein
WHO	World Health Organization
WT	Wildtype
x g	Relative centrifugal force
ZEB	Zinc Finger Homeodomain Enhancer-Binding Proteins
αSMA	Alpha smooth muscle actin
µg	Microgram
µl	Microliter
µm	Micrometer
µm	Micrometer

1 Introduction

1.1 Glioblastoma

Glioblastoma multiforme (GBM) is the most common malignant primary brain tumor in adults. Although GBM is a relatively rare tumor entity with an annual incidence of only 5-6/100.000 it accounts for 14.7 % of all primary brain and other central nervous system (CNS) tumors (Ostrom et al., 2018) with slightly higher frequency (1,2 times) in men (Sung et al., 2021; Thakkar et al., 2014). It can occur at any age, but it predominates in elderly patients with a peak incidence between the 5th and 6th decade (Hanif et al., 2017). Despite various modern therapeutic strategies, GBM remains an incurable and highly lethal disease with a very poor prognosis. The relative survival rates of GBMs are devastating, with 40.9 % of patients surviving the first year post-diagnosis and only 6,6 % surviving the first 5 years (Ostrom et al., 2021; Ostrom et al., 2018). The median survival is merely 14-15 months after diagnosis when receiving optimal treatment (Thakkar et al., 2014).

GBM is the most malignant and frequently occurring type of primary astrocytoma (Louis et al., 2021). It is an intra-axial tumor that is most commonly found intraparenchymally within the supratentorial region of the brain, particularly in the temporal, parietal and frontal lobes (Iacob & Dinca, 2009). Only 5 % of GBMs appear in the brain stem, cerebellum or spinal cord (Nakada et al., 2011). GBMs are typically unilateral tumors, often involving entire lobes. Seldomly, GBMs can invade the contralateral brain hemisphere via the corpus callosum, named “butterfly” GBM after the typical appearance of the bilateral invasion (Smith & Ironside, 2007).

1.1.1 Classification

Traditionally, CNS tumors have been classified into different subtypes and severity grades ranging from 1 to 4 (Louis et al., 2016), based on the presence or absence of four morphologic criteria: nuclear atypia, mitosis, endothelial proliferation and necrosis (Daumas-Duport et al., 1988). WHO Grade 1 gliomas show low proliferative potential and can be cured by surgical resection, whereas grade 2 to 4 gliomas are

highly malignant and invasive, showing nuclear atypia (Grade 2) and mitotic activity (Grade 3) as an indicator for a high proliferative activity (Daumas-Duport et al., 1988; Hanif et al., 2017). Glioblastoma is the most aggressive, invasive and undifferentiated type of glioma and is classified as WHO Grade 4 (Hanif et al., 2017; Louis et al., 2007). It is a heterogeneous tumor entity almost exclusively featuring endothelial proliferation and vascular abnormalities, multifocal hemorrhage and necrosis (D'Alessio et al., 2019; Daumas-Duport et al., 1988; Smith & Ironside, 2007). GBM is a highly diffuse invasive tumor whose migrating cells tend to spread along vessels, dendrites and fibers within the white matter. However, extracranial metastasis occurs only very seldomly (Nakada et al., 2011; Smith & Ironside, 2007). Additionally, GBMs are considered as immunologically cold tumors, as they possess a highly immunosuppressive microenvironment, fostering poor prognosis (D'Alessio et al., 2019; Nduom et al., 2015).

The classification of GBMs is extremely difficult, heterogeneous and changes regularly. The World Health Organization (WHO) recently updated the Glioma Classification system and included not only histological but also molecular markers into the classification of CNS tumors (Louis et al., 2021). This results in a better correlation of individual tumor biology and behavior. Furthermore, it allows for the identification of subgroups with more consistent prediction of treatment response and prognosis (Bai et al., 2020; Schulz-Schaeffer, 2016). In the case of discordant geno- and phenotype, genotype now takes precedence. Hence, gliomas with histological grade 2 or 3 can be accounted as GBM when featuring specific genetic alterations (Tesileanu et al., 2020).

GBM can generally be divided into two different types which evolve through different genetic pathways, affect patients at different ages and show different outcomes (Ohgaki & Kleihues, 2013; Thakkar et al., 2014). The more common form is the so called primary GBM (~95 %) which arises typically within 3 to 6 months and affects predominantly elderly patients (Alifieris & Trafalis, 2015). Primary GBMs develop rapidly de novo without clinical and histological evidences of less malignant precursor lesions and present as full-blown tumors at diagnosis (Ohgaki & Kleihues, 2007). The absence of IDH1 mutation, also referred as “IDH-wildtype” GBM, is very

typical for primary GBMs (Ohgaki & Kleihues, 2007; Thakkar et al., 2014). In contrast, secondary GBM only account for ~5 % of all GBM cases and progress slowly (over 10 to 15 years) from pre-existing lower-grade diffuse or anaplastic astrocytoma (Ohgaki & Kleihues, 2007; Smith & Ironside, 2007; Thakkar et al., 2014). They are typically found in younger patients. Although histologically largely undistinguishable from primary GBM, secondary GBMs differ in their genetic alterations (Ohgaki & Kleihues, 2013). IDH1-mutations are a main characteristic of secondary GBM ("IDH-mutant" GBM), associated with lower aggressiveness and a significant increase in overall survival (Brat et al., 2020; Ohgaki & Kleihues, 2013).

Besides that, GBM can be classified into four subtypes based on its´ molecular signature: the so-called classical, proneural, neural and mesenchymal subtypes with dedicated specific gene expressions and alterations are closely linked to prognosis and therapy response as described in the Cancer Genome Atlas (TCGA) (Verhaak et al., 2010). However, RNA-sequence analysis has revealed a considerable degree of intratumoral heterogeneity according to the expression of those established GBM subtypes and several other subgroups also exist (Omuro & DeAngelis, 2013; Patel et al., 2014).

1.1.2 Diagnosis and treatment

Usually, GBM is diagnosed after clinical presentation of the patients as soon as they develop first tumor-related symptoms. Unfortunately, GBM is often asymptomatic until it reaches an enormous size (Weller et al., 2017). Patients regularly present with symptoms of increased intracranial pressure, including headaches of progressing severity or neurocognitive impairments as a direct consequence of tumor growth and the surrounding edema (Davis, 2016; Hanif et al., 2017). GBMs locally destructive growth causes focal neurological deficits such as contralateral, slowly progressive hemiparesis or even partial or generalized seizures (25-50% of all patients) (Davis, 2016). Especially in tumors arising in the frontal and parietal lobes as well as in the thalamic region, motor weakness, sensory disturbances and personality changes are quite common (Iacob & Dinca, 2009).

Therefore, rapid tumor treatment is of fundamental importance. The treatment of GBM diagnosed patients consists of direct tumor treatment and additional symptomatic relief to retain the patients´ quality of life. However, a curative treatment option for high-grade gliomas is currently not available. In 2016, the European Association for Neuro-Oncology (EANO) prepared a guideline based on the WHO classification of CNS tumors that provides recommendations for the clinical care of glioma patients and guidance for diagnostic decisions (Weller et al., 2017). According to this guideline, current standard therapy for newly diagnosed GBM in patients younger than 70 years consists of maximal safe tumor resection if feasible, followed by radiotherapy with concomitant and adjuvant chemotherapy with temozolomide (TMZ) (Alifieris & Trafalis, 2015; Darefsky et al., 2012). This treatment protocol was established by Stupp et al. in 2005 and the combined modality therapy to target the remaining tumor cells after surgery results in a significant improvement in the overall survival (Rock et al., 2012; Stupp et al., 2005). Since then, multiple clinical trials investigating novel therapies were performed, but to date there have been no major additions to that treatment strategy (Poon et al., 2020). As GBMs are frequently invasive, extensive and complete surgical resection of the tumor is impossible. GBMs are often localized in important areas of the brain, including areas of speech control, motor function and senses restricting extensive surgery (Davis, 2016; Iacob & Dinca, 2009). Hence, the main goal of surgery is to improve neurological functions by removing as much tumor volume as safely possible without causing new and permanent treatment-related neurological deficits (Weller et al., 2017). Nevertheless, whenever possible, gross total resection of the tumor mass is performed to reduce tumor volume and to take biopsies for histological analysis, tumor grading and genotyping (Eigenbrod et al., 2014). Symptomatic relief can be additionally achieved by administering corticosteroids, as they effectively reduce intracranial pressure and thereby the severity of neurological symptoms as well as headaches in early-stage tumors (Nakada et al., 2011). However, due to their substantial side effects, including immunosuppression and negative impact on anti-tumor treatment, they are usually tapered off early in the treatment process (Omuro & DeAngelis, 2013). When patients suffer from tumor-related epilepsy, anti-epileptic drugs can be given to treat tumor-related seizures (Weller et al., 2017). In addition,

depending on the patients' individual needs, antidepressants, psychostimulants or acetylcholinesterase inhibitors may be administered to further improve quality of life (Tucha et al., 2000).

After initial therapy response, GBM almost universally recur following conventional therapies (in approximately 90 % of cases), usually within a 2-3 cm perimeter of the original lesion (Hanif et al., 2017; Nakada et al., 2011). So called *glioma stem-like cells* (a subpopulation of tumor cells), which are highly resistant to therapy contribute to fast tumor recurrence (Yi et al., 2016). Standards of care for recurrent GBM are not well defined. Clinical decisions are influenced by prior treatment response, extent of the disease, age and performance status as well as general medical condition (Diaz et al., 2017; Weller et al., 2017). Re-resection may be considered for certain patients, as surgical tumor reduction can ease intracranial pressure and other symptoms frequently seen at tumor recurrence, such as seizures, motor and speech deficits (Davis, 2016). However, therapy options are very limited and often, best palliative supportive care must be considered (Tan et al., 2020).

Although therapy regimens have slowly improved over the last decades, no efficacious treatment has been developed yet and improvements have not led to remarkable increases in patient survival (Alifieris & Trafalis, 2015). Unfortunately, many GBMs have intrinsic or acquired resistance to chemotherapy. The only predictive biomarker in GBM for therapy response so far is the methylation status of the promotor region of O6-methylguanine-DNA methyltransferase (MGMT) (Hegi et al., 2005). The epigenetic silencing of this DNA-repair protein is associated with a better response to alkylating chemotherapy such as nitrosoureas and TMZ and therefore correspond to an improved outcome upon TMZ treatment (Colman et al., 2010; Eigenbrod et al., 2014). As the majority of patients with recurrent disease fail to respond to TMZ and other chemotherapeutics, new therapy regimens are urgently needed (Vredenburgh et al., 2007). GBM´s heterogeneity significantly contributes to therapeutic resistance by preventing any possibility of control over the entire tumor mass through a single drug and facilitating escape mechanisms from targeted agents (Noch et al., 2018; Oberoi et al., 2015). While many new therapies show promising results with significant gains in patients with peripheral tumors, they lack

the same effects in GBM. This failure of novel drug therapy may be at least to some extent due to an inconsistent disruption of the blood-brain-barrier (BBB) within the tumor area (Parrish et al., 2015). The inconsistent BBB disruption results in partially impeded and partially undisturbed drug delivery into the tumor. As the majority of new treatment agents is therefore unable to reach a constant adequate penetration of the intact BBB without dose-limiting systemic side-effects, therapy success is restricted (Guerra et al., 2018). In addition, GBMs highly immunosuppressive characteristics propose a major hurdle. It possesses several mechanisms of immune evasion promoting tumor progression and impair successful treatment, including secretion of immunosuppressive cytokines, upregulation of immune checkpoint molecules, activation of regulatory T-cells, down-regulation of MHC molecules and many more (Gieryng et al., 2017).

Various promising novel targeted therapies have been evaluated for treating GBM recurrence over the last decades, including cytotoxic chemotherapy, angiogenesis inhibitors, receptor tyrosine kinase inhibitors, oncolytic virotherapy and immunotherapies like checkpoint inhibitors or tumor-vaccines among others (Diaz et al., 2017; Huang et al., 2020). The aim of these targeted therapies has been to affect and inhibit tumor-specific features, such as altered signaling pathways, abnormal vascularization and impaired anticancer immune response. However, all of the tested agents have failed to show significant clinical benefit thus far (Alifieris & Trafalis, 2015).

To date, the only approved targeted drug for the treatment of recurrent GBM is a single antiangiogenic agent, bevacizumab (Avastin®), a humanized IgG1 monoclonal antibody against vascular endothelial growth factor A (VEGF-A) (Polivka et al., 2017). Bevacizumab reduces angiogenic processes during tumor growth and therefore leads to a temporal vascular “normalization” with improved blood flow and oxygenation as well as reduced vascular permeability and edema (Cohen et al., 2009; Xiao et al., 2018). However, after initial response to treatment with bevacizumab, GBM frequently show enhanced invasiveness and fast tumor progression (Kumar & Arbab, 2013; Narayana et al., 2009). In comparison to standard therapy, there is no improvement in overall survival, although bevacizumab

results in a prolongation of progression-free survival as well as in an overall lowering of glucocorticoid requirements to control tumor related edema (Ameratunga et al., 2018; Gilbert et al., 2014). The use of bevacizumab in GBM treatment is controversial and its use has to be individually evaluated (Davis, 2016). According to the European Association of Neuro-Oncology (EANO), bevacizumab can be used in case of progression or recurrence of glioma either alone or in combination with cytotoxic chemotherapy, but immunotherapies are currently not recommended in clinical routine (Barthel et al., 2022).

1.2 Blood-Brain-Barrier within GBM

Proper neuronal function requires a precise control of the CNS microenvironment, as neuronal signaling within the CNS relies on a combination of electrical and chemical signals (Abbott et al., 2010; Daneman et al., 2010). The BBB is an anatomical and biochemical barrier at the level of brain microvessel endothelium, that protects the brain from potentially harmful substances in the systemic circulation and tightly regulates the movements of ions, molecules and cells between the blood and the brain (Abbott et al., 2010; Daneman & Prat, 2015; Oberoi et al., 2015; Profaci et al., 2020).

The brain´s microvasculature is composed of three cell types: endothelial cells (EC), adjacent pericytes and astrocytes. The latter extend polarized cellular processes (“astrocytic endfeet”), ensheating either neuronal processes or the vascular tube (Daneman & Prat, 2015; Jain et al., 2007). Together with the basement membrane, these cells form the neurovascular unit that constitutes the complex BBB (Jain et al., 2007). Its´ unique ability to selectively restrict the exchange of molecules between the intra- and extracerebral circulatory system plays a crucial role in the maintenance of brain homeostasis and the prevention of toxic injury to the brain, albeit also limiting drug delivery into the brain parenchyma (Jackson et al., 2017). However, the BBB is not static. Instead it may be seen as a dynamic interface that is not only influenced by vascular but also from parenchyma signals (Carvey et al., 2009). The BBB is capable of responding to local changes and adapting to local requirements by

regulating endothelial cell morphology, changing the expression and activity of transporters and enzymes or tight junction function (Abbott et al., 2010). Alterations of these barrier properties are an important component of pathology and progression of different neurological diseases as well as brain tumors (Daneman & Prat, 2015). The normally impermeable BBB is more likely to be disrupted in high-grade gliomas (Diaz et al., 2017; Thanabalasundaram et al., 2010). The BBB-disruption results in ion dysregulation, vasogenic cerebral edema and neuroinflammation, which in turn can lead to increased intracranial pressure, neuronal dysfunction and neuronal degradation (Bradbury, 1993; Profaci et al., 2020).

1.3 Angiogenesis

Tissue growth and function depend on vascularization to ensure oxygen and nutrient supply as well as the disposal of carbon dioxide and metabolic waste that accumulate during metabolism (Liu & Ouyang, 2013). Angiogenesis describes the formation of new blood vessels from pre-existent ones, mainly from capillaries and small venules (Wesseling et al., 1997). Different processes like endothelial intussusception, endothelial cell bridging and vessel sprouting participate in angiogenesis (Bergers & Song, 2005). Therefore, angiogenesis is a complex process, including multiple coordinated steps that require the participation of various cell types and associated molecular signaling (Birbrair et al., 2014; Wesseling et al., 1997). In general, various angiogenic factors, mainly VEGF, stimulate vessel sprouting processes (Gilbert et al., 2014). As initial response to VEGF, endothelial cells differentiate, proliferate and start secreting several proteases (mainly matrix-metalloproteinases [MMPs], serine proteases [plasminogen activators] and cathepsins) to degrade the vessel basement membrane and the interstitial matrix (Hardee & Zagzag, 2012; Holash et al., 1999). This proteolytic degradation results in dilated and leaky vessels and allows invasion of ECs and adjacent pericytes into the surrounding extracellular matrix (ECM) (Bergers & Song, 2005). Vessel sprouting starts with the formation of a “migration column” consisting of proliferating and migrating ECs. At the very tip of the outgrowing EC column, there is a guiding EC which moves towards the VEGF gradient. Newly formed vessel sprouts adhere to

each other and create a new lumen-containing vessel (Gerhardt et al., 2003). The distinction between physiological and pathological angiogenesis lies in the disturbance of the tightly regulated balance of pro- and antiangiogenic factors, even though pathological angiogenesis per se follows the same mechanisms (Bergers & Song, 2005; Hardee & Zagzag, 2012).

1.3.1 Neovascularization within GBM

One of the defining pathological characteristics of GBM is its high angiogenesis ability and the resultant abundant aberrant vascular structure (Sun et al., 2014). Throughout GBM proliferation and invasion, tumor cells require increased vascular supply to meet their metabolic demands (Jackson et al., 2017). As an initial step, tumor cells use pre-existing vessels for their blood supply and organize into cuffs around normal brain vessels, so called vascular co-option. With progressing tumor growth, co-opted vessels undergo involution processes resulting in hypoxia of the surrounding tissue and massive tumor cell necrosis (Holash et al., 1999). As a compensatory response, the remaining tumor cells, especially those situated close to necrotic areas, drastically upregulate pro-angiogenic factors in a shift towards an angiogenic phenotype (Hosono et al., 2017). Hypoxia caused by excessive tumor growth with subsequent inadequate blood supply serves as another major local stimulus of angiogenesis in GBM. Hypoxia induces EC activation, proliferation and vessel sprouting processes via hypoxia-inducible transcription factor HIF-1α stabilization with subsequent activation of VEGF (Hardee & Zagzag, 2012; Kerbel, 2008). The stimulation of microvascular cell proliferation, combined with a relative lack of directional migration due to the overall high VEGF-expression, results in the formation of coiled “glomeroid-shaped” microvascular proliferations instead of delicate vascular sprouts as in physiological angiogenesis (Smith & Ironside, 2007; Wesseling et al., 1997). This leads to an abnormal vascular network with chaotic, poorly organized, tortuous and irregular shaped vessels unable to provide sufficient and effective perfusion (Bergers & Song, 2005; Hardee & Zagzag, 2012). The loss of normal artery-capillary-venule hierarchy and the exhibition of arteriovenous shunts results in impaired perfusion and hypoxia which in turn paradoxically supports

tumor progression by promoting a vicious cycle of inefficient but extensive neo-angiogenesis (Martin et al., 2019). Due to persistent angiogenic stimuli, vessel maturation and basal lamina formation are impeded (Hosono et al., 2017). As a result, tumor vessels show increased cellular fenestrations as well as widened intercellular gaps, resulting in vessel-leakiness and breakdown of the BBB (Sun et al., 2014). Subsequently, the vessel-leakiness causes vasogenic edema peritumorally which is a major cause of morbidity in GBM patients (Jackson et al., 2017). Birner et al. postulated, that there are distinct vascular subtypes within the newly formed tumor vessels. More “capillary-like” microvessels can be distinguished from a vascular pattern comprising mainly glomeroid-/garland-like, bizarre vascular formations. GBMs with more regular vascular structures showed significantly better survival. This leads to the conclusion that not the neovascularization itself, but the amount of unfunctional, irregular vessels is the determining factor for clinical outcome in patients with GBM, as non-uniformal blood flow and differences in the delivery of oxygen, nutrients and also therapeutical drugs further promote tumor progress (Birner et al., 2003; Sun et al., 2014).

Besides angiogenesis and vascular co-opting, various other processes have been discussed to participate in GBM´s neo-angiogenesis. GBM-to-EC transdifferentiation (Ricci-Vitiani et al., 2010) and vasculogenesis, a process where endothelial progenitor cells migrate from the bone marrow into the tumor area, have also been described. All of these mechanisms are not independent from each other, but rather interlinked and controlled by similar processes (Hardee & Zagzag, 2012). Recently, another cell type has been identified to strongly influence angiogenic processes in physiological and pathologic conditions: Pericytes.

1.4 Pericytes

1.4.1 Pericyte function under physiological conditions

Pericytes are vascular associated mural cells (VAMCs) adjacent to ECs of blood microvessels, that can be found around precapillary arterioles, capillaries, postcapillary venules and collecting venules (Armulik et al., 2005). Pericytes appear

to be present in most tissues (Thomas, 1999). Nonetheless, the pericyte coverage of the endothelium varies in between different tissues, depending on the vascular bed (Armulik et al., 2005) and correlates with endothelial barrier properties (Zhang et al., 2020). The highest pericyte coverage around microvessels is found in the CNS with around 80% of cerebral capillary surface (Daneman et al., 2010; Gerhardt & Betsholtz, 2003; Krueger & Bechmann, 2010). Pericytes surround ECs on their abluminal surface and are completely enclosed by the vascular basement membrane (Figure 1). One layer separates the pericytes from the ECs and one compartmentalizes the pericytes from the neurovascular unit (Armulik et al., 2005; Fisher, 2009). Pericytes are morphologically characterized by a flat, oval cell body and stellate appearance with long cytoplasmic protrusions parallel to the vessel axis (Fisher, 2009; Thomas, 1999). However, depending on their differentiation state, their morphology can vary (Zhang et al., 2020).

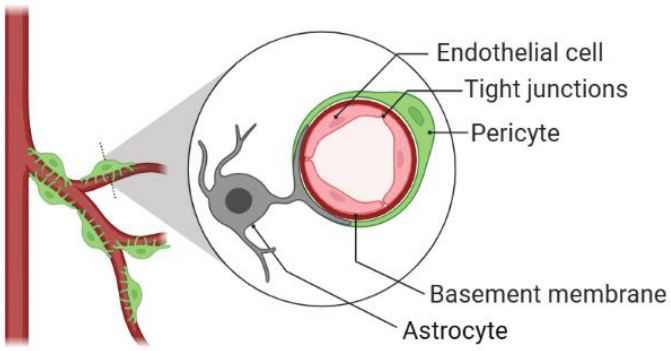

Figure 1: Structure of a normal brain vessel. *Pericytes surround endothelial cells on their abluminal surface. Together with the basement membrane and astrocytes, they form the BBB. Created with BioRender.com.*

Each pericyte surrounds and is in contact with several ECs. By extending to more than one capillary, pericytes are also able to integrate signals along vessels (Armulik et al., 2005). Pericytes and ECs display multiple cell-cell interactions, including adhesion plaques that anchor pericytes to ECs, direct physical contact via so called peg-socked contacts and gap junctions enabling the exchange of ions and small molecules (Thomas, 1999). This indicates a tightly regulated reciprocal paracrine signaling and functional coupling between ECs and pericytes, which is important to maintain vessel integrity and function (Carmeliet & Jain, 2011; Winkler et al., 2010).

During angiogenesis, activated ECs secrete platelet-derived growth factor (PDGF-B), which binds to the platelet-derived growth factor receptor beta (PDGFRβ) on pericytes. This results in the promotion of migration and proliferation of pericytes along the newly formed vessel (Mäe et al., 2021; Stenzel et al., 2009). The importance of the PDGF-B mediated signaling is highlighted by the fact that PDGF-B/ PDGFRβ deficient mice develop abnormal and immature vasculature as well as vascular defects like microaneurysms due to impaired pericyte recruitment (Hellström et al., 2001).

However, pericytes have also been shown to guide sprouting processes by migrating ahead of ECs (Bergers & Song, 2005). They can form endothelium-free tubes that provide guidance for the subsequent penetration of ECs, thereby determining the direction of sprout formation and influencing sprout connection (Nehls et al., 1992; Ozerdem & Stallcup, 2003). Pericyte deficiency has been shown to be the main cause of microvascular dysfunction, correlating with endothelial hyperplasia, increased capillary diameter, abnormal EC shape and ultrastructure, changed cellular distribution of junctional proteins and increased trans-endothelial permeability (Gerhardt & Betsholtz, 2003; Lindahl et al., 1997).

Since their discovery by Rouget in 1873, pericyte functions have been conversely discussed. Although mainly associated with vascular development, maturation and remodeling, pericytes are much more diverse in their functions, which remain to be fully elucidated (Sena et al., 2018; Thanabalasundaram et al., 2011).

Additional to their involvement in the development of vascular structures, pericytes play a critical role in the formation and maintenance of the BBB (Jackson et al., 2017). They promote endothelial stabilization, differentiation and barrier formation and also regulate transendothelial vesicle trafficking (Winkler et al., 2011). By secretion of various cytokines like Ang-1, VEGF and transforming growth factor (TGF)-β, pericytes are able to influence inter-endothelial connections and therefore modify vascular permeability (Ribatti et al., 2011; Sweeney & Foldes, 2018). Furthermore, pericytes contribute to basal membrane integrity by secreting components like collagen IV, laminin and glycosaminoglycans, all of which are

important for maintaining vessel function and the establishment of the BBB (Hellström et al., 2001; Ribatti et al., 2011). The extent of pericyte coverage inversely correlates with the relative vessel permeability (Daneman et al., 2010).

Similar to smooth-muscle cells of larger vessels, pericytes influence the vascular diameter thus regulating capillary blood flow in reaction to vasoactive substances, effectively linking blood flow to the tissue's metabolic state (Attwell et al., 2016; Rucker et al., 2000). Their contractile function relies mainly on one contractile protein, alpha smooth muscle actin (αSMA), that enables the regulation of blood supply by altering the vessel diameter (Thomas, 1999; Wesseling et al., 1997).

Moreover, pericytes are significantly involved in CNS immune mechanisms by modulating the immune-microenvironment (Sweeney et al., 2016). They express molecules associated with the control of immune cell trafficking such as vascular cell adhesion molecule VCAM-1 and intracellular adhesion molecule ICAM-1 and also secrete prostaglandins and other proinflammatory cytokines important for the attraction and activation of innate leukocytes (Jackson et al., 2017; Thomas, 1999). Additionally, pericytes have been reported to possess numerous macrophagic markers such as leukocyte-common antigen, Fc receptor and class 1 and 2 major histocompatibility complex molecules (MHC) thereby serving as antigen-presenting cells and exhibiting macrophage-like activities (Guerra et al., 2018). They are capable of phagocytosis and pinocytosis, cleaning the extracellular fluid of toxic cellular byproducts (Pieper et al., 2014; Sattiraju & Mintz, 2019).

Pericytes are a very heterogeneous cell population (Birbrair et al., 2014) originating from the mesoderm (Gerhardt & Betsholtz, 2003; Thomas, 1999). They are pluripotent cells with stem cell properties, able to differentiate into distinct cellular populations along the mesenchymal or the neuronal lineage (Caspani et al., 2014; Gerhardt & Betsholtz, 2003; Thanabalasundaram et al., 2011). Therefore, pericytes exhibit self-regenerating capacities and also participate in tissue repair processes (Armulik et al., 2005; Sweeney & Foldes, 2018; Zhang et al., 2020).

However, the secure distinction of pericytes from other cell types can be difficult. Although pericytes are defined by their anatomical perivascular position and tend to

be localized over endothelial tight junctions and capillary branch points, not all perivascular cells are pericytes (Fisher, 2009; Gerhardt & Betsholtz, 2003; Sena et al., 2018). Pericytes can be more specifically characterized by their individual protein expression. Various markers have been used to identify pericytes (Krueger & Bechmann, 2010), including αSMA (Nehls & Drenckhahn, 1991), desmin (Nehls et al., 1992), nerve growth factor 2 (NG-2) (Ozerdem et al., 2001), PDGFRβ (Lindahl et al., 1997), aminopeptidase N (Kunz et al., 1994) and the regulator of G-protein signaling-5 (RGS5) (Bondjers et al., 2003). None of these brain pericyte markers is specific, since their expression is dynamic and may differ in a tissue-specific manner or be contingent upon the developmental or angiogenic stage of the blood vessel (Bergers & Song, 2005). However, when used in combination, they are able to distinguish pericytes from other cell types (Guerra et al., 2018).

1.4.2 Pericytes role in tumor progression

Under pathological conditions, such as GBM, pericytes are involved in a variety of processes associated with tumor progression, invasiveness, recurrence and therapy resistance. They are mainly essential for GBM growth by being functional and critical contributors to tumor angiogenesis as well as by manipulating the anti-tumoral immune response (Bergers & Song, 2005; Caspani et al., 2014).

The tumor vasculature frequently exhibits structural and functional abnormalities with irregular pericytes on endothelial tubes (Cheng et al., 2013). With increasing glioma grade, the pericyte density on microvessels shows a rising tendency. It has been shown that most of the microvascular cells express the pericyte markers αSMA and PDGFRβ, while EC markers are only confined to the monolayer lining cells. This demonstrates that pericyte numbers increase drastically during tumor progression whereas the number of vascular ECs remains stable. Therefore, pericytes and not ECs are the main cells that constitute the multiplicity and altered morphology of tumor microvessels (Hosono et al., 2017; Sun et al., 2014). This indicates a guiding role of local pericytes in angiogenic processes contributing to the hyperplastic phenotype of microvessels in high grade gliomas (Hosono et al., 2017; Sun et al.,

2014). Nevertheless, pericyte coverage of tumor vessels is variable. GBMs also contain a substantial proportion of blood vessels lacking pericyte coverage in contrast to the excessive coverage seen in other tumor regions (Bergers & Song, 2005; Zhou et al., 2017). This partial dissociation contributes to increased and inhomogeneous vascular permeability intratumorally (Ribatti et al., 2011).

Interestingly, the pericyte coverage of the tumor vasculature is inversely correlated with GBM patient survival after chemotherapy (Zhou et al., 2017). Tumor vessels with less pericyte coverage appear to be more vulnerable to radiation and chemotherapy, suggesting that pericytes are critical to protect ECs and promote therapeutic resistance (Bergers & Song, 2005; Guerra et al., 2018).

In addition, GBM malignancy proceeds through specific interactions of tumor cells with pericytes through actin-based cytoplasmatic extensions, so called flectopodia. This interaction is not only associated with vessel formation and co-option, but also with an impaired innate immune response against the tumor (Caspani et al., 2014). Subsequent to GBM cell-mediated stimulation, pericytes develop an immunosuppressive phenotype, including secretion of high levels of anti-inflammatory cytokines, inhibition of T-cell function and local immunosuppression, thereby facilitating GBM progression (Ochs et al., 2013; Sena et al., 2018).

1.5 Epithelial-to-mesenchymal transition

Epithelial-to-mesenchymal transition (EMT) is a complex cellular process in which biochemical alterations lead to the acquisition of a transient and reversible mesenchymal phenotype (Kahlert et al., 2013; Moustakas & Heldin, 2014). This phenotype is characterized by increased motility, invasiveness and elevated synthesis of ECM components that are able to degrade the limiting basement membrane (Kahlert et al., 2013). Physiologically, this is a process involved in embryonal development, formation of new tissues and wound healing (Kubelt et al., 2015). The EMT program comprises different molecular and cellular changes resulting in reduced cell-cell adhesion, apical-basolateral polarity and epithelial marker expression along with the acquisition of a spindle-cell shape, increased

expression of mesenchymal markers and enhanced motility (Moustakas & Heldin, 2014). It is well known that TGF-β-signaling is an important inducer of the EMT program (Fuxe & Karlsson, 2012; Liu et al., 2014). TGF-β is a pleiotropic cytokine with multiple functions such as regulating cell proliferation, differentiation, survival and scar formation (Rustenhoven et al., 2016). It fulfills these functions through the binding of its active form to transforming growth factor beta receptors (TGF-βR) 1,2 and 3, serin/threonine kinase receptors that initiate signal transduction pathways (Rustenhoven et al., 2016). The TGF-β-binding leads to the formation of heterotetrametric receptor complexes followed by phosphorylation of the TGF-βR1. The phosphorylated TGF-βR1 then transmits intracellular signaling mainly through Small worm phenotype Mothers Against Decapentaplegic (SMAD)-mediated canonical signaling (Pickup et al., 2013). Therefore, the active receptor initiates downstream signaling through phosphorylation of the r-SMAD transducer proteins SMAD2 and SMAD3. They subsequently form complexes with SMAD 4 (co-SMAD), which then translocate into the nucleus and act as transcriptional regulators (Miyazono et al., 2012; Pickup et al., 2013). This results in a SMAD-dependent induction of multiple transcription factors, including the Zinc Finger Homeodomain Enhancer-Binding Proteins (ZEB) 1 and ZEB 2, the zinc finger proteins SNAIL and SLUG and the basic helix loop factor TWIST (Miyazono et al., 2012). It is known that epithelial markers such as E-cadherin, occludin and claudin are directly transcriptionally repressed subsequent to the binding of SLUG to E-box motifs, whereas the expression of mesenchymal proteins like N-cadherin, fibronectin and vitronectin is indirectly activated (Bolós et al., 2003; Cano et al., 2000; Hajra et al., 2002; Huang et al., 2019; Ikenouchi et al., 2003). Although most of the TGF-β signaling is mediated via SMAD-dependent signaling (Roy et al., 2015), TGF-β also activates various non-SMAD-dependent signaling pathways such as ERK, JNK, p38 MAP kinases and phosphatidyl-inositol-3-kinase (PI3K) as well as small GTPase pathways (Katsuno et al., 2013; Moustakas & Heldin, 2005). These pathways show crosstalk at multiple levels to provide context-dependent outcomes (Derynck & Zhang, 2003; Xu et al., 2009). TGF-β therefore plays a key role in tissue homeostasis and cancer development as it can result both in tumor suppression and promotion

during cancer progression depending on cell-type and interaction with other signaling pathways (Akhurst & Hata, 2012; Platten et al., 2001).

1.5.1 EMT in GBM

Due to GBM´s fast cell proliferation and highly invasive properties, it was supposed that EMT-like processes contribute to GBM progression (Mahabir et al., 2014). Two of the three isoforms of the EMT-inducing factor TGF-β (namely TGF-β1 and TGF-β2), are secreted in large quantities by most GBM cells (Liu et al., 2014; Roy et al., 2015). Whereas TGF-β is known to be anti-proliferative in non-neoplastic tissues and acts tumor suppressive in pre-malignant states, it is a prominent pro-tumorigenic cytokine in advanced tumors that have selectively lost the capacity to respond to TGF-β signals with proliferation inhibition (Bruna et al., 2007; Han et al., 2015; Joseph et al., 2013; Yamada et al., 1995). Additionally, TGF-β mediated changes in gene expression profile alter cell polarity and cell-cell adhesion, thereby enhancing the migratory capacity which favors invasive behavior of cancer cells (De Craene et al., 2005; Kubelt et al., 2015; Moreno-Bueno et al., 2008). It has been shown that high expression levels of TGF-β and EMT-associated genes in GBM is associated with increased malignancy, hence related to a poor outcome (Liu et al., 2014; Roy et al., 2015). Interestingly, the observed increase in the mRNA-expression levels of the EMT-associated genes SNAI1 (coding for SNAIL), SNAI2 (coding for SLUG) and TWIST was mainly localized to the vasculature and the perivascular areas (Dieterich et al., 2012; Elias et al., 2005; Yang et al., 2010). In accordance to those findings, SLUG expression is also notably elevated especially in areas with increased vessel proliferation such as the invasive fronts of gliomas (Oh et al., 2019; Yamada et al., 1995). Initially, this EMT signature was mainly ascribed to the glioma cells. However, Mäder et al. were able to show that the transcription factors SLUG and TWIST are almost exclusively expressed by pericytes/VAMCs of glioma blood vessel proliferations, while being absent in glioma cells, ECs and also in “normal” pericytes. The notion of pericytes as the source of EMT transcription factors is further supported by the fact that other vascular tumors such as angiosarcomas or hemangioblastomas also display more SLUG and TWIST positive cells in similar

cellular association as seen in GBMs, while non-vascular tumors are devoid of the same (Mäder et al., 2018). The high expression levels of EMT transcription factors in glioma-associated pericytes (GA-Peris) suggest, that these non-neoplastic cells undergo an EMT-related activation during glioma-associated neoangiogenic processes leading to enhanced proliferation, motility and altered growth patterns (Wirsik et al., 2021). This indicates that not the GBM cells themselves, but rather the activation of EMT-processes in pericytes results in morphological changes in GBM-associated vessels. Figure 2 schematically presents this model of EMT-like activation of pericytes in GBM.

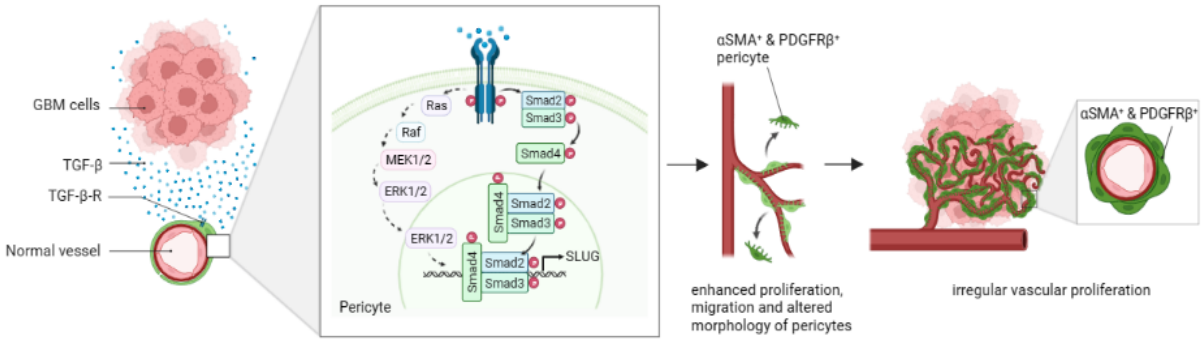

Figure 2: Model of EMT-like activation of VAMCs in GBM*. TGF-β1 and -β2 released by GBM cells induce an EMT-like activation process of pericytes via upregulation of EMT factors like SLUG, leading to enhanced proliferation, migration and morphological alterations of pericytes. These activated PDGFRβ⁺ and αSMA⁺ pericytes then contribute to GBMs´ excessive and irregular vascularization. Created with BioRender.com.*

1.6 Objective of this project

GBM vessel structure is altered and the significant structural abnormalities result in dysregulated blood flow and ischemia as well as impaired transport of drugs limiting therapeutic efficiency (Jain et al., 2007). “In recent years, increased attention has been paid to vessel-covering pericytes and their interaction with endothelial cells during vessel formation processes in tumors, including GBM.” (cited from Merk et al., 2024) It is essential to understand how GBM cells modulate pericytes and which mechanisms are involved in functional changes of pericytes resulting in their dysfunction, abnormal vascularization and breakdown of the BBB.

TGF-β secreted by glioma cells is suggested to stimulate the development of a mesenchymal phenotype in pericytes characterized by enhanced αSMA and PDGFRβ levels, that results in pericyte proliferation, migration and morphological changes (Wirsik et al., 2021). The elevated SLUG expression in pericytes of human GBM samples with simultaneous enhanced αSMA and PDGFRβ levels indicate that the induction of an EMT-like program is associated with SLUG upregulation (Mäder et al., 2018; Wirsik et al., 2021). These assumptions were supported by the fact that the knockdown of SLUG in human brain microvascular pericytes (HBVP) *in vitro* completely inhibited the capability of TGF-β to trigger proliferation, migration and metabolic activity in GA-Peris (Wirsik et al., 2021). Therefore, TGF-β induces, at least *in vitro*, a mesenchymal phenotype in pericytes via SLUG-mediated signaling. Whether these TGF-β and SLUG mediated effects detected *in vitro* can be transferred to the *in vivo* situation is the main investigative purpose of my thesis.

“We initially examined whether the absence of TGF-β in GBM cells prevents VAMC stimulation *in vivo*. Therefore, the amount of activated VAMCs was identified by antibody-dependent immunofluorescent (IF) staining for PDGFRβ and αSMA in relation to the EMT transcription factor SLUG after TGF-β knockout (KO) in GBM cells. Furthermore, we investigated whether the knockout of SLUG specifically in VAMCs inhibits the capability of TGF-β to induce a mesenchymal phenotype in these cells” (cited from Merk et al., 2024 in a modified way). To achieve a VAMC-specific SLUG-KO in mice brains, a lentivirus-based approach using a CRISPR/Cas9 technology with DNA oligos encoding guide RNAs (gRNA) targeting SLUG was

deployed. VAMC activation was again determined by IF staining for PDGFRβ and αSMA.

As it has been shown that structural and functional vessel abnormalities within GBM correlate with an irregular pericyte coverage (Cheng et al., 2013), we were interested if the inhibition of the TGF-β-mediated EMT-like activation in glioma-associated VAMCs influences the architecture of newly-formed tumor-associated vessels. We investigated whether knocking out TGF-β in GBM cells or the knockout of SLUG specifically in VAMCs not only prevents VAMC activation but also leads to lesser vascular malformations (Figure 3). Therefore, vessel structure was analyzed by IF staining for ECs. Additionally, three-dimensional depiction of tumor-associated vessels was performed.

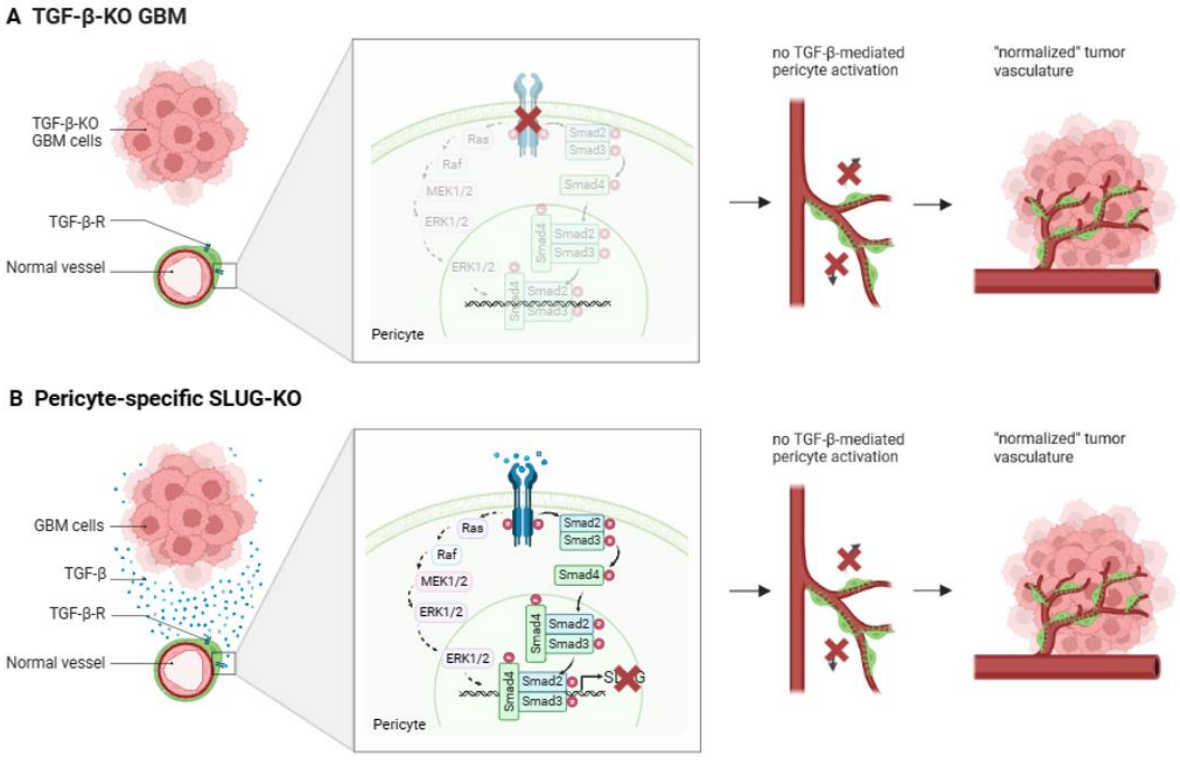

Figure 3: Postulated effects of the absence of TGF-β-signaling on the development of an activated phenotype in glioma-associated VAMCs. *TGF-β-KO GBMs (A) are due to the absence of TGF-β not expected to induce EMT-like activation in VAMCs (represented by "pericytes" in this graphic) of tumor vessels via TGF-β-mediated induction of SLUG. The missing stimulation of VAMCs may in turn result in less vascular alterations. After VAMC-specific SLUG-KO (B) we postulate similar effects, as the TGF-β-mediated upregulation of SLUG process is inhibited. This should also hinder the EMT-like activation of glioma-associated VAMCs which may then result in a "more normal" intra-tumoral vessel structure. Created with BioRender.com*

These examinations concerning the importance of EMT factor-expressing VAMCs for tumor-angiogenesis, vessel structure and therefore putatively also BBB integrity are required not only to attain a better understanding of vascular biology, but also to realize the full potential of antiangiogenic therapy.

2 Material and Methods

2.1 Material

2.1.1 Chemicals, Media, and Reagents

Table 1: Chemicals

Description	Supplier
2-Propanol	Merck KGaA, Darmstadt, Germany
Acetone	BioFroxx, Einhausen, Germany
Bovine Serum Albumine	Sigma Aldrich, St. Louis, USA
DAKO Fluorescence Mounting Media	Agilent Technologies, Santa Clara, USA
Dimethylsulfoxid (DMSO)	Carl Roth GmbH + Co. KG, Karlsruhe, Germany
Ethanol	Merck, Darmstadt, Germany
Formaldehyd	Merck, Darmstadt, Germany
Hydrogen Peroxide Solution	Sigma Aldrich, St. Louis, USA
Immersion Oil	ZEISS, Oberkochen, Germany
Nuclease-Free Water	Promega, Madison, USA
Poly-L-Lysin	Sigma Aldrich, St. Louis, USA
Puromycin	AppliChem, Darmstadt, Germany
Sucrose	Sigma Aldrich, St. Louis, USA
Tissue-Tek® O.C.T.^{Tm} Compound	SAKURA Finetek, Alphen aan den Rijn, NL
TransIT-LT1 Transfection Reagent	Mirus Bio LCC, Madison, USA
Triton X-100	Sigma Aldrich, St. Louis, USA
Trypsin	Sigma Aldrich, St. Louis, USA
Tween®-20	Carl Roth GmbH + Co. KG, Karlsruhe, Germany
VECTASHIELD® Antifade Mounting Media with DAPI	BIOZOL Diagnostica Vertrieb GmbH

Table 2: Media

Description	Supplier
Dulbecco's modified Eagle Medium (DMEM), high glucose	Sigma Aldrich, St. Louis, USA
Iscove´s Modified Dulbecco´s Medium (IMDM)	Gibco, ThermoFisher SCIENTIFIC / Sigma Aldrich, St. Louis, USA
LB-Medium (Lennox)	Carl Roth GmbH + Co. KG, Karlsruhe, Germany
Opti-MEM I (1X) + GlutaMAX-I	Gibco, ThermoFisher SCIENTIFIC, St. Louis, USA
Endothelial Basal Medium-2 (EBM-2)	Lonza, Wakersville, USA
SOC outgrowth medium	NEB, Frankfurt, Germany
LB agar plates supplemented with ampicillin (100 µg/mL)	Carl Roth GmbH + Co. KG, Karlsruhe, Germany

Table 3: Reagents

Description	Supplier
1x TBST	for 2 L: 100 ml 20x TBS +190 ml VE water +1 ml Tween® 20
20x TBS	for 2 L: 96.8 g Tris-Base +320 g Sodium chloride in 1600ml ddH2O, adjusted pH with 10M HCl to 7.6 and added up to 2000ml with ddH2O
Bepanthen® Eye and Nose Ointment	Bayer Vital GmbH, Leverkusen, Germany
Betaisadonna Solution, Povidon-Ion, Antiseptica	mundipharma, Frankfurt, Germany
Dulbecco´s Phosphate Buffered Saline, modified	Sigma Aldrich, St. Louis, USA
Fetal Calf Serum (FCS)	Gibco, ThermoFisher SCIENTIFIC / Sigma Aldrich, St. Louis, USA
Penicillin / Streptomycin	Sigma Aldrich, St. Louis, USA
PTwH	for 1l: 100ml PBS 10X + 2ml Tween-20 + 1ml Heparin (10mg/ml)
PTx.2	for 1l: 100ml PBS 10x + 2ml Triton-X100, pH 7.4

2.1.2 Cell Lines

Table 4: Cell Lines

Description	Type	Supplier
GL261 mCherry	chemical induced, mouse-derived glioma cell line	German Collection of Microorganisms and Cell Cultures GmbH
GL261 mCherry TGF β 1/2 KO	chemical induced, mouse-derived glioma cell line	German Collection of Microorganisms and Cell Cultures GmbH, genetically modified in our Laboratory by Hermann Eckhardt
HEK-293FT	human embryonic kidney	Microbix, Mississauga, ON, Canada
LNT-229	human glioblastoma cell line	N. Tribolet, Geneva, Switzerland
Pericytes	GFP positive mouse pericytes	own preparation

2.1.3 Viruses and Bacteria

Table 5: Viruses

Description	date of preparation	Virus Titer (IP/µl)	Supplier
pLentiCRISPRv2	22.06.2022	2,54E+03	own production
pLentiCRISPRv2-mSLUG1-mRGS5Pro14	22.06.2022	2,65E+03	own production
pLentiCRISPRv2-mSLUG4-mRGS5Pro14	22.06.2022	6,06E+03	own production
pLentiCRISPRv2-mSLUG5-mRGS5Pro14	22.06.2022	1,50E+05	own production
pLV mCherry	22.06.2022	1,07E+04	own production

Table 6: Bacteria

Description	Supplier
NEB® 5 alpha Competent Escherichia coli (E. coli)	NEB, Frankfurt, Germany

2.1.4 Antibodies

Table 7: Primary Antibodies

Description	Catalog	Supplier
Alpha-Smooth Muscle Actin Recombinant Polyclonal Antibody (17HCLC)	# 710487	ThermoFisher SCIENTIFIC Invitrogen, Waltham, USA
Anti-CD31 Antibody	# ab28364	abcam, Cambridge, UK
CD140b (PDGFRB) Monoclonal Antibody (APB5), eBioscience™	# 14-1402-82	ThermoFisher SCIENTIFIC Invitrogen, Waltham, USA
CD31 (PECAM-1) Monoclonal Antibody (390), eBioscience™	# 14-0311-82	ThermoFisher SCIENTIFIC Invitrogen, Waltham, USA
Chicken anti-mCherry Antibody	# NBP2-25158	NOVUS BIOLOGICALS, Centennial, USA
DRAQ5™ Fluorescent Probe Solution	# 62252	ThermoFisher SCIENTIFIC , Waltham, USA
GFP Polyclonal Antibody	# A10262	ThermoFisher SCIENTIFIC Invitrogen, Waltham, USA
Rabbit IgG Isotype Control	# 31235	ThermoFisher SCIENTIFIC Invitrogen, Waltham, USA
Rat IgG Isotype Control	# 31933	ThermoFisher SCIENTIFIC Invitrogen, Waltham, USA
Slug (C19G7) Rabbit mAb	# 9585	Cell Signaling TECHNOLOGY, Danvers, USA

Table 8: Secondary Antibodies

Description	Catalog	Supplier
Goat anti-Chicken IgY (H+L) Secondary Antibody, Alexa Fluor™ 488	# A-11039	ThermoFisher SCIENTIFIC Invitrogen, Waltham, USA
Goat anti-Chicken IgY (H+L) Secondary Antibody, Alexa Fluor™ 546	# A-11040	ThermoFisher SCIENTIFIC Invitrogen, Waltham, USA
Goat anti-Rabbit IgG (H+L) Cross-Adsorbed Secondary Antibody, Alexa Fluor™ 405	# A-31556	ThermoFisher SCIENTIFIC Invitrogen, Waltham, USA
Goat anti-Rabbit IgG (H+L) Highly Cross-Adsorbed Secondary Antibody, Alexa Fluor™ 647	# A-21245	ThermoFisher SCIENTIFIC Invitrogen, Waltham, USA
Goat anti-Rat IgG (H+L) Cross-Adsorbed Secondary Antibody, Alexa Fluor™ 647	# A-21247	ThermoFisher SCIENTIFIC Invitrogen, Waltham, USA
Goat anti-Chicken IgG (H+L) Secondary Antibody, Alexa Fluor™ 546	# A-11040	ThermoFisher SCIENTIFIC Invitrogen, Waltham, USA
Goat anti-Rabbit IgG (H+L) Highly Cross-Adsorbed Secondary Antibody, Alexa Fluor™ 488	# A-11034	ThermoFisher SCIENTIFIC Invitrogen, Waltham, USA

2.1.5 Kits

Table 9: Kits

Description	Supplier
Plasmid DNA Purification (NucleoBond Xtra Midi/Maxi) KIT	MACHEREY-NAGEL GmbH & Co. KG, Düren, Germany
QuickTiterTM Lentivirus Titer Kit (Lentivirus Associated HIV p24)	Cell Biolabs Inc., San Diego, USA

2.1.6 Narcotics

Table 10: Narcotics

Description	Concentration	Supplier
Isoflurane		cp-pharma, Burgdorf, Germany
Surgical Anesthesia		
Fentanyl	0,05 mg/kg BW	Dechra, Aulendorf, Germany
Midazolam	5,00 mg/kg BW	provided by veterinarians of the Animal Welfare and Veterinary Office at the University of Tübingen
Medetomidine	0,50 mg/kg BW	provided by veterinarians of the Animal Welfare and Veterinary Office at the University of Tübingen
Analgesia		
Carprofen	5,00 mg/kg BW	provided by veterinarians of the Animal Welfare and Veterinary Office at the University of Tübingen
Antidote		
Atipamezole	2,50 mg/kg BW	provided by veterinarians of the Animal Welfare and Veterinary Office at the University of Tübingen
Flumazenil	0,50 mg/kg BW	provided by veterinarians of the Animal Welfare and Veterinary Office at the University of Tübingen
Naloxone	1,20 mg/kg BW	provided by veterinarians of the Animal Welfare and Veterinary Office at the University of Tübingen

2.1.7 Devices

Table 11: Devices

Description	Supplier
Axio Imager with ApoTome2	ZEISS, Oberkochen, Germany
Axiovert 200M Microscope	ZEISS, Oberkochen, Germany
Bacteria Incubator Shaker	HT INFORS, Einsbach, Germany
Centrifuge 5417R	Eppendorf, Mississauga, USA
Centrifuge, Megafuge 1.0	Heraeus Holding GmbH, Hanau, Germany
Centrifuge, MULTIFUGE 3 S-R	Heraeus Holding GmbH, Hanau, Germany
CO2 Incubator	SANYO, München, Deutschland
Drill MH145 FM3545	Foredom electric co., Bethel, USA
Heating Mat Standard	Terra EXOTICA, Alfeld, Germany
Leica CM3050 Cryotome	Leica, Deer Park, USA
Leica SP8 Microscope	Leica, Deer Park, USA
LSM 510 META	ZEISS, Oberkochen, Germany
LSM 710	ZEISS, Oberkochen, Germany
pH-meter	Schott, Mainz, Germany
Precision Balance	KERN und SOHN, Balingen-Frommern, Germany
Rocking Shaker ROCKY®	Fröbel, Blaufelden, Germany
Spectrophotometer ND-1000	Peqlab Biotechnologie GmbH, Erlangen, Germany
SteREO Lamp CL 1500 ECO	ZEISS, Oberkochen, Germany
Stereotactic device, mouse	ConductScience, Skokie, USA
Sterile Workbench HERAsafe	Heraeus Holding GmbH, Hanau, Germany
T1-SM Nikon Microscope	Nikon, Amstelveen, NL
Thermomixer comfort	Eppendorf, Mississauga, USA
TriStar2 LB942 Multimode Reader	Berthold Technologies, Bad Wildbad, Germany
Vortex-genie 2	Scientific Industries, New York, USA

2.1.8 Software

Table 12: Software

Description	Supplier
Excel	Microsoft, Redmont, Washington, USA
GraphPad Prism 5	GraphPad, La Jolla, USA
Image J	Wayne Rasband, Bethesda, USA
Imaris	Oxford Instruments, Abington, UK
SPSS	IBM, New York, USA
Word	Microsoft, Redmont, Washington, USA
ZEN black	ZEISS, Oberkochen, Germany
ZEN blue	ZEISS, Oberkochen, Germany

2.2 Methods

2.2.1 Cell culture

2.2.1.1 Maintenance

All cells were kept at 37 °C with 5 % CO_2. GL261^{mCherry}, GL261 TGF1/2 Double-KO ^{mCherry}, LNT-229 and HEK-293FT cells were all maintained in Dulbecco's Modified Eagle's Medium (DMEM) supplemented with 10 % fetal calf serum (FCS) and 1 % penicillin-streptomycin (P/S).

2.2.1.2 Cell splitting

Cells were passaged once they reached approximately 80 % confluency. For this purpose, the medium was discarded and cells were washed with 1x phosphate buffered saline (PBS) before 1 ml of trypsin was added for 2-3 min at room temperature. Subsequently, the detached cells were resuspended in their corresponding media, transferred into 15 ml falcon tubes, centrifuged (900 rpm, 5 min) and resuspended in fresh medium. An aliquot was transferred back into the flask. GL261 and HEK-293FT cells were split in a 1:10 ratio, LNT-229 cells in a 1:20 ratio.

2.2.1.3 Cell freezing

For cell freezing, the detached cells were resuspended in fresh DMEM comprising 10 % DMSO. The cells were then aliquoted into cryogenic vials, placed in a cryofreezing container and transferred to -80 °C. For short-term storage, cells were stored at -80 °C. For long-term storage, the cell-containing tubes were transferred to -148 °C.

2.2.1.4 Cell counting

To determine the number of cells, a Neubauer cell counting chamber was used.
10 µl of the resuspended cells were carefully pipetted between the coverslip and the chamber. Cells with intact cell membrane were count using the T1-SM Nikon Microscope.

2.2.2 Lentiviral transduction

Lentiviral shuttle vectors utilizing a CRISPR/Cas9 system targeting SLUG were designed and analyzed for in vitro editing efficiency by Marietheres Evers as part of her Master thesis. The lentiviruses express CAS9 under the control of the mural cell specific promoter RGS5 as well as sgRNAs specific for murine SLUG (Lenti-RGS5-CRISPR-SLUG 1, 4 and 5). The mixture of those three lentiviruses has been proven to show the highest *in vitro* target efficacy and was therefore produced for the *in vivo* experiments (Merk et al., 2024).

2.2.2.1 Transformation and Production of frozen glycerol E. coli stocks

50 µl NEB® 5alpha Competent Escherichia coli (E. coli) were thawed on ice. Then, appropriate amounts of vectors were added to the E. coli cells. The cells were kept on ice for 30 min, followed by heat-shocking at 42 °C for exactly 45 sec before they were put back on ice. After five minutes, 1 ml Super Optimal broth with Catabolite repression (SOC) outgrowth medium was added to the cells. Next, the cells were incubated for 1 h at 37 °C with shaking (450 rpm). Afterwards, 250 µl were plated on prewarmed LB agar plates supplemented with ampicillin (100 µg/ml). The residue was then pelleted by centrifugation (2500 rpm, 2 min), resuspended in 200 µl of the supernatant and plated on a second LB agar plate. The transformed bacteria were incubated overnight at 37 °C.

For the production of frozen glycerol E. coli stocks, one E. coli colony was transferred into 1 ml LB-Media containing 100 µl ampicillin and was incubated overnight. 500 µl of Glycerol were added to 1 ml of incubated E. coli cells before they were frozen at -80 °C.

2.2.2.2 Plasmid isolation via Midi prep

Verified plasmid DNA was isolated from 100 ml bacterial overnight cultures using the Xtra Midi Kit (Macherey-Nagel). Therefore, a deduction of frozen glycerol E. coli stocks of the corresponding plasmids was taken into culture in 100 ml LB-Medium containing 100 µl ampicillin and was incubated overnight at 37 °C on a shaker. The next day, plasmid DNA purification was performed following the manufacturers protocol. Plasmid DNA concentration (ng/µl) and purity were determined by

absorbance measurement at 260 nm and 280 nm. DNase-free water was used for calibration.

2.2.2.3 Lentivirus production

10 cm dishes were coated with 2 µg/cm² Poly-L-Lysin in PBS per dish for two hours at 37 °C in order to guarantee optimal cell attachment, before continuing with the lentivirus production.

Three million HEK-293FT cells were seeded in each of the Poly-L-Lysin coated dishes in DMEM containing 10 % FCS and 1 % P/S. They were left to attach overnight at 37 °C in the incubator until they had reached an optimal confluency for transfection around 80-90 %.

Then, the medium was changed to 8 ml Opti-MEM I reduced-serum medium per dish before performing the transfection with 2.2 µg of PLP-1 (packaging construct 1), 1.1 µg PLP-2 (packaging construct 2), 1.3 µg VSV-G (packaging construct 3) and 3 µg of the respective lentiviral shuttle vector (either pLentiCRISPRv2-mSLUG1-mRGS5Pro14, pLentiCRISPRv2-mSLUG4-mRGS5Pro14, pLentiCRISPRv2-mSLUG5-mRGS5Pro14, pLentiCRISPRv2, pLVmCherry). Therefore, the DNA-mix was diluted in double distilled water (ddH_2O) to a volume of 50 µl and added to 30 µl of MIRUS-TransiTlenti Reagent previously mixed with 20 µl of ddH_2O. The mixture was left at room temperature for 20 min to incubate. Afterwards, this mixture was taken up in 1,5 ml of Opti-MEM and added dropwise to the HEK-293FT cells. After 24 hours incubation at 37 °C, the media was changed to 8 ml DMEM containing 0,5 % FCS and 1 % P/S. The next day, the supernatant (SN) was collected and new 8 ml of DMEM were added. The collected SN was stored in the fridge at 4 °C. Further 24 h later, a second supernatant collection was performed. Afterwards, the SN was centrifuged at 2000 x g for 5 min to precipitate the cells and debris and then filtered through a 0.45 µm sterile filter. To concentrate the virus, polyethylene glycol (PEG)-precipitation was used (Fricano-Kugler et al., 2016). Therefore 3,2 ml PEG 6000 were added to the filtered SN, gently mixed and stored overnight at 4°C with occasionally remixing. After 24 hours, the mixture was centrifuged at 2500 x g for 45 min at 4 °C, then the supernatant was removed and discarded. It was centrifuged a

second time for 2 min at 2500 x g to remove and discard the remaining supernatant. Then the pellet was resuspended in 120 µl cold PBS and stored in the fridge overnight. Subsequently, 10 µl aliquots were stored at -80 °C until required.

2.2.3 Virus titer determination via ELISA-Kit

The QuickTiter™ Lentivirus Titer Kit (detection of the HIV protein p24) from Cell Biolabs was used to determine the concentration of the produced lentiviruses. The essay was performed following the manufacturers' protocol. Each lentiviral sample as well as the control standards were assayed in duplicate. Absorbance of each microwell was measured using the Berthold TriStar2 LB942 Multimode Reader.

For the calculation of Lentivirus Titer (VP/ml), the p24 amount was determined using the following formula:

$$p24\ Titer\ \left(Virus\ associated\ p24\frac{ng}{ml}\right) = p24\ (ng/ml)\ x\ Dilution\ Factor\ x\ 0.25\ ml/1.0\ ml$$

With the known amount of p24 molecules, the lentivirus titer was calculated. One lentiviral particle (LP) contains approximately 2000 molecules of p24 which is equivalent to $8x10^{-5}$ pg of p24 per LP.

p24 Titer in ng/ml were calculated, implying how many virus particles are present/ml:

$$\frac{Virus\ particles}{ml} = p24\ Titer\ \frac{ng}{ml} \times (1.25\ \times 10^7)$$

The calculated virus particles were equivalent to the lentivirus physical titer according to the p24 core protein level and not the infectious titer, which had to be determined:

$$Infectious\ Virus = \frac{Virus\ particles}{10^2}$$

2.2.4 Pericyte isolation from mouse brains

Pericyte isolation from 3 RGS5/GFP$^+$ pericyte reporter mice was performed under a sterile bench. The mice were sacrificed and their brains were harvested. By rolling the brains on sterile Whatman paper, the meninges were removed and the meninges-free brains were transferred to a 15 ml Falcon tube containing 10 ml Minimal Essential Medium (MEM)+ P/S. The brains were centrifuged at 300 x g for 5 min. Then, the supernatant was removed and the tissue was resuspended in 4 ml of enzymatic solution (Papain Dissociation System; Worthington, Freehold, NJ, USA). The enzymatic solution was previously prepared by adding 500 µl Earle's balanced salt solution (EBSS) into 1 vial DNase, from which then 250 µl were used to reconstitute 1 vial papain before 3,75 ml EBSS were added to the papain solution to a total of 4 ml. After incubation at 37°C for 70 min with inverting every 10 min, the tissue was homogenized by passing it 10 times through a sterile glass pipette using a grey knob. Afterwards it was centrifuged again for 5 min at 300 x g followed by removal of SN. 10 ml of sterile 33 % BSA solution were added to the homogenized tissue and briefly mixed before centrifuging again for 10 min at 1000 x g in order to separate myelin. The lipid layer on top was carefully removed. The cell pellet was now resuspended in 5 ml endothelial basal medium-2 EBM2$^+$ and was again centrifuged at 300 x g for 5 min, before the SN was removed and plated on one previously collagen-coated dish (5 ug/cm^2). The cell pellet was resuspended in 4 ml EBM2$^+$ before the mixture was plated on the collagen-coated dishes. After 20 h, new EBM2$^+$ was added. Medium change was performed every second day from now on. Cells were checked for GFP fluorescence on day 3 and 7 using the Axiovert 200M Microscope.

2.2.5 Animal experiments

Animal handling, experiments and included procedures were approved by the Institute of Animal Welfare and the Veterinary Office at the University of Tübingen and the regional council Tübingen. Animal experiments were registered under the animal license number N05/17.

RGS5-GPF^{+} pericyte reporter mice (C57BL/6$^{rgs5GFP/GFP}$) of both sexes were used for all experiments. Their ages ranged from 3 to 9 month. Mice were bred in the animal facility of the Hertie Institute for Clinical Brain Research and were housed in individually ventilated cages (IVC). They were kept in 12-12 hours light-dark cycle with ad libitum feeding. Originally, this mouse strain was kindly provided by Dr. Genove [Karolinska Institute, Stockholm, Sweden (Nisancioglu et al., 2008)].

2.2.5.1 Intrastriatal glioma cell injection

Throughout the surgery, a sterile microenvironment is maintained, including all surgical instruments and supplies.

Animals were anesthetized by intraperitoneal injection of narcotics depending on their individual weight (0,1 ml/10g body weight). Pain management during anesthesia was supplemented with subcutaneous injection of 0,1 ml Carprofen. The mice were intensively monitored throughout the surgery to avoid and reduce pain. A toe pinch for testing the intertidal reflex was used to confirm the mouses unconsciousness in order to ensure an adequate anesthesia. Breathing was monitored throughout the whole surgery. Eye protection was performed using Bepanthen® eye and nose ointment. The surgical incision site in the middle of the mouse's head was shaved, the hair was removed and the skin was disinfected with betaisadonna solution (Povidone-Ion). Next, a sagittal skin incision was made using a disposable scalpel blade. Afterwards, the animal was placed on the stereotact, fixed by hinging the top front teeth into the indentation of the stereotact. Additionally, the head was fixed from two metal pens positioned in both ears to hinder side movements. Subsequent, the skull surface was exposed and 3 % H_2O_2 was used to remove the periost and display the bregma, the intersection of the sutura coronalis and sagittalis, nicely. A burrhole was made 1 mm rostal and 2 mm lateral of the bregma, using the mouse brain atlas coordinates; The Mouse Brain Atlas (gaidi.ca). The Hamilton syringe needle was moved to the burrhole and from there 3 mm deep into the brain and 0,5 mm back out. Then the stereotactic injection of 100.000 tumor cells in 2 µl PBS was performed using a micro injector. The cell suspension was infused over 2 minutes. Afterwards the needle was left in place for 1 min to prevent leakage from the injection site before it was withdrawn carefully. The burrhole was

closed using histoacryl tissue glue. Then the incision site was sutured with 2 to 3 single button stitches. Anesthesia was ended through application of antidot (0,1 ml/10 g body weight). The mice were placed in a cage under a heating lamp and were intensively monitored post-operatively until they were completely awake and retained normal activity before they were returned to group housing.

2.2.5.2 Intrastriatal Lentivirus injection

For those animal experiments requiring the lentivirus-mediated, VAMC-specific knockout of SLUG, the surgery procedure was similar to the one previously described for the intrastriatal syngeneic glioma cell implantation.

Instead of tumor cells, the mice were injected with either $3x10^5$ infectious particles of Lenti-CRISPR v2 not targeting SLUG (control virus) or a mixture of the three lentiviruses (Lenti-RGS5-CRISPR-SLUG 1, 4 and 5) (described in Merk et al., 2024). The lentivirus injection was performed 3 days prior to $GL261^{mCherry}$ tumor implantation using the same brain coordinates as described above. Either the virus mix or the control virus were injected with an infusion speed of 1 µl/min.

2.2.5.3 Animal Maintenance

The mice were monitored regularly during all experiments. Inconspicuous animals were checked every second day, which included weighing and scoring of neurological abilities and general appearance as well as behavior and posture. If mice started to show abnormalities, they were checked daily in order to prevent unnecessary suffering.

2.2.5.4 Killing

Animals were euthanized by CO_2 inhalation and cervical dislocation either after a defined amount of time or when the first mouse of the group started to show tumor associated symptoms of declining health including weight loss (maximum 20 %), reduced mobility and explorative behavior, hunched posture, or neurological symptoms such as ataxia, paralysis and loss-of-balance.

2.2.5.5 Brain Harvesting

After the mice were euthanized, their heads were separated, skin and skull were removed using a sharp scissor and the brain was carefully luxated from lateral. Only both hemispheres were collected, the cerebellum and brain stem were discarded.

2.2.6 Immunohistochemistry

2.2.6.1 Sample Fixation

For 4 % PFA immersion fixation, the collected brains were placed in 8 ml 4 % PFA for 20 hours immediately after harvesting, followed by cryoprotection through a sucrose gradient. Therefore, the brains were incubated in 20 % sucrose solution for two days until they sank down. They were then transferred to 30 % sucrose solution for another two days before removing the sucrose solution and freezing them at -80 °C with subsequent embedding in Tissue Tek® and cryosectioning.

Snap freezing of mouse brains was performed by freezing them on dry ice immediately after their collection. Afterwards, the brains were stored at -80 °C with subsequent embedding in Tissue Tek® and cryosectioning.

Post-fixation of snap frozen brain slices was carried out by either incubating them with 4 % PFA at 37 °C for 5 or 10 min or with acetone on ice for 10 min before they were washed thrice for 10 min in PBS.

To compare the preservation of fluorescent proteins, all sections were analyzed using the Zeiss Axiovert 200M Microscope at 10x magnification.

2.2.6.2 Cryosectioning

The frozen brains were cut in 2 to 3 mm coronal sections, which were then embedded in Tissue-Tek® O.C.T™ Compound (Sakura) prior to cryosectioning. Cryosectioning was conducted using a LEICA CM3050 Cryotome. The in Tissue-Tek® embedded samples were cut in 10 µm slices and transferred to SuperFrost™ Plus slides (R. Langenbrinck GmbH). The cut slides were stored at -20 °C until immunostaining was performed.

2.2.6.3 Immunofluorescence staining

The establishment of the used staining protocols was done in collaboration with Katja Regel, Master student under my supervision.

The appropriate slides were removed from the -20 °C freezer and were left at room temperature for 5 min. Then, they were washed in PBS containing 0,2 % Triton® X-100 for 10 min to permeabilize cell membranes. To avoid unspecific binding of secondary antibody, the sections were incubated for 1 h at room temperature (RT) in blocking solution consisting of 5% bovine serum albumin (BSA) and 0.5 % Triton® X-100 in PBS. Excess blocking solution was removed by washing the slides in PBS for 10 min. Subsequently, the respective primary antibody combination diluted in PBS (αSMA, 1:100; CD140b (PDGFRB), 1:100; CD31, 1:100; GFP, 1:100; all from Invitrogen, Carlsbad, CA, USA) was put on the sections. The sections were then incubated at 4 °C for 24 h before they were washed three times for 10 min in PBS in order to remove unbound primary antibodies. The slices were subsequently incubated with the appropriate secondary antibodies diluted in PBS (Goat anti-Chicken Alexa Fluor™ 488, Invitrogen, 1:1000; Goat anti-Rabbit Alexa Fluor™ 405, 1:1000; Goat anti-Rabbit Alexa Fluor™ 647, 1:1000; Goat anti-Rat Alexa Fluor™ 647, 1:1000; all from Invitrogen) for 1,5 h at room temperature. Afterwards, the sections were washed again twice for 10 min and once for 15 min before they were mounted either with DAKO mounting medium or alternatively with Vectashield® antifade mounting media containing DAPI in case no AF405 secondary antibody was used for staining. They were left overnight at 4 °C to allow the coverslips to dry. The stained slices were kept at 4°C until microscopy was finished (as also described in detail in Merk et al., 2024).

2.2.6.4 Fluorescence microscopy and analysis

All stained tissue samples were assessed for the proteins of interest using the Zeiss Axio Imager with ApoTome2. Images were captured in different magnifications (10x, 25x, 40x and 63x) with fixed exposure settings.

Image processing was conducted using the ZEN blue 3.6 software (Carl Zeiss) and afterwards, all pictures were saved in TIFF-format. Subsequent analysis was performed using Image J.
For the analysis of marker expression, taken pictures were split into their different channels and were background corrected. The generated single channel images were further converted to binary data pictures. Percent-Area (%Area) analysis was performed by default mask overlay with stabile threshold limits to detect the relative amount of fluorescence. The raw results were then statistically analyzed using SPSS.

2.2.7 CLARITY

Recent advancements in the field of tissue clearing have increased the ability to track proteins in three-dimensional samples. CLARITY (Clear Lipid-exchanged Acrylamide-hybridized Rigid Imaging/ Immunostaining/ in situ-hybridization-compatible Tissue hYdrogel) (Chung & Deisseroth, 2013; Liu et al., 2016) is a technique that preserves anatomical structure, proteins and nucleic acids in whole tissue samples by using cross-linking of hydrogel monomers and formaldehyde to functional groups on proteins and nucleic acids (Chung et al., 2013; Yushchenko & Schultz, 2013). Meanwhile, the light-scattering lipids get removed by detergent, which results in optically transparent and macromolecule-permeable 3-D-tissue samples that can be immunostained as a whole (Liu et al., 2016). Afterwards, confocal z-stacks can be used for recreation of a 3-dimensional image (Chandrasekharan & Neish, 2021).

CLARITY of mouse brains was performed in cooperation with Dr. Andreas Mack and Ulrich Mattheus from the Anatomical Institute in Tübingen using the passive tissue clearing method PACT (Jensen & Berg, 2017; Tomer et al., 2014).
After sacrificing the mice, the brains were collected as previously described. They were instantly transferred to at least 25 ml of cold Hydrogen Monomers (HM) solution per brain consisting of 40 ml 40% Acrylamide, 10 ml 2% bisacrylamide, 40 ml 10X PBS, 100 ml 16% PFA, 210 ml distillated water and 1 g VA-044 polymerization

initiator as described in the original CLARITY protocol (Chung et al., 2013). The HM-solution was freshly mixed on ice with special attention to safety precautions before use and always kept cool to prevent premature polymerization. The collected brains were stored in the HM-solution at 4°C at least overnight but not longer than 2 days for fixation until the polymerization was started. Therefore, the HM-solution was removed partially, so that there were only 5 ml HM-solution left completely covering the brain. The polymerization was performed using an exsiccator with vacuum to remove the residual oxygen from the tissue, as oxygen interferes with the polymerization resulting in incomplete hydrogel formation (Du et al., 2018). The tissue was incubated at 42°C for 2 to 3 hours to complete the polymerization process. Afterwards, surplus HM-Gel of the in hydrogel embedded brain samples was carefully removed by cutting off excess gel before the brains´ surfaces were cleaned from remaining gel through gently rolling over a Kim wipe.

Then, the brains were cut in 2-3 mm coronal slices, as previous papers showed that the clearance and staining process is improved when using smaller samples (Chung & Deisseroth, 2013; Poguzhelskaya et al., 2014).

For the lipid removal, the brain slides were put in 45 ml of 8 % SDS in PBS and incubated at 50 °C with continuous moving in a rotator with changing of SDS once a week until the tissue had reached a homogenic transparency. Tissue transparency was assessed by visualization of high-contrast signals through the tissue and was reached after approximately 4 weeks.

The transparent brains were washed thrice for 2 hours in PBST before they were put in PBS overnight. The next day, the brains were washed again with PBST for 2 hours before they were incubated for 2 days at 37 °C in pre-incubation solution consisting of 4 % goat-serum, 1 % BSA, 0,25 % Triton and 0,01 % sodium azide in PBS. Subsequently, the brains were incubated for 5 days with the following primary antibodies diluted in pre-incubation solution at 37 °C: anti-CD31 (1:25-1:50, Abcam, Cambridge, UK) and anti-mCherry (1:500, NOVUS Biologicals, Centennial, USA). Excess antibodies were washed off thrice for 2 hours in PBST. The samples were then put in PBST for 2 days at 37 °C followed by incubation with secondary antibodies (goat-anti-rabbit Alexa 488, 1:200; goat-anti-chicken Alexa 546, 1:200; all from Invitrogen, Carlsbad, CA, USA) and DRAQ5 for nuclear staining (1:500,

Thermo Fisher Scientific, Waltham, MA, USA). Afterwards, the samples were washed three times in PBST for 2 hours each followed by washing with either PBS containing 0,01% sodium azide or PBST overnight. The next day, the samples were washed for 2 hours in PBS before they were put first for 2 hours and then for another 4 hours in 80 % glycerol at 37 °C to homogenize the microscopic environment within the tissue, as 80 % glycerol matches closely to the refractive index of the hydrogel (Du et al., 2018). The brains were stored in 80 % glycerol at 4 °C overnight before confocal microscopy using a Zeiss LSM 510 was performed.

The taken images were processed using the ZEN black software (Carl Zeiss) and Image J. Subsequent analysis was performed using Imaris software (Oxford instruments).

This method is detailly described in my publication and here cited in a modified form from my publication (Merk et al., 2024).

2.2.8 Statistical analyses

Further statistical analyses were done with unpaired t-tests using SPSS (IBM, New York, USA). For all in vivo experiments, the group and sample sizes are indicated in each figure legend. The results are represented as mean ± standard deviation (SD). P-values of < 0.05 are considered as statistically significant (* $p < 0.05$; ** $p < 0.01$; *** $p < 0.001$; **** $p < 0.0001$).

3 Results

Parts of the presented results have recently been published in my paper (Merk et al., 2024).

3.1 Best preservation of fluorescence proteins in mouse brain tissue after 4% -PFA immersion fixation

The use of RGS5^{GPF+} pericyte reporter mice [from now on named RGS5 strain, (Nisancioglu et al., 2008)] and mCherry expressing GL261 mouse GBM cells, both of C57BL6 background, allows the simultaneous detection of GFP-expressing vessel-associated mural cells (VAMCs) and the mCherry positive GBM cells in this syngeneic mouse GBM model. However, the direct tracking of those cells necessitates the preservation of the expressed fluorescent proteins. Appropriate fixation is a crucial step for the correct detection of the proteins of interest. As chemical modifications of proteins resulting from different fixatives can mask the epitopes, change the protein conformation or result in loss of fluorescence, different fixation protocols can massively influence the detection (Scandella et al., 2020). In order to evaluate the best fixation method for preservation of fluorescence proteins, different fixatives and fixation methods (described in 2.2.6.1) were tested on RGS5 strain mice brains. The fixation method showing best preservation of immunofluorescent proteins with lowest background was selected for all further experiments. In snap frozen mouse brains as well as in 5 min and 10 min 4% PFA fixed brain slices, GFP signal was not sufficiently preserved and showed decreased intensity. Compared to all other fixation methods, acetone post-fixed slices showed blurred GFP signal with simultaneously high background, therefore not being suitable for fluorescence preservation. Although the tested fixation methods seem to preserve at least some fluorescence signal, the best signal brightness with simultaneously rare background was observed in brain slices which were fixated by 4% PFA immersion (Figure 4). Therefore, 4% PFA immersion fixation was chosen for all following experiments.

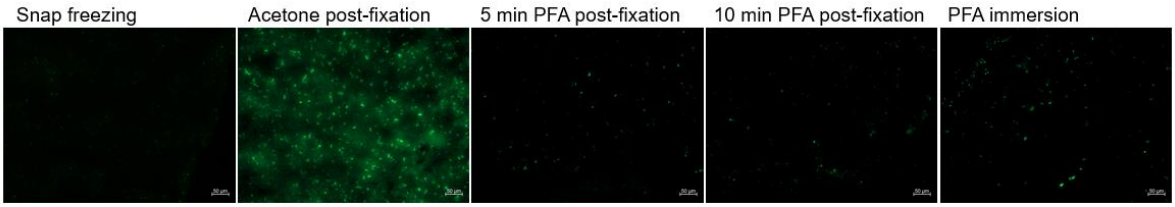

***Figure 4: Preservation of fluorescence proteins after different fixation methods**. Figure shows representative areas of unstained mouse brain tissue of the RGS5 strain. Five different fixation methods (Snap freezing, Acetone post-fixation, 5 min & 10 min 4% PFA post-fixation and 4% PFA immersion fixation) were analyzed for their preservation of the fluorescent protein GFP. 4% PFA immersion fixation showed best preservation with simultaneously lowest background signal. All images were taken with 10x magnification. Scale bars: 100 µm.*

In the RGS5 strain mice used in the experiments, the GFP expression was preserved in VAMCs. This was tested by pericyte isolation from mouse tissue with subsequent pericyte culture and fluorescence microscopy.

After 4% PFA immersion fixation, GFP was still nicely detectable. However, as the fluorescence faded over time, later on in tissues of experimental mice the GFP signal was amplified by immunofluorescence using a GFP specific antibody.

3.2 VAMCs are the source of PDGFRβ, αSMA and SLUG in GBM

Previous research has shown that TGF-β induces a mesenchymal phenotype in primary human microvascular brain pericytes (HBVPs) through the induction of an EMT-like program (Wirsik et al., 2021). Our earlier investigations have revealed a significant involvement of pericytes in the development of GBM-associated vascular proliferations. Those pericytes wrapping around GBM vessels exhibit a distinct expression profile compared to "normal" pericytes found in vessels outside the tumor region, especially in terms of EMT factors such as SLUG (Mäder et al., 2018), as well as the pericytic activation markers αSMA and PDGFRβ (Guerra et al., 2018; Wirsik et al., 2021). Hence, in this project, we sought to investigate the TGF-β-mediated effect on the expression of these proteins and therefore “activation” of VAMCs within GBM.

Therefore, IF staining protocols for the markers SLUG, αSMA, PDGFRβ and CD31, the latter highly expressed in endothelial cells and therefore suitable as a vascularization marker, were initially set up and optimized in collaboration with Katja Regel, Master-Student, under my direct supervision (Supplementary Figure 1, Supplementary Figure 2). This process is described in detail in her Master thesis.

Since VAMCs are defined by their perivascular position, adjacent to endothelial cells, combined CD31 and GFP staining of RGS5 strain mouse brain tissue was used to verify that VAMCs are the source of GFP (Figure 5). As indicated in Suppl. Fig. 4, GFP was only detected in cells enveloping $CD31^{+}$ endothelial cells. Figure 5 C notably shows the specificity of GFP positivity to mural cells located at the abluminal surface of endothelial cells.

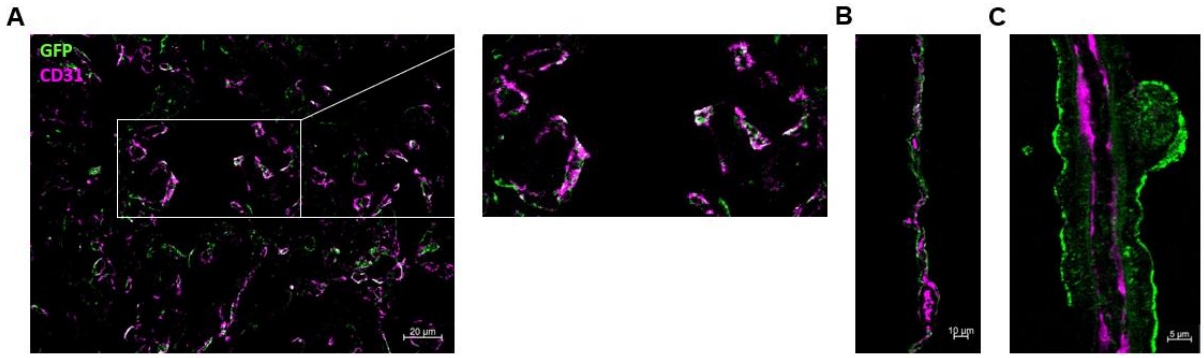

***Figure 5: Visualization of CD31 and GFP co-localization in mouse brain**. Figure shows representative areas of GFP and CD31 double staining on 10 µm sections of RGS5 strain mouse brain tissue bearing PAR GL261^{mCherry} GBM within the tumor area (A) or the contralateral hemisphere (B, C). GFP signal adjacent to CD31 positive vessels is shown (B). GFP positive cell wrapped around CD31-positive endothelial cell (C). Images were taken with 25x (A), 40x (B) and 100x (C) magnification. Scale bars: 20 µm, 10 µm, 5 µm (partly shown in Merk et al., 2024).*

As GFP was expressed by vessel-adjacent VAMCs, its´ localization was used in the following as a reference to identify the expression of other proteins in those cells. Hence, SLUG, αSMA and PDGFRβ were analyzed for co-localization with GFP. As SLUG, αSMA and PDGFRβ are known to be expressed by VAMCs, IF staining in RGS5 strain mouse brain tissue bearing a GBM developed from PAR cells was performed. Co-localization analyses of SLUG, αSMA, and PDGFRβ with GFP revealed a clear association of all three proteins with VAMCs (Figure 6), indicating that PDGFRβ, αSMA and SLUG specific fluorescence is almost exclusively

restricted to GFP$^+$ VAMCs adjacent to CD31$^+$ endothelial cells of glioma vascular proliferations. Whereas VAMCs in GBMs developed from PAR cells showed SLUG-, αSMA-, and PDGFRβ- expression, it was absent in the healthy brain hemisphere (Supplementary Figure 3).

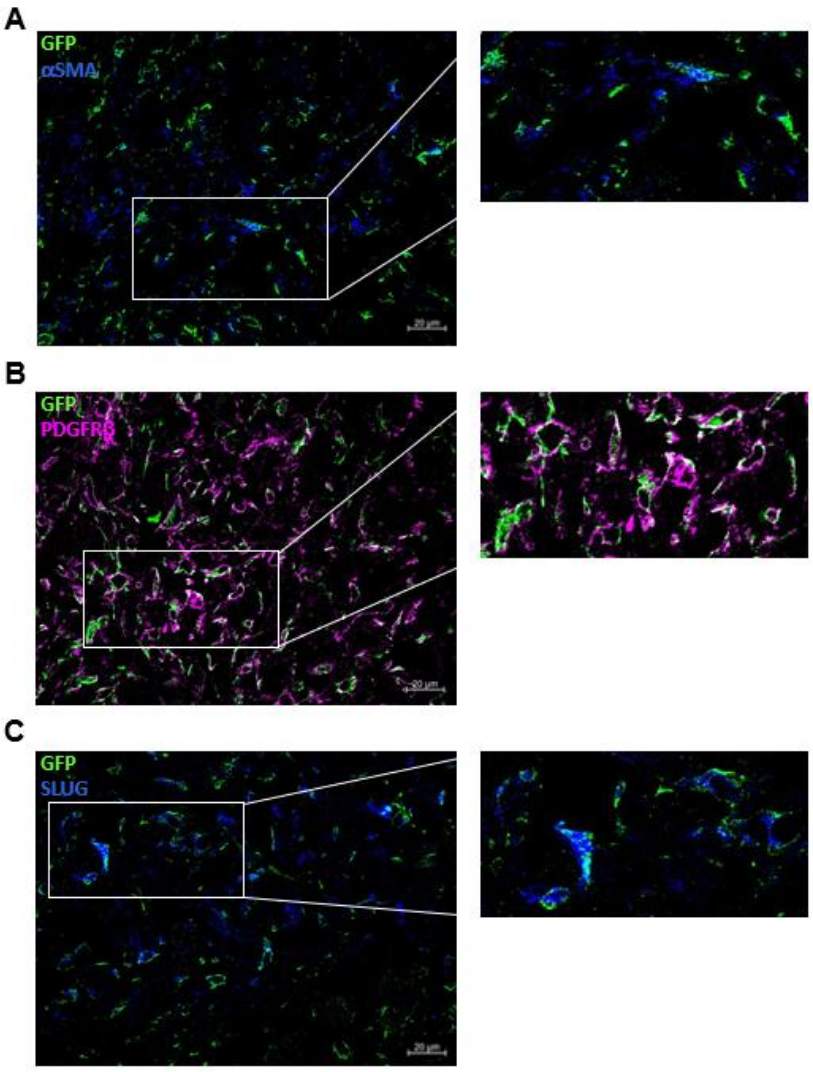

Figure 6: Visualization of GFP and PDGFRβ, αSMA or SLUG in RGS5 strain mouse brain bearing a PAR cell developed GBM*. Figures show double staining of GFP plus αSMA (A), GFP plus PDGFRβ (B) and GFP plus SLUG (C) in representative areas of brain tissue. All images were taken with 40x magnification. Scale bars: 20 µm.*

Moreover, the qualitative analyses revealed that co-localization of the above-mentioned proteins were not only seen with GFP, but also between PDGFRβ and αSMA or PDGFRβ and SLUG (Figure 7).

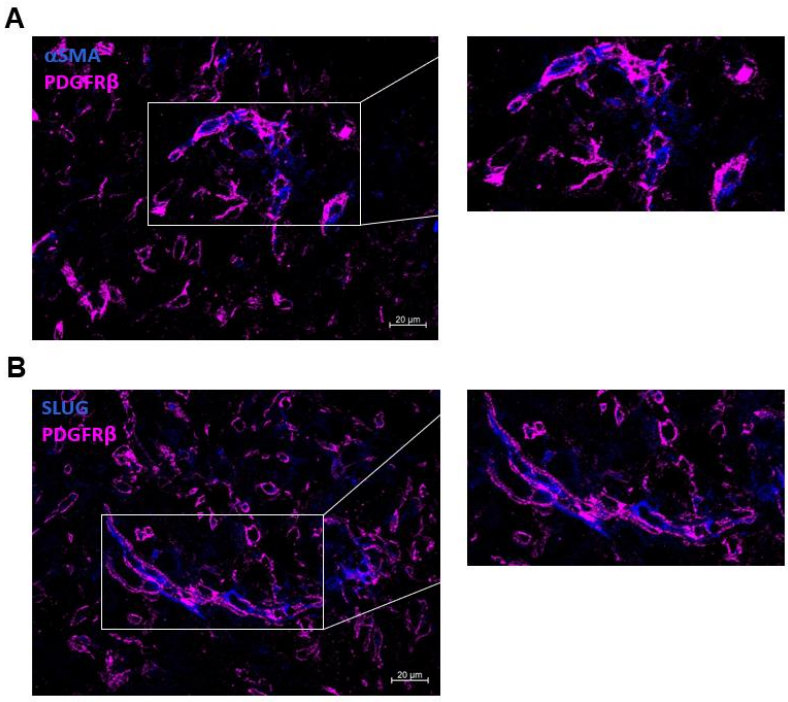

Figure 7: Visualization of PDGFRβ co-staining with αSMA or SLUG in RGS5 strain mouse brain bearing a PAR developed GBM*. Pictures show representative areas of PDGFRβ plus αSMA (A) and PDGFRβ plus SLUG (B) double stainings. All images were taken with 40x magnification. Scale bars: 20 µm.*

To determine that the EMT-factor SLUG that we detected in VAMCs was absent in GBM cells (as shown for human GBMs by Wirsik et al., 2021 and Mäder et al., 2018), SLUG and GFP fluorescence was examined in relation to mCherry which is expressed in the tumor cells. Whereas SLUG showed strong co-localization with GFP, neither SLUG nor GFP signal matched with mCherry (Figure 8). This clearly demonstrated that within the tumor area VAMCs and not GBM cells are the source of SLUG. These results have been published in Merk et al., 2024.

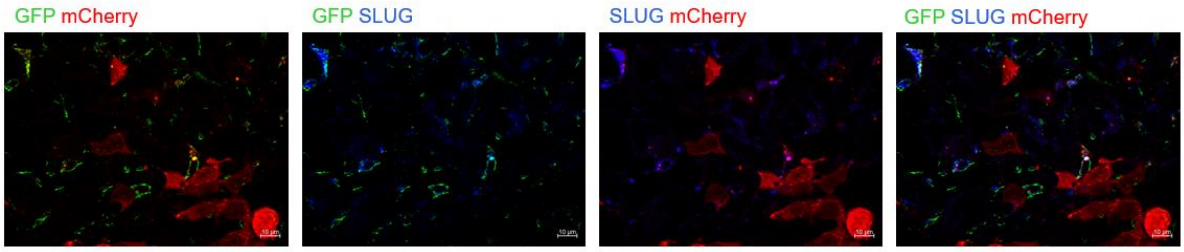

Figure 8: VAMCs, but not GBM cells are the source of GFP and SLUG. *Pictures show representative areas of GFP plus mCherry, GFP plus SLUG, SLUG plus mCherry stainings or the overlay of all three proteins in RGS5 strain mice bearing a PAR cell developed GBM. All images were taken with 63x magnification. Scale bars: 10 µm (Merk et al., 2024).*

As these data (I) are concordant with the presence of PDGFRβ and αSMA that were already identified in VAMCs of human GBM patients and (II) as it has been shown that the knockdown of SLUG in human brain microvascular pericytes (HBVP) *in vitro* inhibits TGF-β induced cell migration and proliferation (Mäder et al., 2018; Wirsik et al., 2021), those proteins are feasible as indicators for pericyte activation. Therefore, in the following analyses, the parallel detection of SLUG, PDGFRβ and αSMA was used to identify VAMCs activation.

3.3 Comparison of tumor growth characteristics of PAR and TGF-β-Knockout (TGF-β-KO) GBMs

In GBM, TGF-β is known to be a potent pro-tumorigenic cytokine which is secreted in large amounts by these tumor cells. TGF-β has already been shown to induce SLUG expression in pericytes *in vitro*, resulting in enhanced proliferation and cell motility (Wirsik et al., 2021). Additionally, TGF-β negatively modulates the function of pericytes as keepers of the blood brain barrier integrity (Schumacher et al., 2023). Therefore, we were interested whether those changes we observed *in vitro* also reflect the *in vivo* situation. To examine the impact of GBM secreted TGF-β1 and -β2 (from now on named TGF-β) on pericytes, TGF-β1 plus -β2 knockout (TGF-β-KO) GL261^{mCherry} GBM cells were generated by CRISPering GL261^{mCherry} GBM cells and were further characterized by Hermann Eckhardt in our Laboratory as a part of his medical doctoral project. *In vitro*, TGF-β-KO GL261^{mCherry} GBM cells showed a significant lower proliferation capacity. Their growth was further determined *in vivo* by contrast enhanced MRI in RGS5 strain mice after intrastriatal implantation. These experiments were performed in collaboration with Dr. Marcel Krüger at the Werner Siemens Imaging Center Tübingen prior to the experiments described in this thesis. Compared to PAR, TGF-β-KO GBM cells indeed need twice the time to reach comparable sizes in RGS5 strain mice. Hence, mice bearing PAR tumors were sacrificed 29 and mice bearing TGF-β-KO tumors 59 days post GBM cell implantation (Merk et al., 2024). To that timepoint the tumors grew up to a size of approximately 1.5 - 2.5 mm in diameter. The visualizing of mCherry-expressing GBM

cells allows us to clearly identify the tumor area and to distinguish it from the adjacent healthy brain parenchyma (Figure 9).

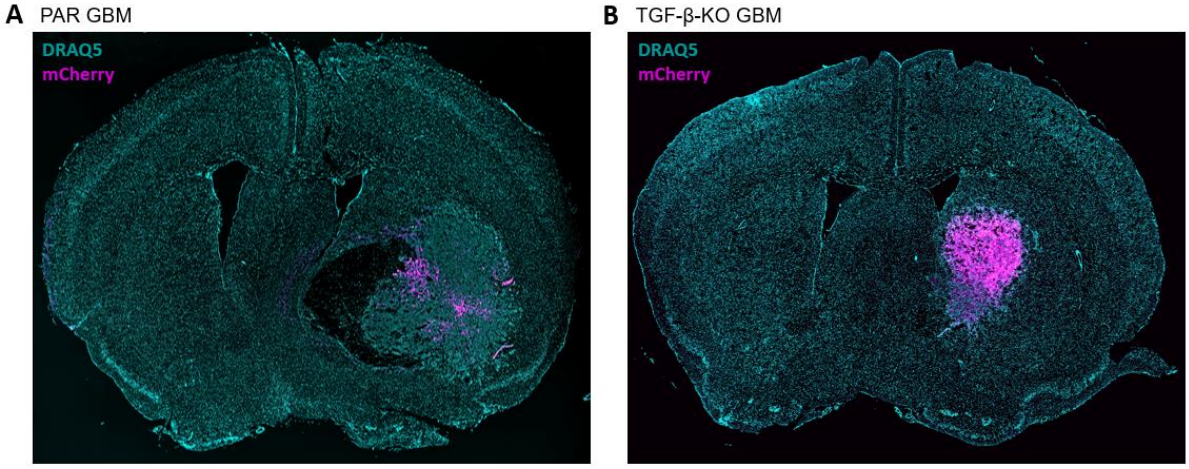

***Figure 9: Localization of PAR (A) or TGF-β-KO (B) GBM in the brain of RGS5 strain mice**. Tumor localization (magenta, mCherry) is exemplarily shown for one mouse per group. Nuclear stain (DRAQ5) was performed on 10 µm sections of RGS5 strain mouse brains bearing either PAR (A) or TGF-β-KO (B) GBM. Images were taken as tile scan with 10x magnification using a Leica DMI8 microscope.*

Tumor infiltration zones and core regions were further identified to compare growth characteristic of PAR and TGF-β-KO GBMs. Even though tumor cell density and size showed intertumoral variability, the comparison of tumor size of all PAR and all TGF-β-KO GBM revealed no significant difference ($p > 0,05$) which will be of importance for processes of tumor-associated neo-angiogenesis we investigated in this project. Interestingly, PAR GBMs showed a slightly more invasive growth pattern than the TGF-β-KO tumors whose cells cluster closer together (Figure 10).

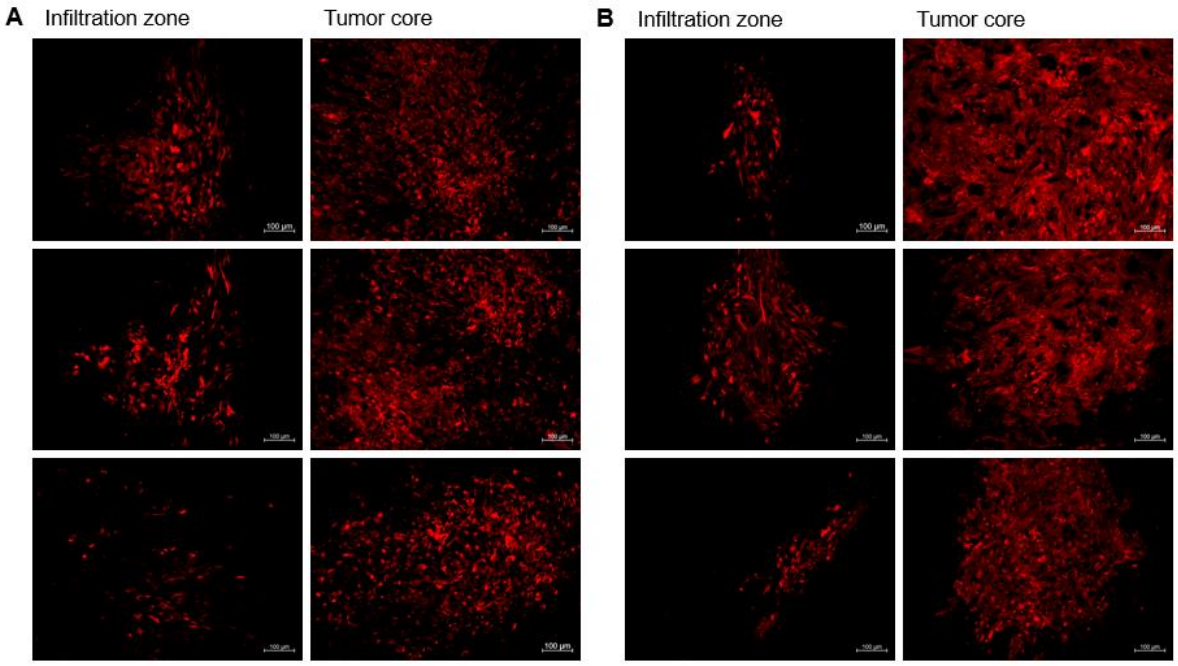

Figure 10: Identification of infiltration zones and tumor core regions for PAR (A) or TGF-β-KO GBMs (B). *The tumor core and infiltration zones were visualized by detection of mCherry in the brain of RGS5 strain mice bearing either a PAR (A) or a TGF-β-KO GBM (B). Three different mice per group are shown from the upper to the lower panel. All images were taken with 10x magnification. Scale bars: 100 µm.*

3.4 VAMCs in TGF-β-KO GBM present a lesser mesenchymal phenotype

The use of TGF-β-KO cells allowed us to examine if the expression of SLUG, PDGFRβ and αSMA, characterizing the mesenchymal phenotype of VAMCs, is induced by GBM-cell secreted TGF-β (Wirsik et al., 2021). Therefore, by IF staining, we investigated whether the absence of TGF-β in TGF-β-KO cell derived GBMs modulates the expression of the above-mentioned proteins in VAMCs.

In TGF-β-KO GBM bearing mice brains the amount of SLUG or αSMA positive tumor-associated VAMCs was significantly reduced compared to mice bearing a PAR cell derived GBM. In line with the reduction of αSMA and SLUG positive VAMCs, a significant decrease could also be seen for PDGFRβ positive VAMCs located in or adjacent to a TGF-β-KO GBM (Figure 11, Figure 12).

In addition to the reduction of αSMA, SLUG and PDGFRβ positive VAMCs, significantly lower numbers of GFP^+ VAMCs were detected in TGF-β-KO GBMs

(Figure 11, Figure 12). This demonstrates that SLUG expression correlates with VAMCs density and their expression of PDGFRβ and αSMA.

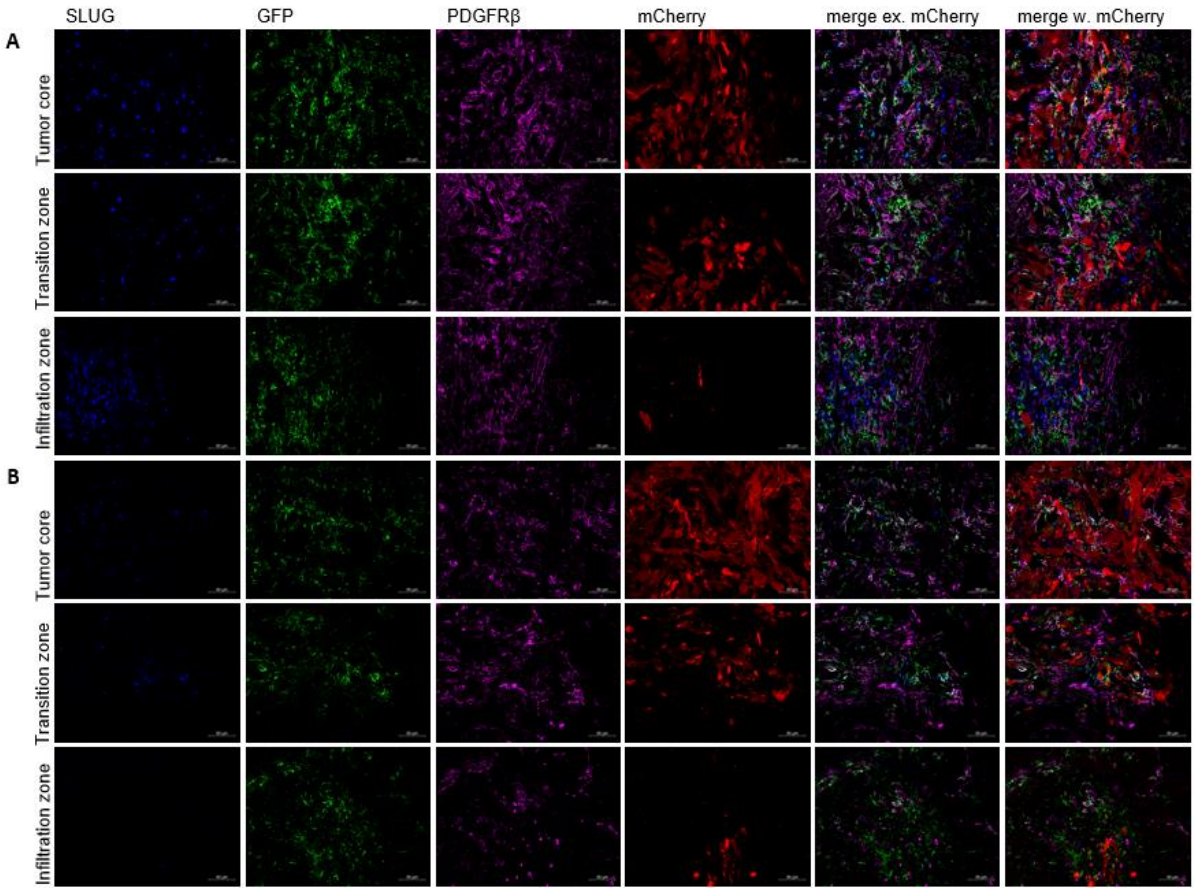

Figure 11: Visualization of SLUG, GFP and PDGFRβ in RGS5 strain mice bearing either a PAR (A) or a TGF-β-KO GBM (B)*. The pictures show SLUG, GFP and PDGFRβ fluorescence in representative areas for the tumor core, the transition and infiltration zone (exemplarily pictures of one mouse per group are shown). Merge pictures show overlays of all stainings including the tumor (merge w. mCherry) or excluding GBM cells (merge ex. mCherry). Stainings were performed by Katja Regel under my supervision. All images were taken with 25x magnification (n= 3 mice per group; Scale bars: 50 µm).*

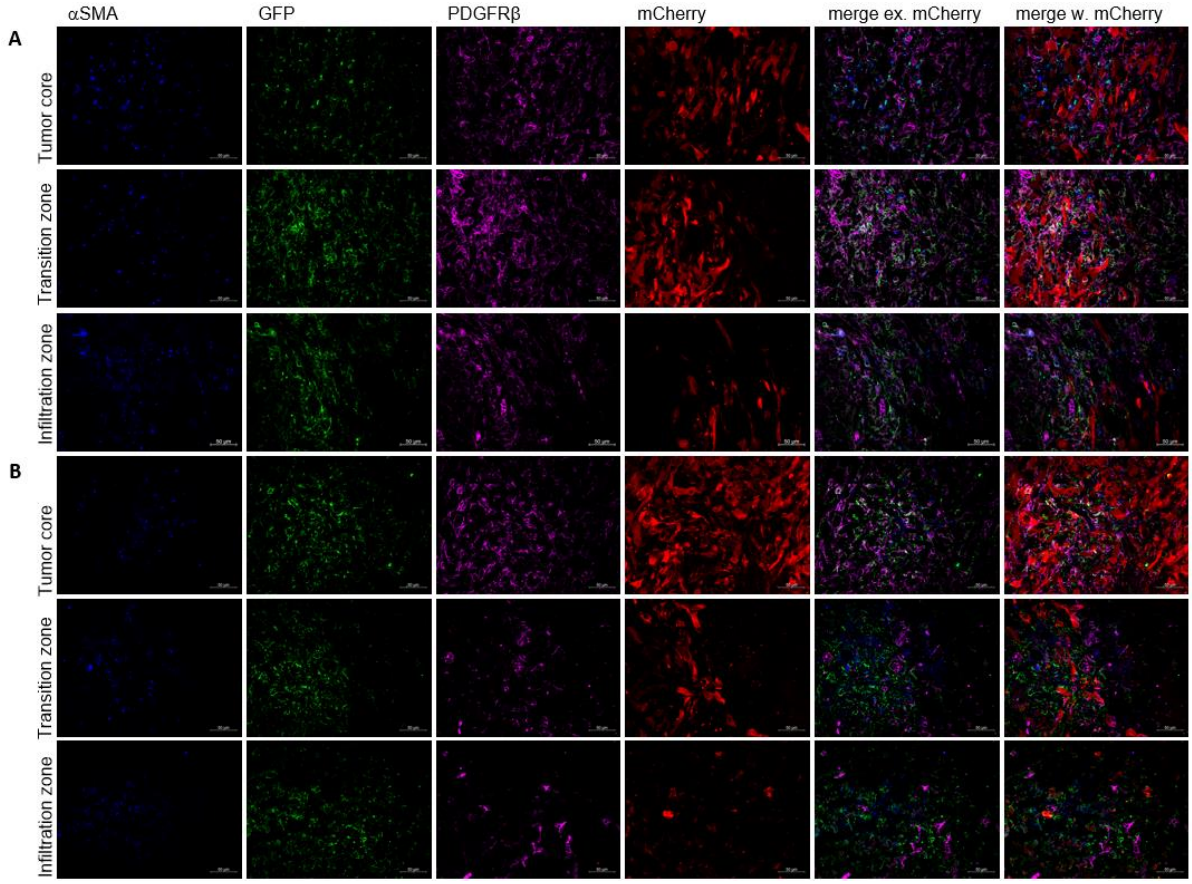

Figure 12: Visualization of αSMA, GFP and PDGFRβ in RGS5 strain mice bearing either a PAR (A) or a TGF-β-KO GBM (B)*. Figure shows αSMA, GFP and PDGFRβ fluorescence in representative areas for the tumor core, the transition and infiltration zone (exemplarily pictures of one mouse per group are shown). Merge pictures show overlays of all stainings including the tumor (merge w. mCherry) or excluding GBM cells (merge ex. mCherry). Stainings were performed by Katja Regel under my supervision. All images were taken with 25x magnification (n=3 mice per group; Scale bars: 50 µm).*

VAMCs with strong and specific fluorescence for PDGFRβ plus SLUG or for PDGFRβ plus αSMA were detected in PAR GBMs. Compared to PAR GBMs, the number of GFP-PDGFRβ-SLUG and GFP-PDGFRβ-αSMA triple positive cells, indicating activated VAMCs, were significantly reduced in both the tumor core as well as in the infiltration zones in TGF-β-KO GBMs. Analyses for PDGFRβ were done under my supervision by Katja Regel as a part of her Master thesis.

To further evaluate differences in the amount of GFP, PDGFRβ, αSMA and SLUG positive cells, by using ImageJ the fluorescence signal was quantified within the tumor area by measuring the area (%Area) that is covered by the respective fluorescence signal of the specific protein. As visualized in Figure 13, all proteins

display a significantly larger area in PAR GBM compared to TGF-β-KO GBM, indicating that the absence of TGF-β in GBM cells prevents excessive activation of VAMCs. These results have been published in a modified form in Merk et al., 2024.

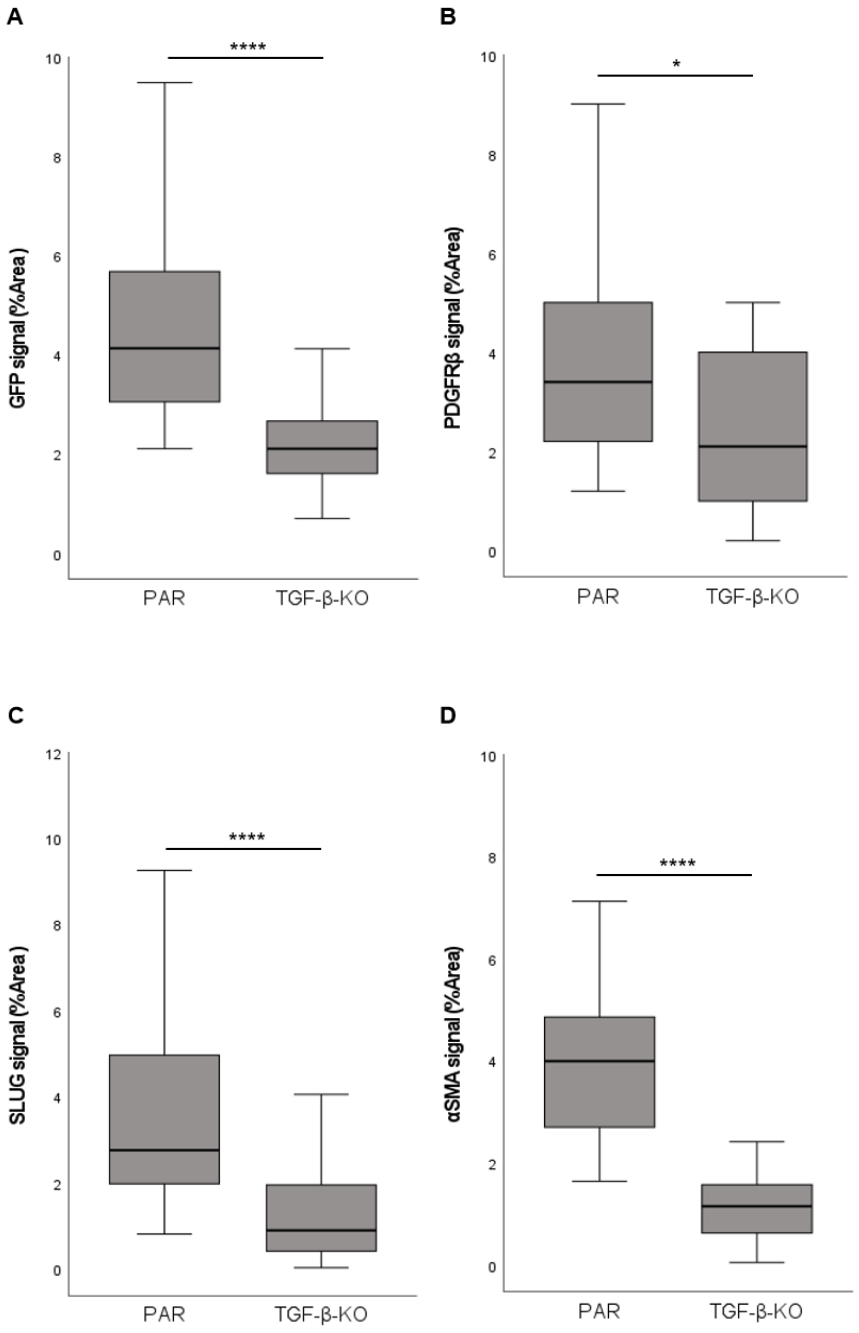

Figure 13: The absence of TGF-β in GBM cells significantly reduces the amount of VAMCs in the tumor area as well as the amount of PDGFRβ, αSMA and SLUG. *Quantification of VAMCs (GFP, A), PDGFRβ (B), αSMA (C) and SLUG (D) positive cells in the tumor area of RGS5 strain mice bearing either PAR or TGF-β-KO GBMs reveals highly significant reduction of these proteins in TGF-β-KO tumors (unpaired t-test, mean ± SEM are shown, n = 3 mice per group, in total 72 (GFP) or 36 (αSMA, PDGFRβ and SLUG) images were analyzed, **** p < 0.0001, * p < 0,05) (data shown in Merk et al., 2024).*

3.5 TGF-β-KO in GBM cells impairs tumor vascularization

As GBM is a highly vascularized tumor and pericytes are known to influence angiogenic processes (Fisher, 2009), we analyzed the impact of the TGF-β-KO in GBMs on the tumor vessel architecture. We were interested whether the differences we observed for PDGFRβ and αSMA in TGF-β-KO compared to PAR tumors are associated with the chaotic, glomeroid, garland-like and often dysfunctional vascular structure of GBM-associated vessels (Bergers & Song, 2005). The endothelial cell marker CD31 was used to characterize the tumor vasculature. Vessel density and structure in PAR and TGF-β-KO GBM were compared.

Compared to PAR GBMs, in all tumor regions, a notable reduction in CD31 fluorescence was detected in TGF-β-KO tumors. However, this reduction was more pronounced in transition and infiltration zones (Figure 14).

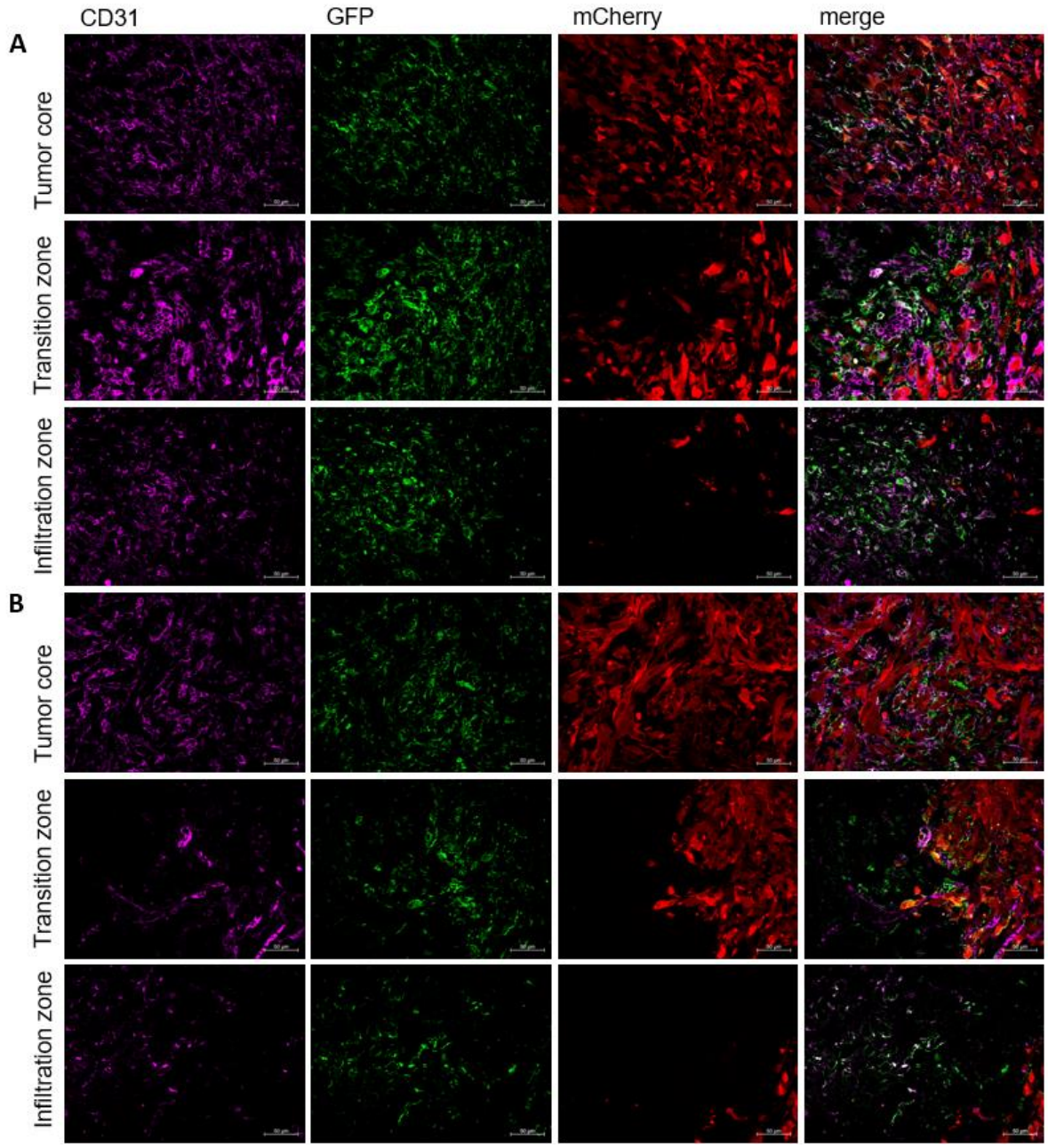

Figure 14: Identification of CD31 positive cells in either PAR (A) or TGF-β-KO GBMs (B). *Pictures exemplarily show GFP, CD31 and mCherry fluorescence in representative areas for the tumor core, the transition and infiltration zone in RGS5 strain mice bearing either PAR (A) or TGF-β-KO GBMs (B). All images were taken at 25x magnification (n=3 mice per group; Scale bars 50 µm) (partly shown in Merk et al.,2024).*

These findings were further supported by the quantification of CD31 positive cells, confirming the highly significant differences in vessel density of PAR and TGF-β-KO tumors that were already visible in the IF images. Mice bearing TGF-β-KO GBM showed a definite reduction of vessel density (2 times less than PAR GBM bearing

mice). However, when taking the non-tumor-bearing hemisphere as a reference, endothelial cell density was still significantly lower in the healthy brain than in the tumor area, independent whether the tumor secrets TGF-β or not (Figure 15).

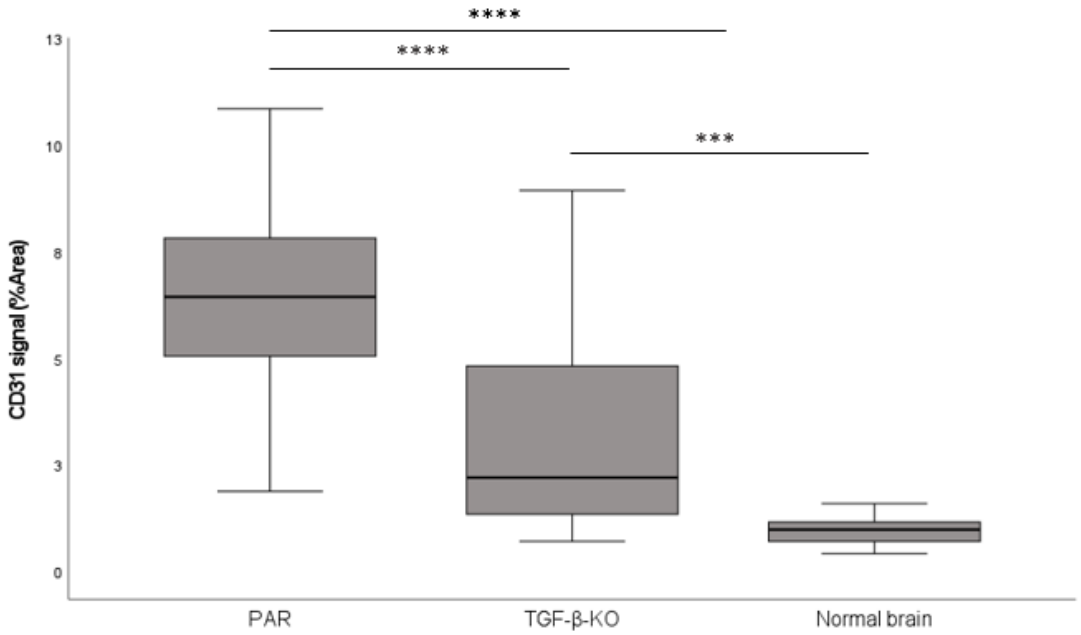

Figure 15: The missing secretion of TGF-β by TGF-β-KO GBMs results in a significantly reduced intratumoral vessel density. *Quantification of CD31 fluorescence in the brains of RGS5 strain mice bearing either PAR or TGF-β-KO tumors. TGF-β-KO tumors showed significant reduction of CD31 fluorescence compared to PAR GBM. However, CD31 fluorescence is still significantly elevated in both tumor types compared to the non-tumor bearing hemisphere (n= 3 mice per group, in total n=72 images per experimental group and n=24 images for the non-tumor bearing hemisphere were analyzed, unpaired t-test, means ± SEM are shown, **** p < 0.0001, *** p < 0,001) (data shown in Merk et al., 2024).*

Further, vessels of PAR cell derived GBMs clearly exhibited pronounced structural alterations consisting of vascular tangles or glomeroid-like formations (Figure 14). They appeared more “net-like” and closer together than the vessels found in TGF-β-KO tumors. In PAR cell derived GBMs, the vasculature exhibited not only a higher vessel density compared to TGF-β-KO cell-derived GBMs but also greater variability in vessel diameter (Supplementary Figure 4, Supplementary Figure 5). TGF-β-KO GBMs displayed less pronounced structural vessel abnormalities and a decreased number of VAMCs compared to PAR GBMs. “However, the intratumoral vessels were still chaotically organized compared to the vascular structure of the brain in the contralateral, tumor-free hemisphere of the same animal” (cited from Merk et al., 2024). These results have recently been published in Merk et al., 2024.

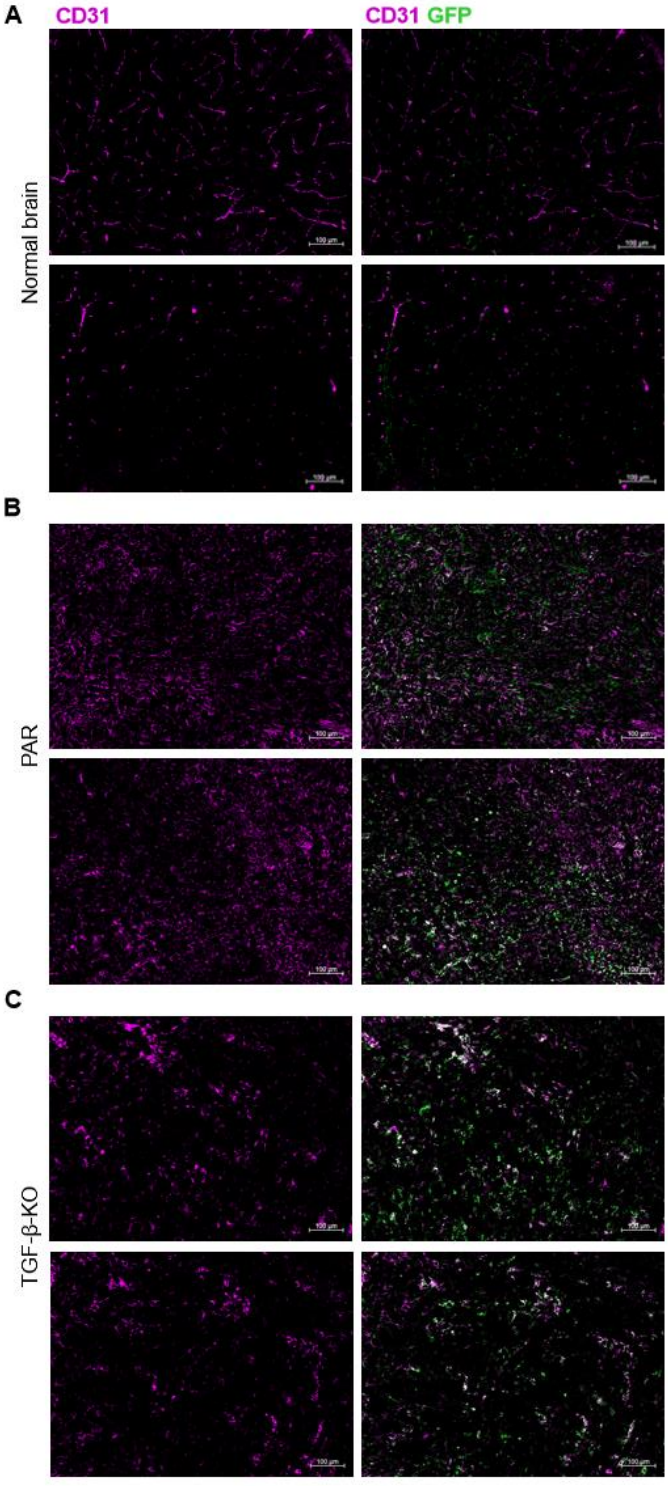

Figure 16: Vessel density in the non-tumor bearing brain hemisphere (A) or in the tumor area of PAR (B) and TGF-β-KO GBM (C). *Endothelial cells identified by CD31 fluorescence (magenta, left panels) and co-localization of GFP+ VAMCs with endothelial cells (right panels) is exemplarily shown. Mice bearing TGF-β-KO tumors showed a noticeable reduction of vessel density and number of VAMCs compared to PAR tumors. However, none of the tumors reached the basal CD31 fluorescence level detected in the non-tumor-bearing brain parenchyma. All images were taken at 10x magnification (n=3 mice per group; Scale bars: 100 µm) (partly shown in Merk et al., 2024).*

Along with the CD31 positivity, the number of glioma-associated VAMCs was dramatically enhanced in PAR GBMs compared to the non-tumor-bearing normal brain. In addition, VAMCs of PAR tumor associated vessels seemed to be more loosely attached to endothelial cells. This was also observed in TGF-β-KO GBMs, however to a lesser extent. In contrast to PAR GBM, the VAMCs density in TGF-β-KO GBMs was significantly reduced. Further, the inconsistent and partly increased vessel coverage by VAMCs observed in PAR GBM was less pronounced if TGF-β is absent (Figure 17).

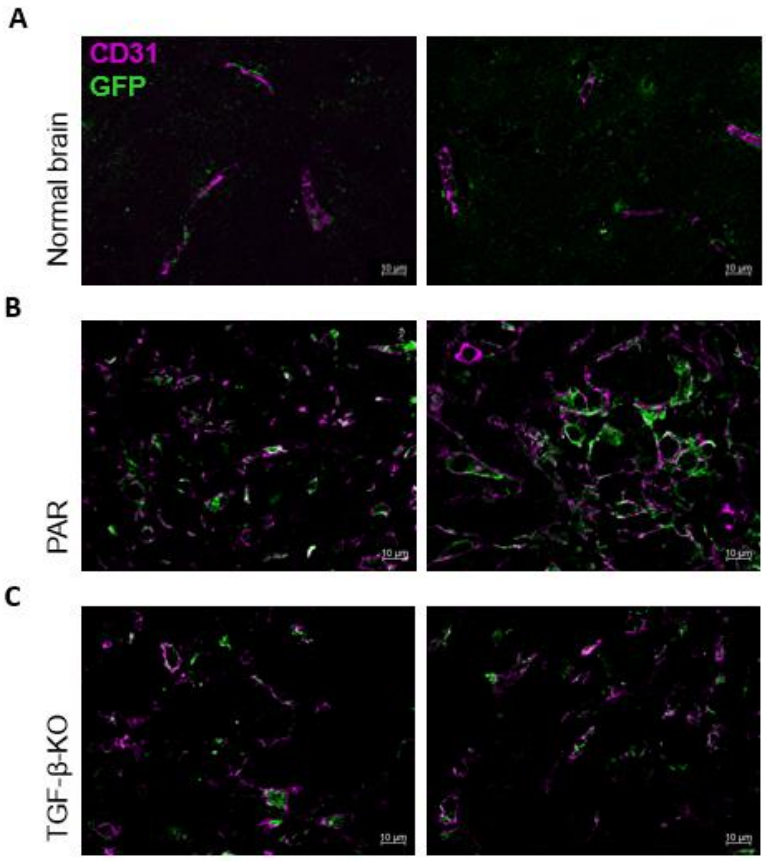

***Figure 17: Visualization of vessel structure and VAMCs coverage**. Vascular structure consisting of endothelial cells (CD31) and adjacent VAMCs (GFP) is exemplarily shown in RGS5 strain mice for the tumor-free hemisphere (A) compared to PAR (B) and TGF-β-KO (C) GBMs. All images were taken at 63x magnification (n=3 mice per group; Scale bars: 10 µm) (partly shown in Merk et al., 2024).*

Additional IF analyses demonstrated that CD31 fluorescence and by this vessel density also strongly correlated with that of the pericyte markers SLUG, αSMA and GFP (Supplementary Figure 4-7). Elevated number of SLUG and αSMA positive

cells are therefore associated with altered growth characteristics of VAMCs and augmented vessel disorganization. These results have recently been published in Merk et al., 2024.

3.6 GBM growth after VAMC-specific SLUG KO

As it has been described that GBM-secreted TGF-β induces SLUG expression and subsequent activation of HBVPs, at least *in vitro* (Wirsik et al., 2021), we next were interested to examine whether abolishing the induction of SLUG in tumor-adjacent VAMCs could prevent the TGF-β-mediated effects on pericytes. To investigate the effect of SLUG-mediated signaling on VAMC activation *in vivo*, the GBM/TGF-β-mediated upregulation of SLUG in VAMCs was inhibited. By intrastriatal injection of a mixture of three lentiviruses (Lenti-RGS5-CRISPR-SLUG 1, 4 and 5) that express CAS9 under the control of the RGS5-promoter as well as sgRNAs specific for murine SLUG, a VAMC-specific knockout of SLUG (SLUG-KO) was performed in the brain of RGS5 strain mice. The mixture contained about 3 x 10^5 IV/ml of each Lenti-RGS5-CRISPR-SLUG 1, 4 and 5. Equivalent infectious virus particles of Lenti-CRISPR V2 (empty vector control, from now on named Lenti-V2) were used in the control group. Three days after lentivirus injection, all mice received an injection of PAR GBM cells at the same brain location the viruses were injected. The mice were sacrificed when developing the first tumor related symptoms which was 25 days after tumor cell implantation for animals receiving Lenti-V2 and 60 days for animals receiving Lenti-SLUG-KO virus (from now on named SLUG-KO). Like for TGF-β-KO GBMs, tumor growth was compared between both groups to exclude an impact of tumor size on tumor angiogenesis. Although the individual tumors were heterogeneous in their GBM cell distribution, there was no significant overall difference in their size ($p > 0,05$) (Figure 18).

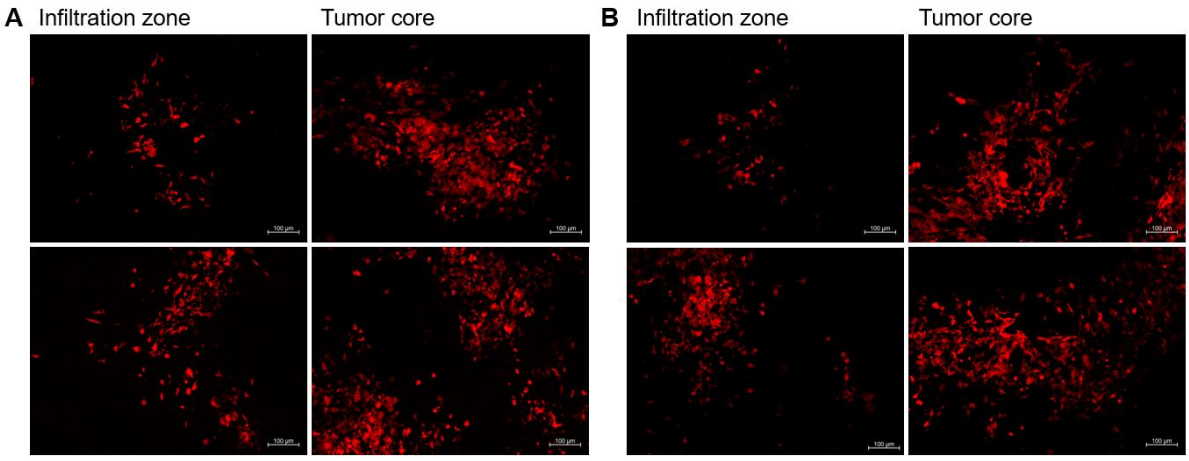

***Figure 18: Representative infiltration zones and tumor core regions of control and SLUG-KO mice**. Tumor core and infiltration zones were visualized by detection of mCherry after either (A) V2 lentivirus injection or (B) SLUG-KO lentivirus injection. Tumor core and infiltration zone of two mice per group are shown (upper and lower panel). All images were taken with 10x magnification. Scale bars: 100 µm.*

3.7 Inhibiting SLUG expression in VAMCs diminishes their mesenchymal signature

First, the knockout of SLUG was verified by comparing SLUG fluorescence within the tumor area in mice that received either the Lenti-V2 or Lenti-SLUG-KO. In SLUG-KO mice, SLUG expression was not detectable (Figure 19). This indicated that within the injection area, Lenti-SLUG-KO resulted in a localized knockout of SLUG in VAMCs, by this prohibiting a TGF-β-induced SLUG expression in these cells.

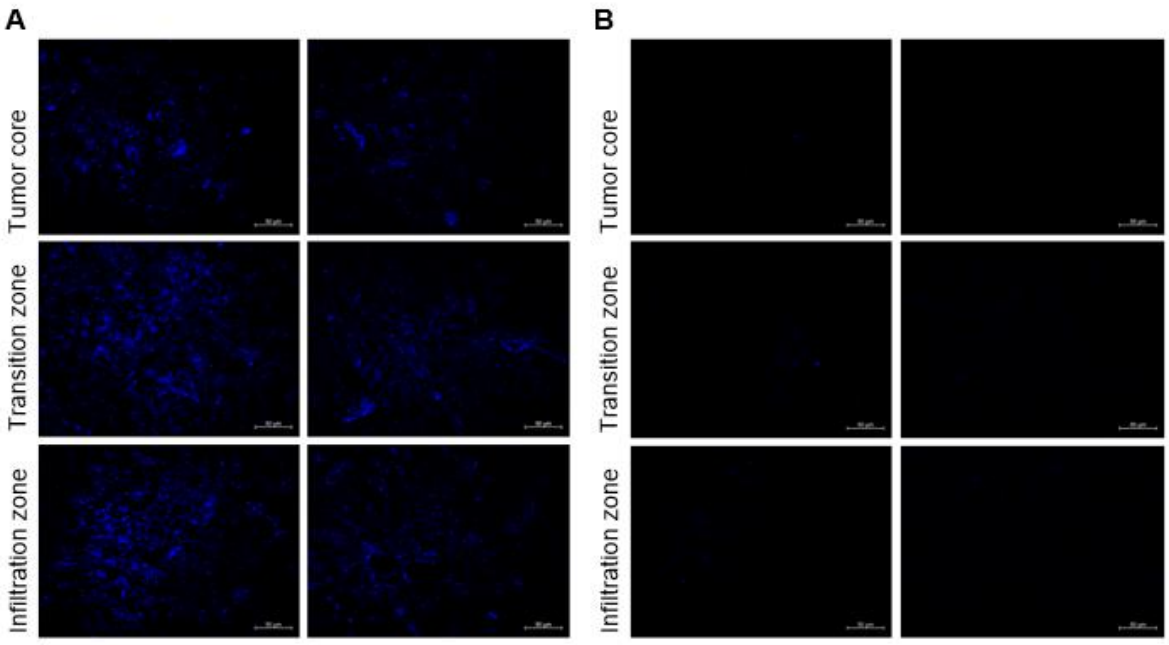

Figure 19: Evaluation of the SLUG knockout in tumor adjacent VAMCs of RGS5 strain mice bearing PAR tumors. *SLUG fluorescence in the tumor core, transition and infiltration zone of RGS5 strain mice bearing PAR tumors and that received either an intrastriatal injection of Lenti-V2 (A) or Lenti-SLUG-KO (B) prior to tumor cell implantation. Representative pictures of two mice per group are shown. All images were taken with 25x magnification. Scale bars: 50 µm.*

Given the knockout of SLUG in the Lenti-SLUG-KO virus treated mice, the correlation to αSMA and PDGFRβ, known to be upregulated in parallel to SLUG, was examined. In different tumor regions a significant reduction of αSMA and PDGFRβ was seen in those mice that received Lenti-SLUG-KO prior to tumor cell implantation. This was not the case if the mice received Lenti-V2. SLUG expression has consistently been shown to strongly correlate with PDGFRβ (Figure 20) and αSMA (Figure 21). Further analyses in VAMCs supporting the statement that SLUG strongly correlates with αSMA, PDGFRβ and GFP are shown in Supplementary Figure 12-15.

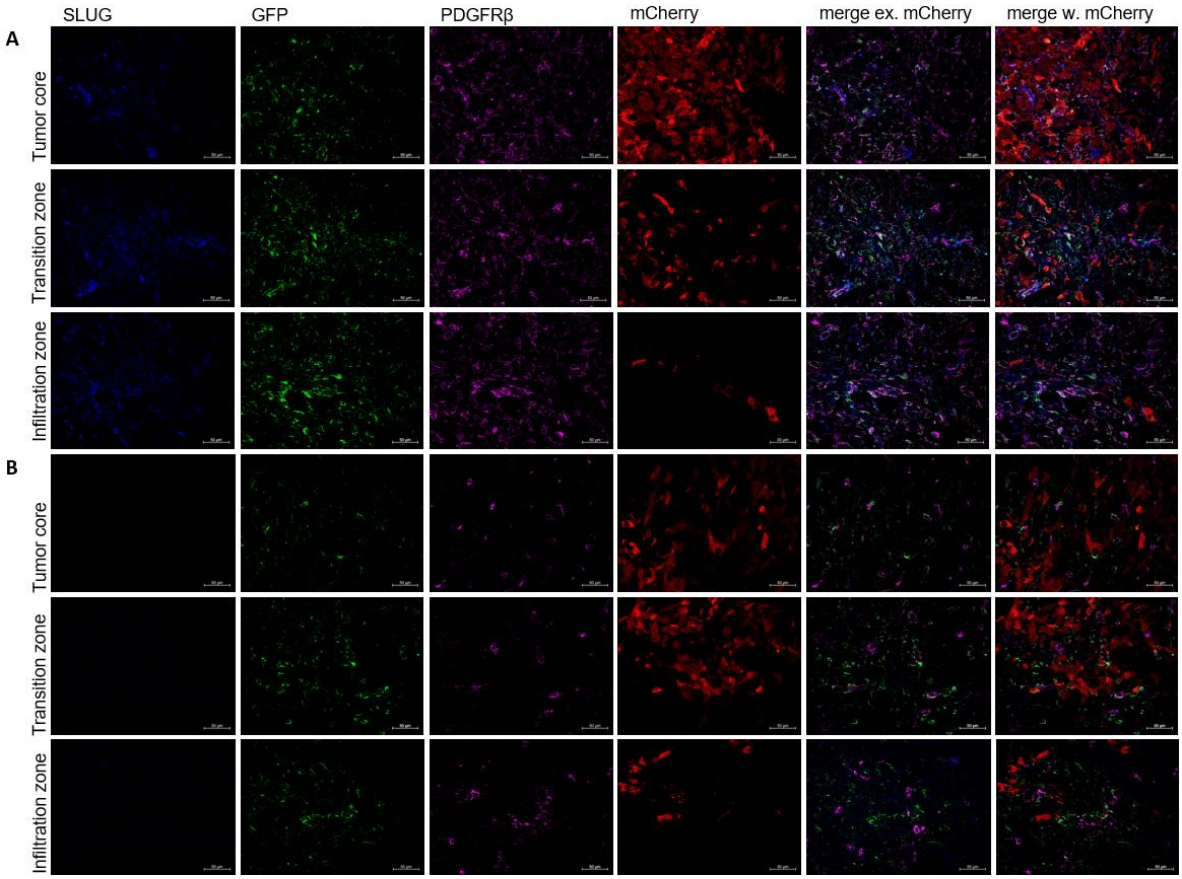

Figure 20: Visualization of SLUG, GFP and PDGFRβ positive cells in RGS5 strain mice bearing PAR GBM that received an intrastriatal injection of either Lenti-V2 (A) or Lenti-SLUG-KO (B). *Photographs exemplarily show SLUG, GFP and PDGFRβ in representative areas for tumor core, transition and infiltration zone. Marker co-localization is shown in merge with (merge w. mCherry) and without (merge ex. mCherry) the GBM cells. All images were taken with 25x magnification (n=2 mice per group; scale bars: 50 µm) (partly shown in Merk et al., 2024).*

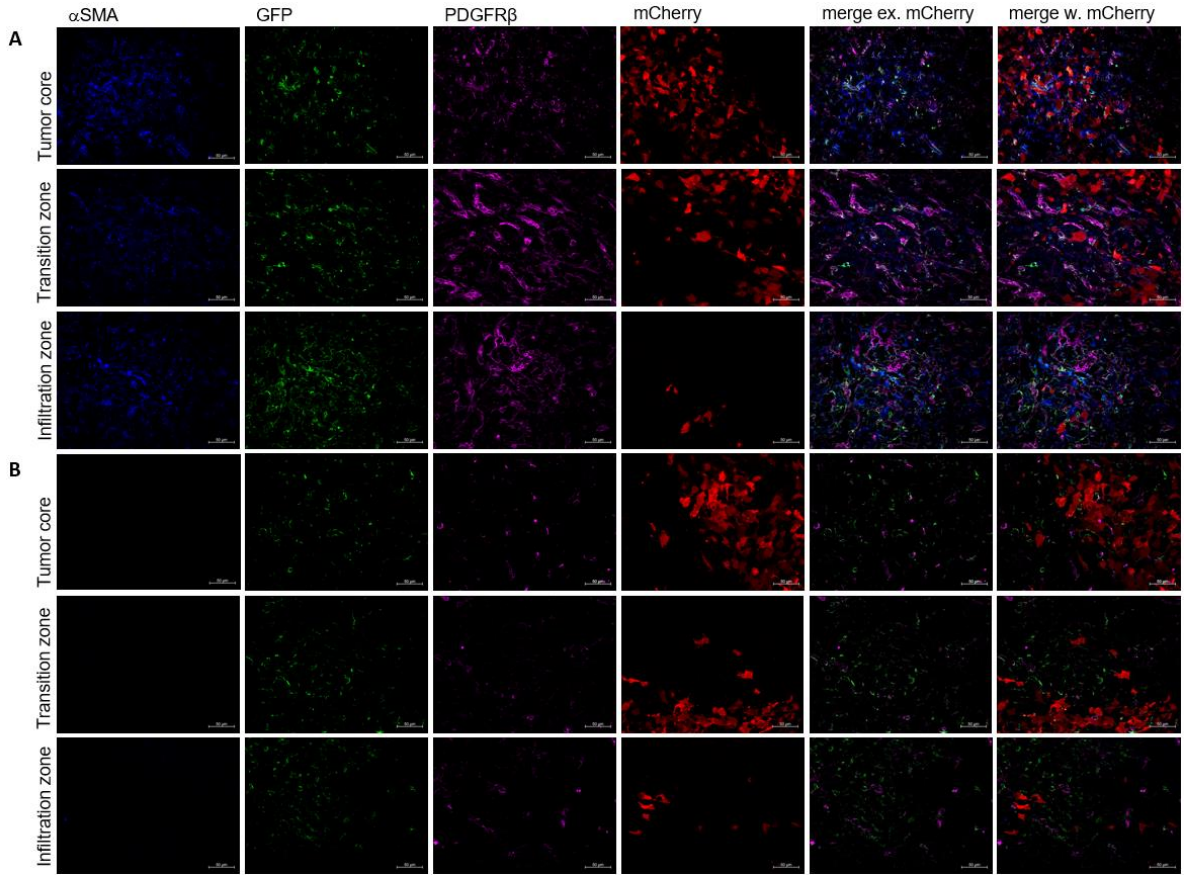

Figure 21: Visualization of αSMA, GFP and PDGFRβ positive cells in RGS5 strain bearing PAR GBM that received an intrastriatal injection of either Lenti-V2 (A) or Lenti-SLUG-KO (B). *Photographs show αSMA, GFP and PDGFRβ positive cells in representative areas for tumor core, transition and infiltration zone. Marker co-localization is shown in merge with (merge w. mCherry) and without (merge ex. mCherry) visualizing the tumor. All images were taken with 25x magnification (n=2 mice per group, pictures of one animal are exemplarily shown, scale bars: 50 µm) (partly shown in Merk et al., 2024).*

The differences between Lenti-V2 and the Lenti-SLUG-KO injected animals were further evaluated by quantification of GFP, PDGFRβ, αSMA and SLUG fluorescence within the tumor area. Percentage of area (%Area, ImageJ) of marker signal was used to determine the amount of positive cells. Consistently, all markers were significantly reduced in the SLUG-KO compared to the Lenti-V2 treated animals ($p < 0.0001$, Figure 22). After knocking out SLUG specifically in VAMCs, almost no αSMA fluorescence was detectable, whereas a decent PDGFRβ signal was traceable. The number of GFP^+ VAMCs were notably reduced in Lenti-SLUG-KO injected animals, though to a significant smaller amount than determined for αSMA and PDGFRβ. This suggests that VAMCs remained covering tumor vessels,

however they seem to display a “more normal” phenotype instead of the mesenchymal phenotype that we observed in Lenti-V2 injected animals.

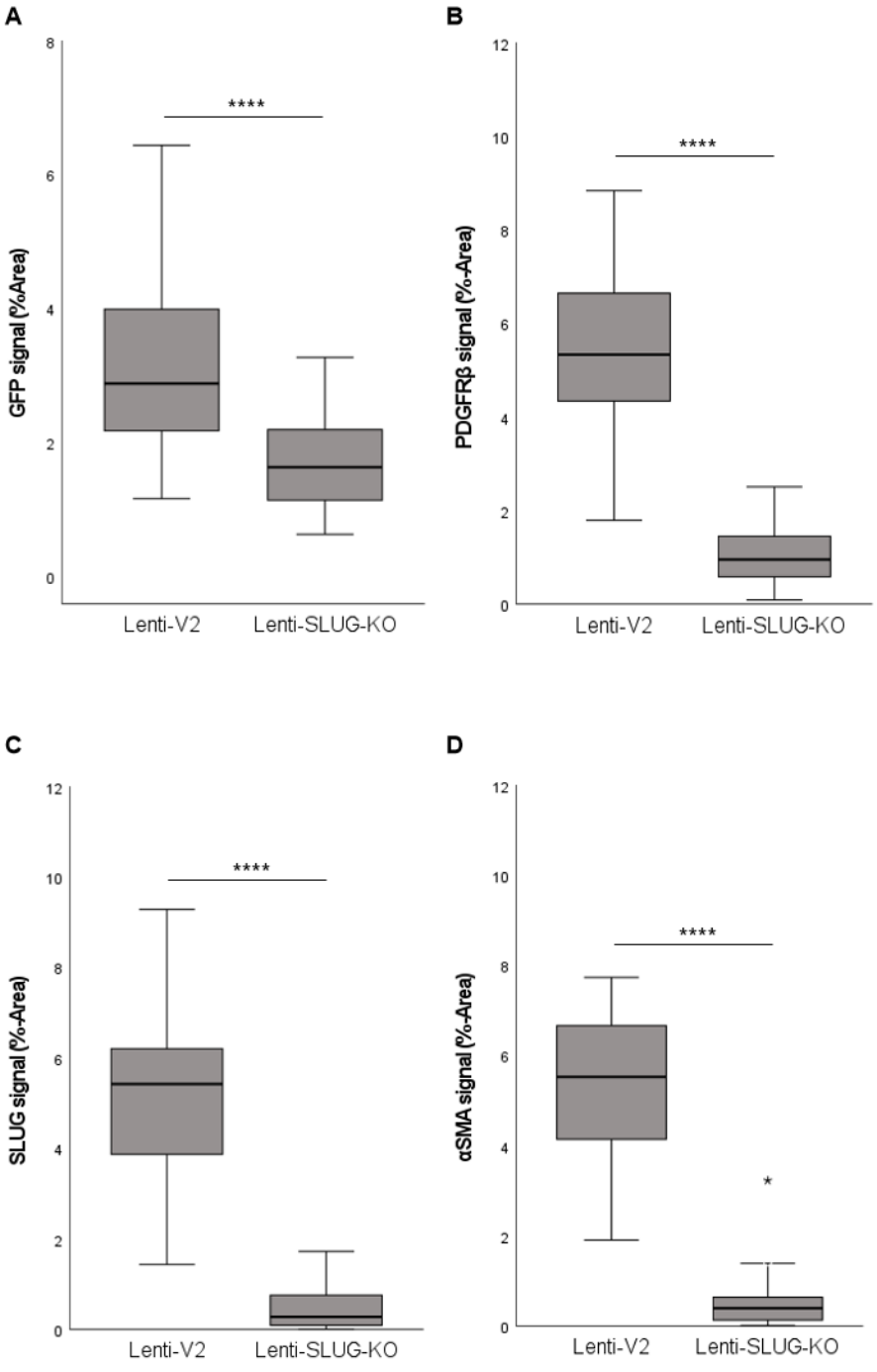

Figure 22: In the tumor area, the VAMC specific knockout of SLUG significantly reduces the number of VAMCs as well as the amount of PDGFR and αSMA in RGS5 strain mice bearing PAR tumors. *Quantification of GFP⁺ VAMCs (A), PDGFRβ (B) and αSMA (C) fluorescence. The knockout of SLUG in VAMCs was verified by analyzing SLUG (D) fluorescence (n=2 mice per group; in total n=48 (GFP and PDGFRβ) and n=24 (αSMA and SLUG) images were analyzed; unpaired t-test; mean ± SEM; **** p < 0.0001) (data shown in Merk et al., 2024).*

To examine whether the number of activated VAMCs in the tumor area was altered by knocking out SLUG in GBM-adjacent VAMCs, GFP⁺ VAMCs positive for either PDGFRβ and αSMA or PDGFRβ and SLUG were identified and were manually counted. Compared to Lenti-V2 injected mice, the number of either GFP-SLUG-PDGFRβ or GFP-αSMA-PDGFRβ triple positive cells was significant reduced, suggesting a prevention of the TGF-β-mediated VAMC activation by knocking out SLUG in these cells (Figure 23, Figure 24).

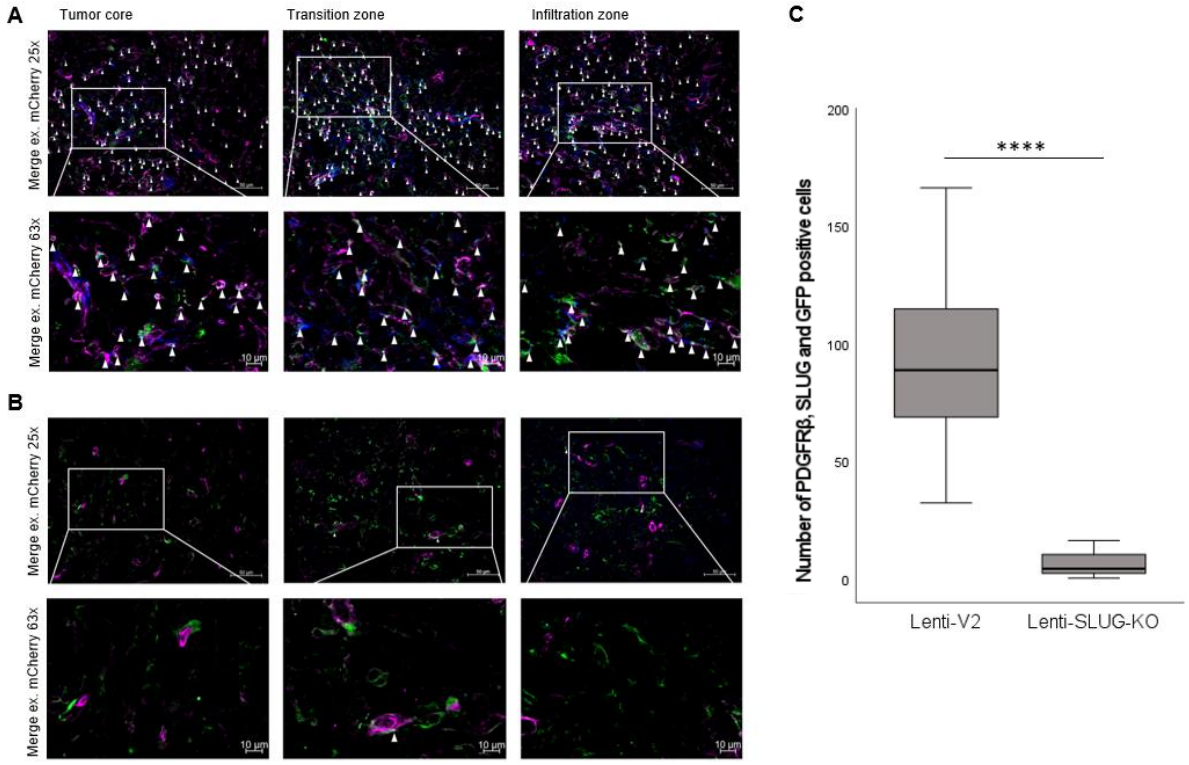

Figure 23: Visualization of PDGFRβ (magenta), SLUG (blue) and GFP (green) triple positive VAMCs*. PDGFRβ, SLUG and GFP triple positive VAMCs (marked with arrows) are shown in RGS5 strain mice bearing PAR tumors and that received an intrastriatal injection of either Lenti-V2 (A) or Lenti-SLUG-KO (B). Upper panel show pictures at 25x, lower panel at 63x magnification (n=2, photographs of one animal per group are exemplarily shown; scale bars 50 µm or 10 µm). C. Quantification of PDGFRβ, SLUG and GFP triple-positive VAMCs reveals a significant reduction in Lenti-SLUG-KO compared to Lenti-V2 injected mice (n=2 animals per group; n=24 images each group were analyzed; unpaired t-test; means ± SEM; **** p < 0.0001) (shown in Merk et al., 2024).*

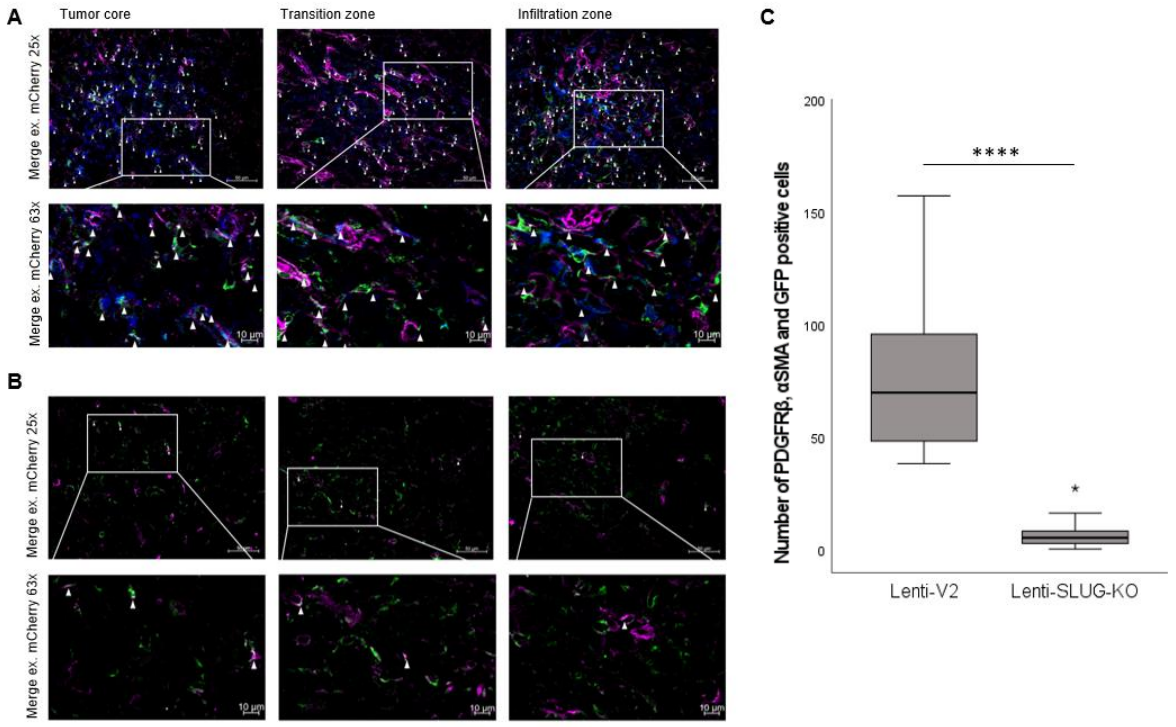

Figure 24: Visualization of PDGFRβ (magenta), αSMA (blue) and GFP (green) triple positive VAMCs*. PDGFRβ, αSMA and GFP triple positive VAMCs (marked with arrows) are shown in RGS5 strain mice bearing PAR tumors and that received an intrastriatal injection of either Lenti-V2 (A) or Lenti-SLUG-KO (B). Upper panel show pictures at 25x, lower panel at 63x magnification (n=2, photographs of one animal per group are exemplarily shown; scale bars 50 µm or 10 µm). C. Quantification of PDGFRβ, αSMA and GFP triple-positive VAMCs reveals a significant reduction in Lenti-SLUG-KO compared to Lenti-V2 injected mice (n=2 animals per group; n=24 images each group were analyzed; unpaired t-test; means ± SEM; **** p < 0.0001) (shown in Merk et al., 2024).*

These results have recently been published in Merk et al., 2024.

3.8 The VAMC-specific knockout of SLUG impairs the vessel density in the tumor area

Besides the impact of SLUG as an inducer of a mesenchymal phenotype in VAMCs, it was investigated whether the prevention of SLUG expression in VAMCs results in the development of vessels in the tumor area that show a more normal structure, compared to the altered and chaotic vessel structure regularly seen in GBM. Like before, IF staining for CD31 was used to determine vessel density.

Compared to Lenti-V2-injected animals, vessel density was clearly diminished in Lenti-SLUG-KO treated mice (Figure 25).

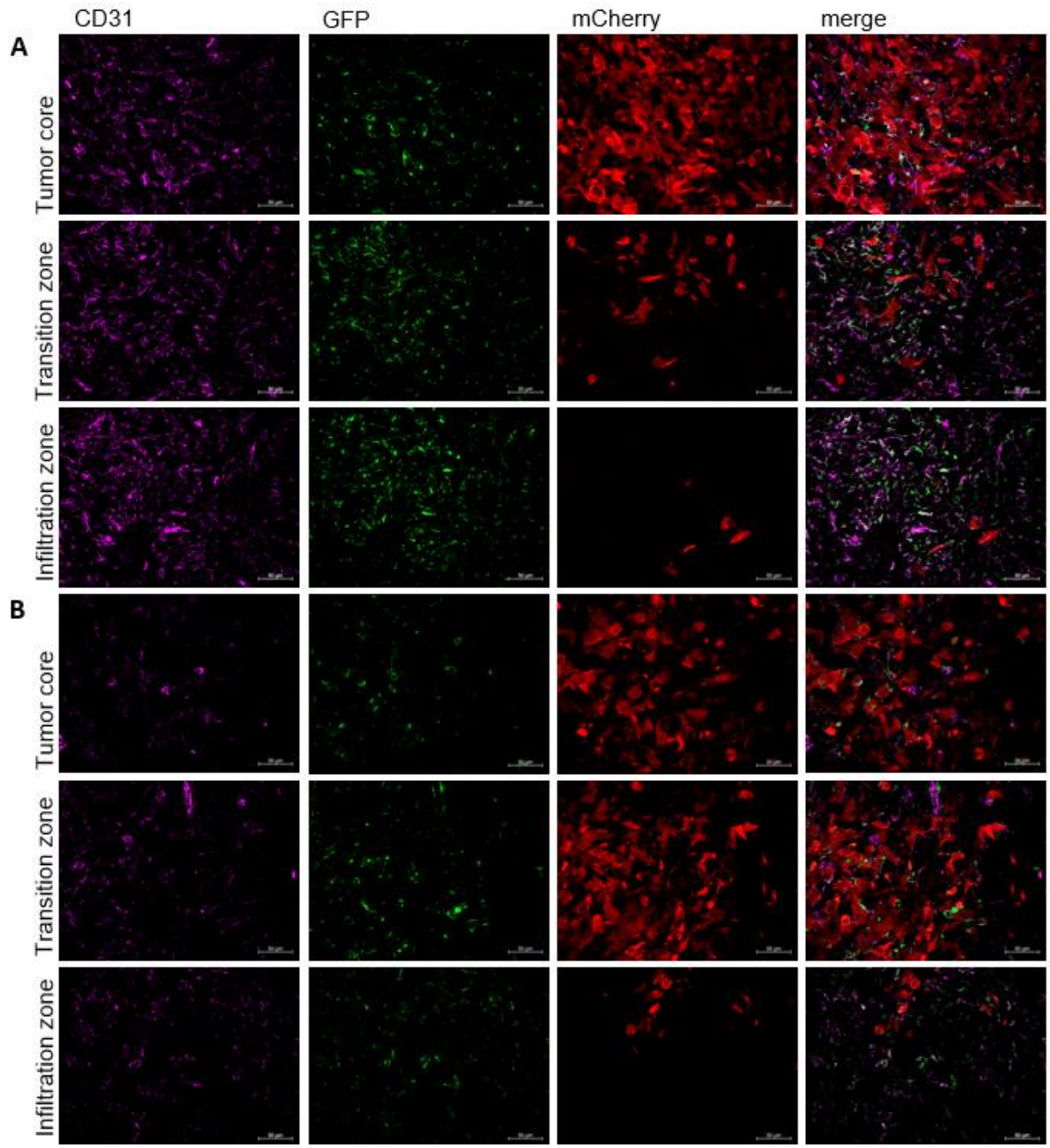

***Figure 25: Identification of CD31⁺ endothelial cells in the tumor area**. Photographs exemplarily show GFP, CD31 and mCherry fluorescence in representative areas for tumor core, transition and infiltration zone in RGS5 strain mice bearing PAR GBMs. Mice received either Lenti-V2 (A) or Lenti-SLUG-KO (B) intrastriatal injections prior to tumor cell implantation. All images were taken at 25x magnification (n=2 mice per group; scale bars 50 µm) (partly shown in Merk et al., 2024).*

These findings were further supported by quantification of CD31 fluorescence within different tumor areas that revealed a significant decrease of vessel density in the Lenti-SLUG-KO injected animals. However, knocking out SLUG in VAMCs did not

restore the basal vessel density observed in contralateral brain hemisphere that contains no tumor (Figure 26).

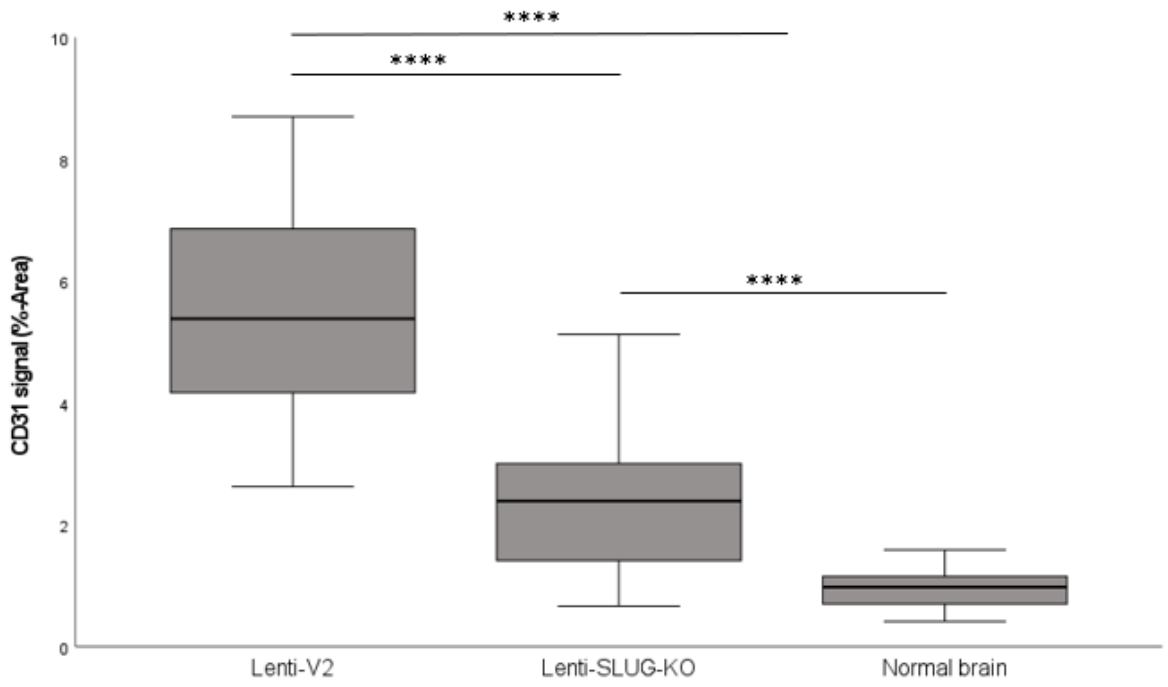

Figure 26: The knockout of SLUG in VAMCs significantly reduces the intratumoral vessel density. *RGS5 strain mice received an intrastriatal injection of either Lenti-V2 or Lenti-SLUG-KO prior to implantation of PAR cells at the same stereotactic brain coordinates. Quantification of CD31 immunofluorescence reveals a significant reduction of CD31 fluorescence in Lenti-SLUG-KO compared to Lenti-V2 treated animals. However, CD31 levels are still significantly higher in the tumor area compared to the no-tumor containing, contralateral hemisphere (n=2 mice per group, in total n=48 images per experimental group and n=24 images for the healthy hemisphere were analyzed; unpaired t-test; means ± SEM; **** p < 0.0001) (data shown in Merk et al., 2024).*

Additional IF analyses demonstrated that CD31 fluorescence strongly correlated with that of SLUG, αSMA in VAMCs as well as with the number of VAMCs in the tumor area (as shown by GFP; Supplementary Figure 8-11), indicating that vessel density is linked to these proteins and therefore to the activation of VAMCs.

Moreover, we were interested whether the decreased vessel density we observed in the Lenti-SLUG-KO injected mice was associated with lesser vascular abnormalities. Therefore, vessel structure and VAMCs coverage within the tumor region were analyzed. Lenti-V2 treated mice seemed to show a higher density of microvessels with a wider range of vessel diameter that were chaotically organized in glomeroid-

like structures. In comparison, Lenti-SLUG-KO injected mice also showed an elevated density of microvessel structures compared to that of the normal brain, however to a significantly lower extent than Lenti-V2 treated animals. Furthermore, vessel diameters seemed to be more homogeneous and vasculature structures showed less alterations after preventing the upregulation of SLUG in VAMCs, thereby resembling “more normal” vessel structures. Together, the tumor vasculature in Lenti-SLUG-KO injected mice displayed more structural similarities to “normal” vessels, even though it is still differed from the strictly organized, straight vessel course that can be seen in healthy brain parenchyma (Figure 27).

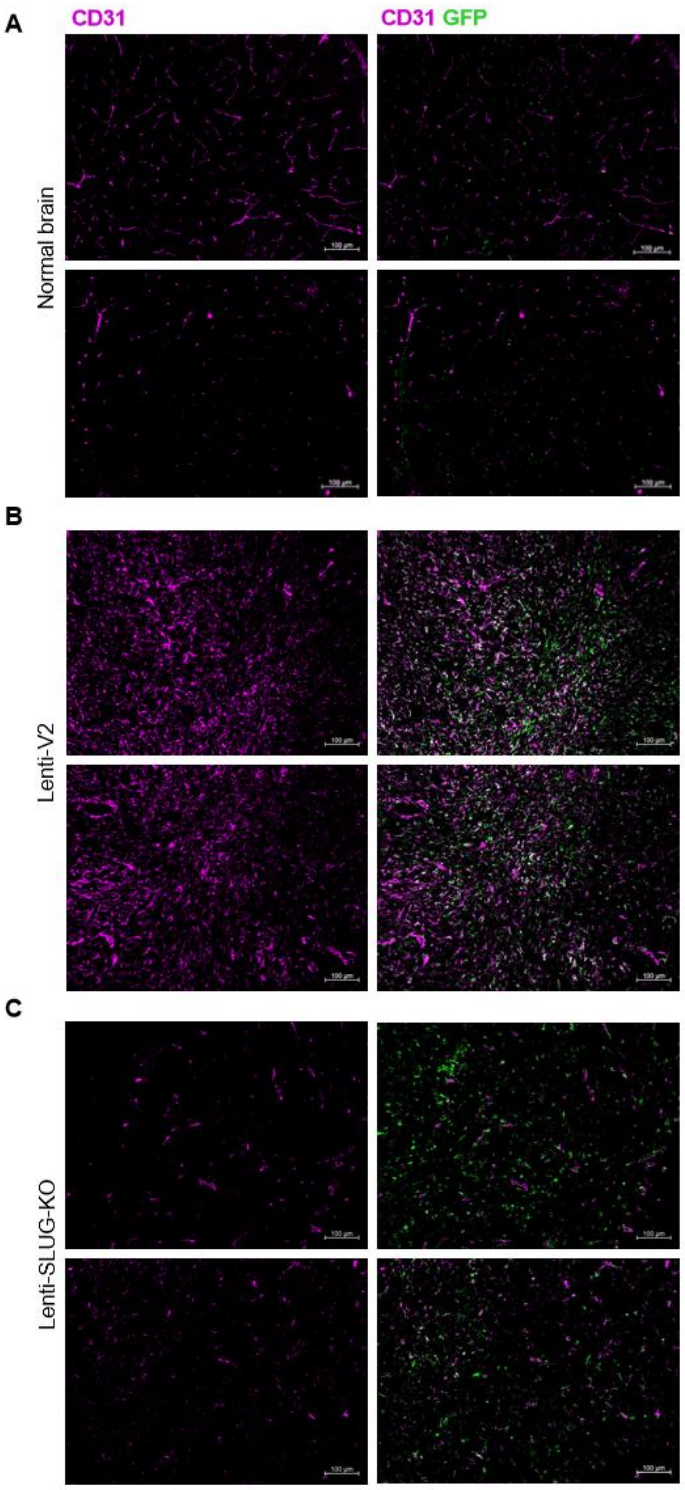

Figure 27: Vessel density in the healthy brain (A) and in the tumor area of RGS5 strain mice bearing PAR GBMs that received an intrastriatal injection of either Lenti-V2 (B) or Lenti-SLUG-KO (C). *Endothelial cells (CD31, magenta, left panels) and co-localization of CD31 with GFP⁺ cells (right panels) are exemplarily shown. Compared to Lenti-V2, mice injected with Lenti-SLUG-KO show a significant reduction of vessel density and of VAMC numbers. All images were taken at 10x magnification (n=2 mice per group; Scale bars: 100 µm) (partly shown in Merk et al., 2024).*

It is also noticeable, that not only vessel density but also the number of VAMCs covering the intratumoral blood vessels was significantly lower in the Lenti-SLUG-KO treated mice. In addition, when comparing the localization of the VAMCs, those in the Lenti-V2 injected animals appeared to be more loosely attached to the vasculature. These animals also presented a more heterogeneous vessel coverage with areas displaying VAMC-multilayers and with microvessels without VAMC-coverage. In contrast, in Lenti-SLUG-KO injected animals the VAMC-coverage appears more uniform. However, it is still augmented compared to vessels in the contralateral hemisphere (Figure 28). These results have recently been published in Merk et al., 2024.

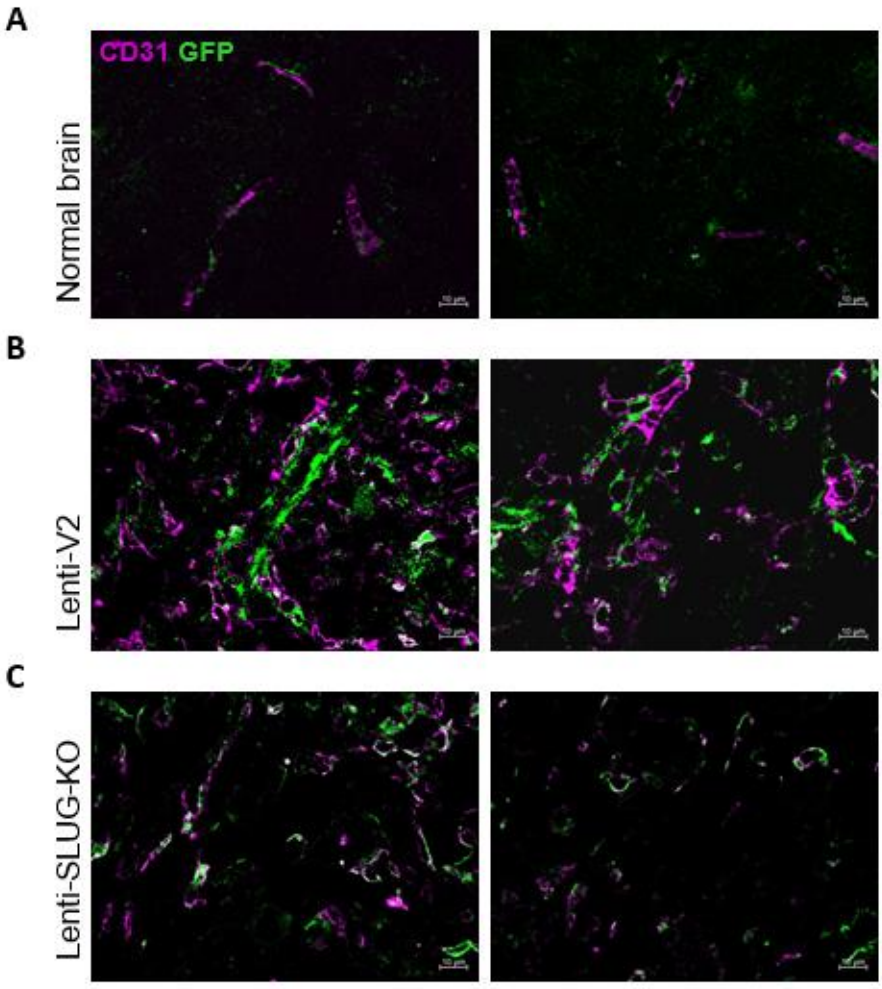

***Figure 28: Visualization of vessel structure and VAMC coverage**. The vascular structure consisting of endothelial cells (CD31) and adjacent VAMCs (GFP) is exemplarily shown in RGS5 strain mice harboring PAR tumors. Pictures show the no tumor containing contralateral hemisphere (A) as well as the tumor area of Lenti-V2 (B) and Lenti-SLUG-KO (C) injected animals. All images were taken at 63x magnification (n=2 mice per group; Scale bars: 10 µm) (partly shown in Merk et al. 2024).*

3.9 Knocking out SLUG in VAMCs provides a more prominent effect on vessel density than knocking out TGF-β in GBM cells

As shown before, both the VAMC-specific knockout of SLUG as well as the knockout of TGF-β in GBM cells display a significant decrease in intratumoral vessel density in the tumor area, however not reaching the normal vessel density of the healthy brain. Comparing the vascular density and structure in TGF-β-KO tumors with that of PAR tumors in mice that received Lenti-SLUG-KO, we observed a more consistently reduced amount of microvessels in the Lenti-SLUG-KO mice (Figure 29).

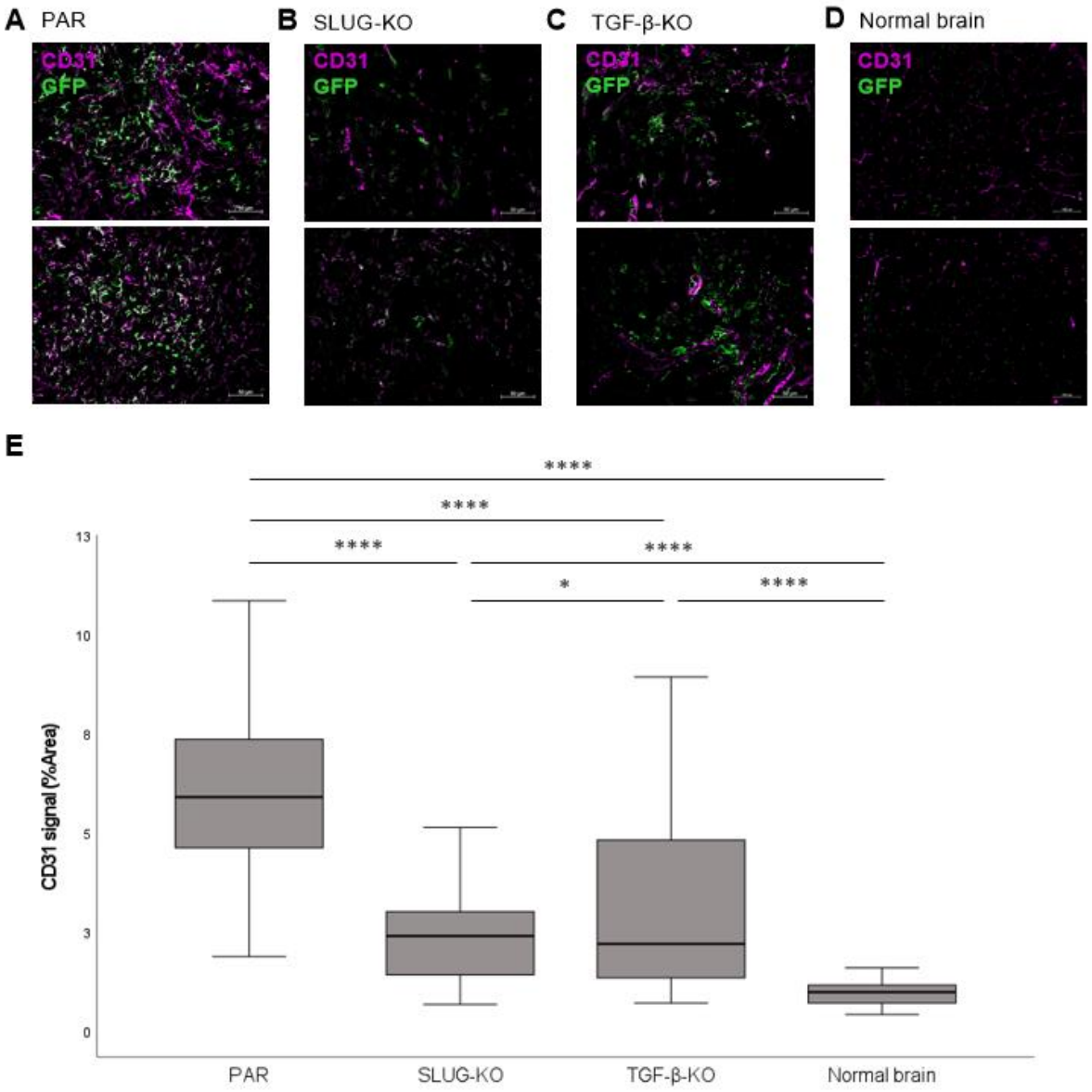

Figure 29: Visualization of vessel density after knocking out TGF-β in GBM cells or SLUG in VAMCs*. Quantification of CD31 fluorescence in PAR GBM without further treatment (PAR), in PAR tumors of mice that received an intrastriatal injection of Lenti-SLUG-KO (SLUG-KO), in mice harboring TGF-β-KO GBMs (TGF-β-KO) as well as in the contralateral hemisphere (normal brain). Highest reduction in vessel density was observed in those mice in which SLUG was specifically knocked out in VAMCs in the tumor area (25 x magnification; scale bars: 50 µm; n= 2 (SLUG KO) or n=3 (TGF-β-KO, PAR) mice per group; in total n=72 (TGF-β-KO, PAR), n=48 (Lenti-SLUG-KO) and n=24 (healthy hemisphere) images were analyzed; unpaired t-test, means ± SEM; * p < 0,05; **** p < 0.0001).*

Along with the reduction of vessel density within the tumor region, VAMC density was also lower both in the Lenti-SLUG-KO injected animals as well as in those mice that harbor TGF-β-KO GBMs. Though, the VAMC-specific knockout of SLUG

resulted in a statistically significant higher reduction of VAMCs in the tumor area than the knockout of TGF-β-KO GBM cells (Figure 30).

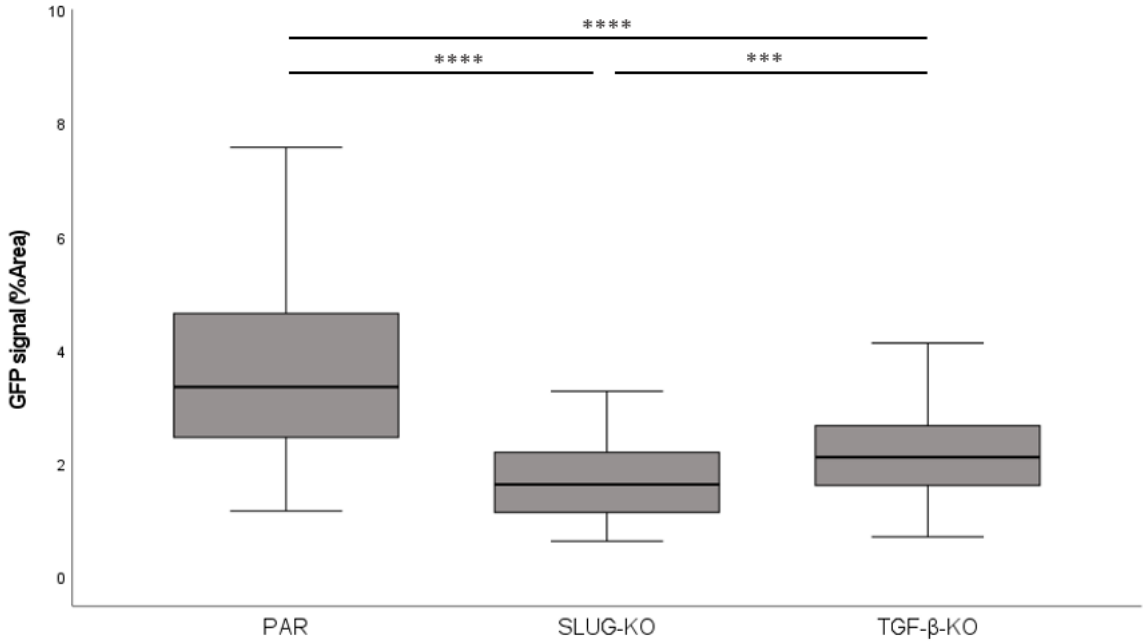

Figure 30: Pericyte density is significantly more reduced by the VAMC specific knockout of SLUG than by the GBM specific knockout of TGF-β. *Quantification of GFP fluorescence (%Area GFP⁺ cells) in the tumor area of mice harboring PAR GBMs (PAR), in mice that harbor PAR tumor and received Lenti-SLUG-KO (SLUG-KO) and in mice harboring TGF-β-KO GBMs (TGF-β-KO). Unpaired t-test was performed for statistical analysis (n=3 mice (TGF-β-KO, PAR) or 2 mice (Lenti-SLUG-KO); in total n=72 (TGF-β-KO, PAR) and n=48 (Lenti-SLUG-KO) images were analyzed, mean ± SEM; *** p < 0,001; **** p < 0.0001).*

This observation is in concordance with the significantly lower levels of PDGFRβ (**** <0,0001), αSMA (**** <0,0001) and SLUG (**** <0,0001) we detected in animals in which the upregulation of SLUG in VAMCs was prevented by the injection of Lenti-SLUG-KO prior to GBM cell implantation, compared to those mice that harbor TGF-β-KO GBMs.

3.10 Diminishing TGF-β-signaling impairs tumor vascularization

To further evaluate whether the TGF-β-mediated modulation of VAMCs is associated with vascular alterations in GBM-associated vessels, vascular density and structure were additionally analyzed in their three-dimensional (3D)

arrangement. Reconstructing 3D information by assembling a series of serial thin sections is often unsatisfying due to loss or distortion of individual sections (Richardson & Lichtman, 2015). Hence, we used CLARITY, a tissue clearing method which enables the integration of molecular and structural information on whole tissue samples (Du et al., 2018). In order to display the intratumoral vessel structure, we performed IF staining for endothelial cells (CD31) and the mCherry^{+} GBM cells in cleared mice brains bearing either PAR or TGF-β-KO GBM, or we, prior to implantation of PAR GBM cells, specifically knocked out SLUG in VAMCs adjacent the tumors. CLARITY and following microscopy analyses were performed in cooperation with Ulrich Mattheus and Dr. Andreas Mack (Anatomical Institute, Tübingen).

We observed that both, the prohibition of TGF-β secretion by GBM cells after knocking out TGF-β-KO in these cells as well as blocking the induction of SLUG-mediated EMT processes in VAMCs (by injecting Lenti-SLUG-KO prior to implantation of PAR GBM cells) resulted in a significant decrease in intratumoral vascular density compared with untreated mice harboring PAR GBM (Figure 31A).

These results were in accordance with our previous findings, which demonstrated that the amount of intratumoral vessels correlates with the number of “activated state VAMCs” in the tumor area. Unfortunately, staining quality and therefore signal brightness in the CLARITY samples was inconsistent. To improve the 3D visualization of the intratumoral vessel structure, surface algorithms (Imaris software) were applied (Figure 31B).

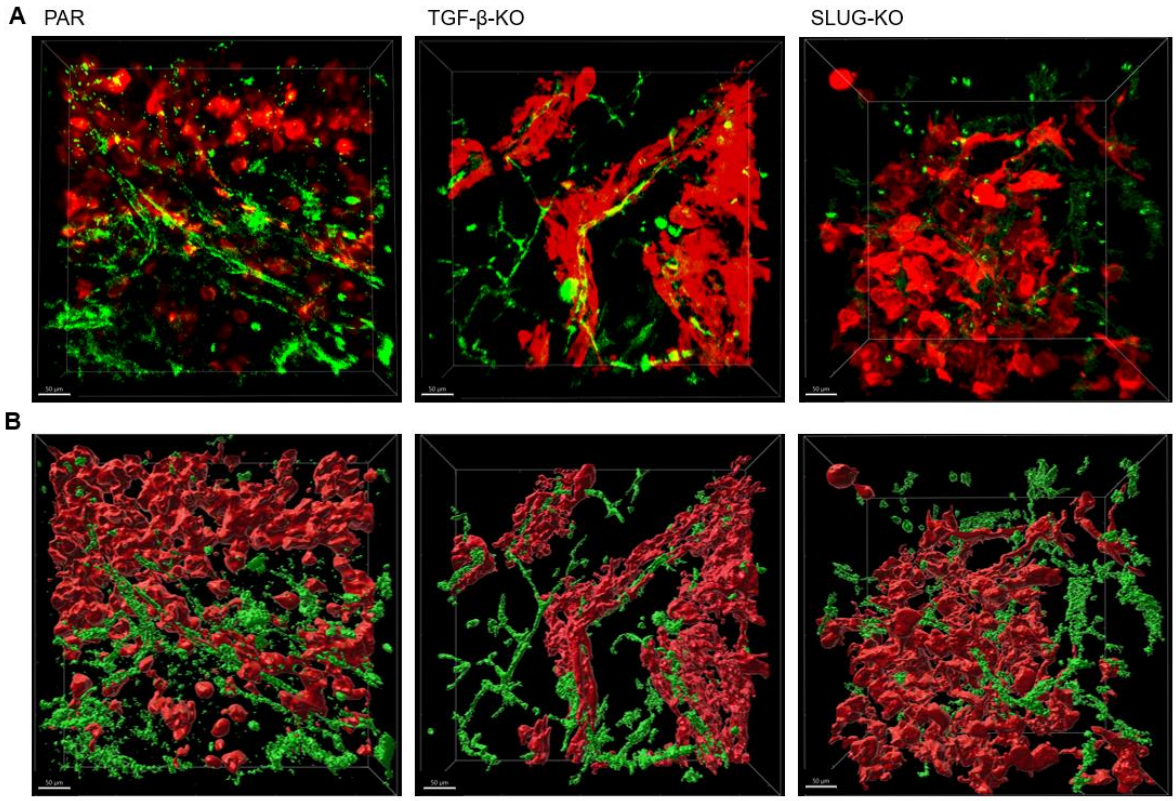

Figure 31: 3D Visualization of intratumoral vessel morphology after knocking out TGF-β in GBM cells or specifically knocking out SLUG in VAMCs*. Images exemplarily show CD31 (green) and mCherry fluorescence (GBM cells, red) in RGS5 strain mice bearing either PAR GBM without further treatment (PAR), PAR GBM after receiving an intrastriatal injection of Lenti-SLUG-KO (SLUG-KO) or TGF-β-KO GBM (TGF-β-KO) prior (A) and post (B) 3D-reconstruction by using Imaris. All images were taken at 20x magnification (n=1 mouse per group; Scale bars 50 µm) (shown in Merk et al., 2024).*

“Moreover, we were interested whether the decreased vessel density we observed after knocking out TGF-β in tumor cells or SLUG in VAMCs was associated with a reduced amount of vascular malformations. The 3D vessel reconstruction strikingly showed that vessels of PAR cell derived GBMs clearly displayed abundant structural alterations consisting of vascular tangles or glomeroid-like structures. They exhibited a more interconnected, "net-like" appearance and were positioned in closer proximity to each other compared to the vessels found in TGF-β-KO tumors or when SLUG induction in VAMCs was inhibited by Lenti-SLUG-KO injection. Mice brains bearing PAR GBM showed not only a high vessel density but also several structural aberrations instead of the straight vessel course seen in the healthy brain. We observed that this altered and chaotic vessel structure was clearly attenuated after

TGF-β-KO in tumor cells or VAMC-specific SLUG-KO" (Figure 32; cited from Merk et al., 2024 in a modified way). Different angles on the intratumoral vessel structure are shown in Supplementary Figure 16. Noteworthy, in addition to the less abnormal vascular structure, tumor cells at the infiltrative margins, particularly in TGF-β-KO GBM, appeared to be closer attached to blood vessels (Figure 31).

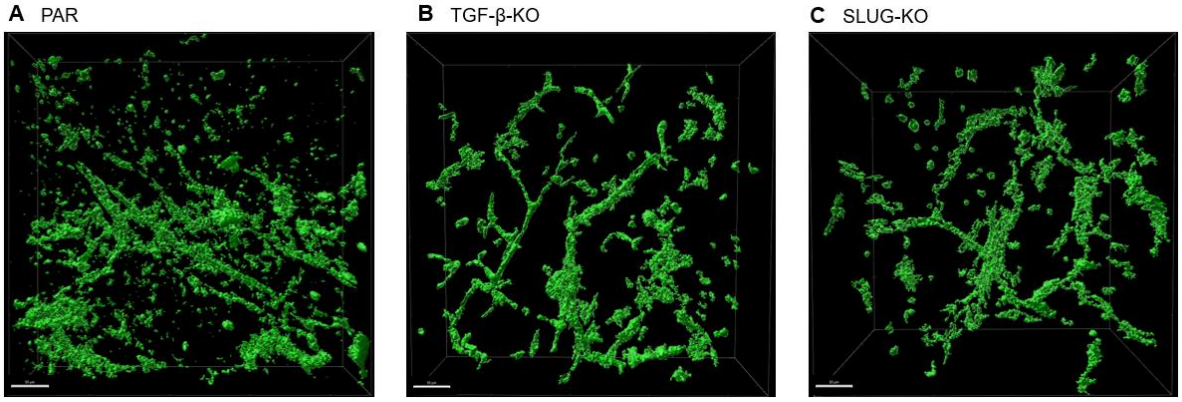

Figure 32: 3D Visualization of intratumoral vessel structure. *Images exemplarily show reconstructed CD31 signal (Imaris) in the tumor area of RGS5 strain mice bearing either PAR GBM without further treatment (PAR, A), PAR tumors after intrastriatal injection of Lenti-SLUG-KO (SLUG-KO, C) or TGF-β-KO GBMs (TGF-β-KO, B). All images were taken at 20x magnification (n=1 mouse per group; Scale bars 50 µm) (shown in Merk et al., 2024).*

To further evaluate the differences in vascular structure, we also compared the intratumoral vessel structure in the tumor area with those of the non-tumor containing contralateral hemisphere. The tumor vasculature of mice bearing either TGF-β-KO tumors or of mice where SLUG was knocked out in tumor adjacent VAMCs displayed more structural similarities to normal vessels. We observed a "more regular" vessel arrangement and branching when TGF-β-signaling was abolished compared to the glomeroid-like and chaotic vessel structure of PAR tumors. In addition, both the VAMC-specific SLUG-KO and TGF-β-KO in GBM cells resulted in tumor vessels with a more homogeneous diameter, thereby resembling the vascular structure seen in the non-tumor bearing hemisphere. However, the vessel diameter was still enlarged compared to vessels of the non-tumor containing brain parenchyma (Figure 33). These results have recently been published in Merk et al., 2024.

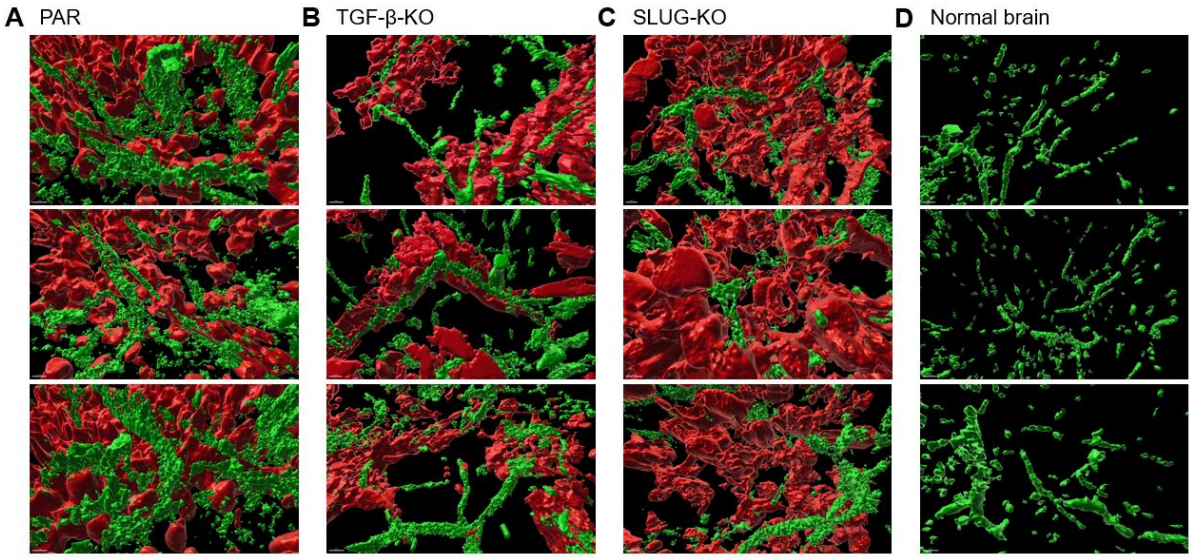

Figure 33: Visualization of the intratumoral vessel structure compared to that in the non-tumor containing hemisphere. *The vascular structure (CD31⁺ endothelial cells, green) is exemplarily shown for three different localizations within the tumor region (mCherry⁺ GBM cells, red) of RGS5 strain mice bearing either PAR GBM without further treatment (PAR; A), mice bearing PAR tumors after intrastriatal injection of Lenti-SLUG-KO (SLUG-KO; C) or mice bearing TGF-β-KO GBMs (TGF-β-KO; B). Under those conditions where TGF-β was knocked out in GBM cells or where SLUG was knocked out in VAMCs, a significant reduction of vessel density and vascular abnormalities was observed in the tumor area. However, both the TGF-β-KO as well as the SLUG-KO still display augmented vessel density compared to the non-tumor-bearing hemisphere (D). All images were enlarged from images taken at 10x magnification (n=1 mouse per group; Scale bars 20 µm).*

Knocking-out SLUG in VAMCs showed comparable results to the TGF-β-KO in GBM cells, which suggests that the TGF-β-mediated induction of SLUG and therefore the EMT-like program in VAMCs contributes to the abnormal vascularization in the tumor area. These findings are consistent with our results from IF analyses, which also demonstrated that vessel density and structure are associated with the TGF-β-mediated, SLUG-dependent modification of VAMC functions.

4 Discussion

Parts of the discussion have been recently published in my paper (Merk et al., 2024) and are presented in a modified form in the following chapters of the discussion.

GBM is a highly malignant tumor that is obligatory lethal. Despite best multimodal available therapy including optimal surgical resection, radiation and chemotherapy or even additional treatment strategies such as tumor treating fields, recurrence of the tumor is inevitable, hence GBM treatment remains only palliative. Thus, new therapy options are urgently needed. Given that GBM is a highly vascularized tumor characterized by altered vascular morphology and disorganized vessel arrangement, antiangiogenic therapies were considered as a promising therapeutic option. However, until now they lack to show remarkable increases in patient survival. Rather, vascular remodeling triggered by anti-VEGF therapy leads to hypoxia due to excessive tumor growth with simultaneous inadequate vascularization following an initial transient vascular “normalization”, which finally favors invasiveness (Keunen et al., 2011). After initial prolonged progression-free survival no benefit for OS was detected (Gilbert et al., 2014).

Hence, it has been shown, that not the neo-vascularization itself but the amount of unfunctional, irregular vessels is the determining factor for clinical outcome in patients with GBM (Birner et al., 2003). “For a long time, it has been thought that irregular vessel development in tumors depends on the activation of endothelial cells resulting in proliferation, migration and chaotic vascular structures. More recently, increased attention has been paid to vessel-covering pericytes and their interaction with endothelial cells during vessel formation processes in tumors, including GBM” (cited from Merk et al., 2024). Brain pericytes are known to be crucial for diverse microvascular functions, including angiogenesis, perfusion regulation and BBB-maintenance (Cheng et al., 2018). “However, within GBM, the tumor vasculature displays structural and functional abnormalities with increased and irregular pericyte coverage, that is associated with worse prognosis and accelerated tumor recurrence (Zhang et al., 2021)” (cited from Merk et al., 2024). Those glioma-associated VAMCs were found to strongly express EMT-transcription factors, among others SLUG,

especially in areas with high vascular proliferation. Along with their pronounced morphological alteration, this suggests that these non-neoplastic cells undergo an EMT-like activation process during glioma-associated neoangiogenic processes that is associated with vascular malformation (Wirsik et al., 2021). GMB-secreted TGF-β has already been shown to stimulate the development of a mesenchymal phenotype in VAMCs, characterized by the induction of SLUG and an enhanced αSMA and PDGFRβ expression, in *vitro* (Mäder et al., 2018).

“The aim of this study was to demonstrate if the modulation of VAMCs is conveyed via TGF-β-mediated induction of the EMT factor SLUG and whether this impacts the development of GBM-associated vascular abnormalities *in vivo.* The induction of this EMT-like activation was prevented by either knocking out TGF-β in the tumor cells or by knocking out SLUG in tumor adjacent, RGS5-expressing VAMCs.

One limitation of the used $RGS5^{GFP+}$ mouse model is that it does not allow a clear distinction between pericytes and vascular smooth muscle cells, as those cells could express RGS5 and might therefore also be positive for GFP (Bohannon et al., 2021).

Tumor angiogenesis is correlated to tumor size and growth. Hence, the growth rate of PAR and TGF-β-KO cells and tumors was initially determined to avoid artifacts generated by different sizes of PAR and TGF-β-KO GBMs. TGF-β-KO cells showed a reduced proliferation rate and decreased cell motility *in vitro* as well as a delayed tumor growth *in vivo*. By using MRI, the time point the tumors reached a size of 1.5 to 3 mm in diameter was determined prior to the experiments (demonstrated in Merk et al., 2024). However, this might be considered a limitation of this study because we cannot entirely exclude that a delayed tumor growth also impacts its vascularity, even if we analyzed the vascular structure of PAR and TGF-β-KO GBMs within a similar size range” (cited from Merk et al., 2024 in a modified way).

4.1 GBM-secreted TGF-β elevates the activity-status of VAMCs via SLUG-induction

“TGF-β, a prominent pro-tumorigenic cytokine secreted in large quantities by glioma cells, has been shown to be an important driver of EMT and additionally to be

involved in various tumor-associated processes such as invasion, immunosuppression, inflammation and angiogenesis (Dieterich et al., 2012). Hence, we experimentally determined whether glioma-secreted TGF-β modulates the expression of the EMT-transcription factor SLUG and therefore switches on EMT-like processes in VAMCs, by analyzing the association of SLUG with αSMA and PDGFRβ in VAMCs. Previous studies already reported a strong upregulation of αSMA and PDGFRβ in HBVPs in response to GBMs (Mäder et al., 2018). In accordance with those findings, strong signals of αSMA and PDGFRβ colocalization with GFP^+ VAMCs were detected in mice brains bearing PAR GBMs (Figure 12). Since αSMA and PDGFRβ are considered as pericyte activation markers, this suggests that in vascularized high-grade glioma VAMCs are pathologically activated. In parallel with the high levels of PDGFRβ and αSMA we observed in TGF-β-secreting, experimental GBMs, we detected SLUG. This suggests that not only *in vitro* (Wirsik et al., 2021), but also *in vivo,* SLUG is involved in the EMT-related activation process of VAMCs" (cited from Merk et al., 2024 in a modified way). Both TGF-β as well as EMT gene expression have been shown to correlate with the degree of tumor malignancy (Kahlert et al., 2013; Kjellman et al., 2000), posing the question if VAMC activation is crucial for GBM progression.

When the TGF-β mediated induction of EMT-like processes in VAMCs was prohibited by either knocking out TGF-β in GBM cells or inhibiting SLUG upregulation in VAMCs by knocking out SLUG in these cells via Lenti-SLUG-KO viruses, significantly lower numbers of activated VAMCs were detected in the tumor area (Figure 13, Figure 22, Figure 24). In line with the reduction of PDGFRβ and αSMA positive VAMCs, SLUG was barely detectable in VAMCs located in the area of TGF-β-KO GBMs, and was completely absent in SLUG-KO pericytes.

The specificity of the lentivirus-mediated KO of SLUG in VAMCs and subsequent reduction of cell activation was proven by using a non-target-control virus (Lenti-V2). Lenti-V2 lacked to show similar effects as observed for Lenti-SLUG-KO and resembles the VAMC marker profile of PAR GBMs (Figure 21). Thus, it can be assumed that SLUG upregulation is related to the induction of PDGFRβ and αSMA in VAMCs.

“To avoid artifacts that might be induced by knocking out SLUG in other cell types than VAMCs within the tumor area, we examined the expression of SLUG in the tumor area of PAR GBMs and found it to be colocalized invariably with GFP, but not with the tumor cells (Figure 8). However, even if CAS9 expression in Lenti-SLUG-KO was driven by the RGS5 minimal promoter, which significantly induced luciferase activity in MBVPs, but not in GL261 GBM cells we cannot completely exclude that minimal SLUG levels (below the immunofluorescence detection limit) in other cell types will be also reduced by intrastriatally applied Lenti-SLUG-KO“ (cited from Merk et al., 2024).

In vitro, the prevention of TGF-β-mediated EMT-induction in human brain vascular pericytes (HBVP) mitigated proliferation and cell motility and restores their original morphology (Wirsik et al., 2021). This reinforces the assumption that also *in vivo* the induction of a mesenchymal phenotype in pericytes located adjacent to TGF-β secreting high grade gliomas is at least partly mediated by the TGF-β-dependent induction of SLUG.

Interestingly, less PDGFRβ and αSMA positive VAMCs were observed in the tumor area of those mice in which SLUG was knocked out in VAMCs, compared to those mice that harbor TGF-β-KO GBMs (Figure 30). A possible explanation for this effect might be that there are other stimulators in addition to GBM-released TGF-β that serve as inducers for a mesenchymal phenotype in VAMCs. Apart from GBM cells, several other cell types in the CNS have been shown to secrete TGF-β, including endothelial cells and microglial cells, which could also stimulate VAMCs to a certain amount (Joseph et al., 2013; Rustenhoven et al., 2016). Nevertheless, additional influence on VAMC stimulation that is mediated by different cytokines cannot be excluded. Particularly the hypoxic microenvironment in GBM is known to be a potent inducer of EMT and morphological alterations (Iwadate, 2016; Krueger & Bechmann, 2010). Until now it remains unclear whether VEGF-signaling also directly influence VAMCs. It is known that VEGF primarily signals via VEGFR2, leading to endothelial cell proliferation, survival and migration (Peach et al., 2018). However, a VEGF-mediated activation of VEGFR1 has recently been shown to be not only involved in the recruitment of mural cells which is required for maturation and stabilization of

neo-vessels, but also to affect vascular permeability (Cicatiello et al., 2015; Uemura et al., 2021). As pericytes are known to express VEGFR1 particularly under hypoxic conditions (Cicatiello et al., 2015; Eilken et al., 2017), VEGF-mediated changes of pericytes towards a more mesenchymal phenotype enabling their recruitment might be considered. The former paragraph is cited in a modified form from my publication (Merk et al., 2024).

The orthotopic GL261^{mCherry} cells we implanted in RGS5-GFP reporter mice allowed us to track endogenous VAMCs. The source of VAMCs on or adjacent to GBM vessels remains controversial as it has been postulated that pericytes might also derive from glioma stem cells (Cheng et al., 2013) or might be attracted by the infiltration of progenitor cells (Birnbaum et al., 2011). Therefore, we cannot certainly examine the complete amount of VAMCs as only RGS5-positive, host-derived VAMCs express GFP. However, the group of Svensson has already shown that the majority of pericytes within the tumor area are endogenous, host-derived pericytes that were mainly activated or recruited (Svensson et al., 2015). Hence, the chosen model is appropriate to investigate the modulation of VAMCs by glioma cell secreted TGF-β *in vivo.*

4.2 In high grade gliomas, an elevated activity status of VAMCs is associated with vascular alterations

The aggressive growth of GBMs is associated with the overexpression of growth- and pro-angiogenic factors leading to rapid vascularization which then matches tumor growth (Siemann, 2011). Abnormal branching results in the development of disorganized and highly dysfunctional blood vessel networks with an uneven and poorly distributed vascular basement membrane, leaky endothelial cell layers and altered pericyte coverage leading to immature, tortuous, and hyperpermeable vessels (Armulik et al., 2011; Hoque et al., 2020).

“Vascularization not only involves endothelial cell proliferation, migration, branching and anastomosis, it also requires adequate pericyte coverage of vascular sprouts for vessel stabilization and maturation (Greenberg et al., 2008; Holderfield &

Hughes, 2008)" (cited from Merk et al., 2024). The tumor vasculature has already been shown to frequently exhibit structural and functional abnormality with irregular pericytes on endothelial tubes (Cheng et al., 2013). During tumor progression pericyte numbers increase drastically, whereas vascular endothelial cell numbers remain relatively stable, indicating that pericytes are the main cells that constitute the altered morphology of tumor microvessels (Hosono et al., 2017; Sun et al., 2014). Physiologically, pericytes constitute to a monolayer surrounding the endothelial cells (Berthiaume et al., 2018). However, the detected vessel coverage with VAMCs in the tumor area was heterogeneous and areas with multilayers of overlapping pericytes can be distinguished from vessels that display almost no VAMC coverage. These irregular VAMCs feature a significant correlation to elevated SLUG, PDGFRβ and αSMA levels. This further underpins that the shift towards a more mesenchymal phenotype in glioma-associated VAMCs and their subsequent activation might contribute to the development of vascular alterations in the tumor area. Unlike the tight association of pericytes and endothelial cells that can be observed in normal vessels (Morikawa et al., 2002), VAMCs with elevated PDGFRβ and αSMA levels display an abnormal separation to endothelial cells (Figure 17, Figure 28). The direct contact and communication between pericytes and endothelial cells are critical for maintenance of cerebrovascular stability and blood-brain barrier function (Berthiaume et al., 2018). Hence, the observed loose association of VAMCs to endothelial cells might result in vascular dysfunction and remodeling, as aberrations in VAMC-endothelial cell signaling are known to contribute to tumor angiogenesis (Schiffer et al., 2018). Our results demonstrate that, "at least in GL261 tumors, the knockout of TGF-β or the prevention of a SLUG-mediated EMT-like activation of VAMCs in the tumor environment, reduces the number of GFP^+ cells as well as that of $CD31^+$ cells, suggesting that not only ECs, but also VAMCs are main cells that constitute the multiplicity and altered morphology of tumor microvessels. The former paragraph has been discussed in detail also in my recent publication (Merk et al., 2024) and therefore has been cited here in a modified form.

“Apart from an abnormal VAMC coverage, tumor vessels displayed various structural abnormalities. The observed high amount of “activated-state” VAMCs in PAR GBMs was paralleled by an increased vascular density and vascular abnormalities which suggests an important role of activated VAMCs in glioma-associated neoangiogenic processes (Supplementary Figure 4). Tumor blood vessels displayed inconsistent diameter and uneven shape with abnormal bulges, blind ends and glomeroid-like structures” (cited from Merk et al., 2024). This abnormal vascular network is known to be unable to provide a sufficient and effective blood supply, thus resulting in hypoxia which in turn further promotes tumor neo-angiogenesis (Bergers & Song, 2005; Hardee & Zagzag, 2012). Interestingly, benign Grad 1 pilocytic astrocytomas also exhibit microvascular proliferations with glomeroid-like vessel proliferations. However, in contrast to vessels in high grade glioma, in pilocytic astrocytoma the relative position of endothelial cells and pericytes remains normal, which may reflect the intact regulation of angiogenesis in those low-grade gliomas (Mustafa et al., 2013). This indicates, that not vessel proliferations but their structural and functional abnormalities, especially the altered VAMC coverage, are one main factor that contributes to GBM malignancy. We were therefore interested, whether the prevention of the EMT-like, SLUG-mediated activation of VAMCs results in lesser vascular alterations.

Indeed, IF staining for CD31, a marker for endothelial cells, displayed a significant decrease in intratumoral vessel density in the tumor area of those mice that harbor TGF-β-KO GBMs as well as in mice where SLUG was specifically knocked out in VAMCs (Figure 29). The reduced vessel density thereby correlated with the above-mentioned decreased amount of PDGFRβ and αSMA positive VAMCs (Supplementary Figure 5, Supplementary Figure 9).

In addition, intratumoral vessels displayed more structural similarities to “normal” vessels when the TGF-β-mediated, SLUG-dependent activation of VAMCs was prevented. At this condition the amount disorganized and tortuous tumor vessels was significantly reduced, even though being still differed from the strictly organized, straight vessel course and density that is present in the tumor-free brain parenchyma of the contralateral hemisphere (Figure 32, Figure 33). Our results demonstrate that

the upregulation of SLUG and the elevated levels of PDGFRβ and αSMA in glioma-associated VAMCs strongly reflect the amount of neo-angiogenesis in the tumor area and that a pathological VAMC activation and dysfunction contribute to excessive and defective vascularization, which has already been shown to be associated with vascular leakage and hemorrhage (Dubrac et al., 2018).

However, in this regard it should be mentioned that other tumor-associated "vascularization" processes like the formation of blood-containing vessel-like networks by GBM cells that are devoid of endothelial cells, so called vasculogenic mimicry (Hardee & Zagzag, 2012), or trans-differentiation of tumor cells in pericytes or endothelial cells (Cheng et al., 2013) have not been examined in this study. Whether those mechanisms occur more frequently when TGF-β-mediated VAMC stimulation is inhibited has to be evaluated in further experiments.

In consistence with the amount of "normal" VAMCs, vascular density and structure that was more prominently restored in mice in which SLUG was knocked out in VAMCs compared to those mice that harbor TGF-β-KO gliomas, the amount of tumor-microvessels was also more consistently reduced after specifically knocking out SLUG. This suggests that elevated SLUG levels, induced by GBM-secreted TGF-β, modulate neo-vascularization by influencing VAMCs. Interestingly, particularly in TGF-β-KO tumors we observed a reduced, but highly variable and heterogeneous vessel density (Figure 15). This might be due to regional hypoxia that provides additional angiogenic stimuli and results in local increased neo-vascularization whereas other areas display normoxic conditions and therefore less vascularization.

The GBM vasculature characteristically displays areas of hyperpermeability as a direct consequence of its´ structural abnormalities, which is associated with vasogenic brain edema, a significant cause of morbidity in GBM patients (Batchelor et al., 2007; Jackson et al., 2017). Since diminished TGF-β-signaling in GBM results in "more normal" appearing vessel structures, it would be interesting whether this also associates with a functional reconstitution of blood flow, diffusion, BBB integrity, and a reduction of the edema.

4.3 Potential influences of the prevention of VAMC activation on the BBB

In GBMs, structural and functional abnormalities of peritumoral vessels are often associated with an inconsistent disrupted BBB that propose a main hurdle for targeting GBM as it limits adequate drug delivery (Oberoi et al., 2015). Pericytes, being important contributors to the establishment and maintenance of BBB integrity by regulating tight and adherens junctions as well as transcytosis across endothelial cells (Cheng et al., 2018; Liebner et al., 2018), can be functionally modified by GBM cells (Thanabalasundaram et al., 2011). Via the TGF-β-mediated induction of EMT-factors in VAMCs, GBM cells are able to induce proliferation and cell motility, and notably change the metabolic behavior of VAMCs. Schumacher et al. demonstrated that TGF-β treatment of HBVPs results in BBB disruption at least *in vitro*. Additional metabolomic and transcriptomic analyses underscored that the TGF-β-mediated functional and metabolic changes in pericytes are closely connected with their role during angiogenic processes (Schumacher et al., 2023). In combination with the lower VAMC activity state and the less chaotic vessel structure resembling normal vessels we observed after preventing the induction of pericytic SLUG expression *in vivo*, these findings suggest that the BBB integrity might also be affected. However, this has to be further evaluated for example by measuring the amount of edema or the uptake of contrast agents using small animal MRI. The former paragraph has been discussed in detail also in my recent publication (Merk et al., 2024) and therefore has been cited here in a slightly modified form.

4.4 Diminishing TGF-β-signaling impairs tumor invasiveness

Interestingly, in addition to the altered VAMC coverage in mice bearing TGF-β-KO GBMs, in these tumors we observed a more localized, clustered growth pattern and less tumor cell infiltration compared to PAR GBMs (Figure 10). TGF-β-secretion by GBM cells induces the expression, secretion and activation of matrix metalloproteinases (MMP)-2) and -9, whereas the expression of tissue inhibitor of metalloproteinase (TIMP) in the tumor area is downregulated. This results in a

remodeling of the extracellular matrix (ECM) thereby enhancing and facilitating tumor cell migration (Ikushima & Miyazono, 2010). However, it remains unclear to what extent the “vessel normalization” we observed in mice harboring TGF-β-KO GBMs might additionally contribute to the less invasive behavior of these tumors.

In contrast to TGF-β-KO GMBs, the VAMC-specific SLUG knockdown did not show an altered tumor cell invasion, indicating that VAMC independent processes predominate the promotion of tumor cell invasion. However, also TGF-β secreting PAR tumors in which SLUG was knocked out in VAMCs displayed a more heterogeneous growth pattern. Hence, we cannot exclude that the Lenti-SLUG-KO injection prior to tumor cell implantation influences tumor migration and infiltration in the surrounding tissue.

4.5 Possible effects of a “more normal” intratumoral vasculature on treatment response

Heterogeneity in vascular morphology within the tumor along with a partly intact remaining BBB particularly at the infiltration zone where highly migratory tumor cells invade the normal cortex proposes a major hurdle for therapy success (Kane, 2019). Various promising novel targeted therapies have been evaluated for treating GBM recurrence over the last decades, however until now they failed to show the significant clinical benefit (Alifieris & Trafalis, 2015). At least partly due to the inconsistent BBB disruption within the tumor area, treatment agents are unable to reach adequate intratumoral concentrations without dose-limiting systemic side-effects (Guerra et al., 2018). Several studies have shown that alterations in GBM-associated blood vessels, especially when they retain a high level of pericyte coverage, limit therapy responsiveness (Hoque et al., 2020). This supposes that the “more normal” vessel structure with reduced irregular VAMC coverage that we observed in the absence of TGF-β or after knocking out SLUG in VAMCs might also improve therapy effectiveness. The re-establishment of a “normalized” vessel structure can improve blood flow and oxygenation, as well as reduce vascular permeability and edema resulting in longer progression-free survival (Cohen et al.,

2009; Xiao et al., 2018). The resultant more regular perfusion might not only decrease intratumoral hypoxia and therefore tumor invasiveness, but also facilitate drug delivery into the tumor tissue (Ameratunga et al., 2018). Thus, vessel “normalization” instead of inhibition of tumor neo-angiogenesis has emerged as a potentially powerful concept to attenuate vascular dysfunction and improve chemotherapeutic or immunotherapy delivery and efficacy (Hoque et al., 2020).

5 Abstract

Glioblastoma (GBM) is the most common malignant primary brain tumor in adults. Despite various modern therapeutic strategies, GBM remains an incurable and highly lethal disease with a very poor prognosis. Among others, one of the defining pathological characteristics of GBM is its high angiogenesis ability and the resultant excessive and dysfunctional vascularization being a main contributor to the devastating prognosis of GBM patients. Recently, pericytes have been identified to mainly constitute the irregular vessel architecture in GBM. *In vitro* data suggest that TGF-β secreted by glioma cells stimulates the development of a mesenchymal phenotype in pericytes via an epithelial-to-mesenchymal transition (EMT)-like activation that results in pericyte proliferation, migration and morphological changes favoring the formation of GBMs´ chaotic vasculature. Thus, this study aimed to investigate if TGF-β modulates VAMC (vessel-associated mural cell) functions via the induction of the EMT factor SLUG and its potential influences on the development of vascular abnormalities associated with GBM *in vivo*.

Therefore, in a syngeneic mouse GBM model, we assessed the activation status of glioma-associated VAMCs by disrupting the TGF-β- and SLUG-mediated EMT-induction either by preventing TGF-β secretion from GBM cells or by specifically knocking out the EMT regulator SLUG in VAMCs before tumor cell implantation. The VAMC activation state was evaluated by measuring the levels of PDGFRβ and αSMA proteins. Stainings for the endothelial cell marker CD31 were performed to investigate the corresponding intratumoral vessel structure.

Blocking EMT-mediated activation of glioma-associated VAMCs significantly reduced the number of PDGFRβ- and αSMA-positive VAMCs, regardless of whether TGF-β secretion by GBM cells was inhibited or SLUG was specifically knocked out in VAMCs prior to tumor cell implantation. The decrease in $PDGFR^+$ or αSMA^+ VAMCs we observed under those circumstances corresponded with diminished vessel density and fewer vascular abnormalities and was even more pronounced after SLUG KO in VAMCs compared to mice that harbor TGF-β-KO GBM.

Our findings suggest that at least in experimental mouse GBMs the SLUG-mediated modulation of VAMC activity is induced by GBM-secreted TGF-β and that activated

VAMCs play a crucial role in neo-angiogenic processes within this tumor. We propose that dysregulated activation of VAMCs in the tumor microenvironment is responsible for the disorganized tumor vasculature.

There is emerging evidence that vessel normalization can mitigate tumor hypoxia, reduce tumor-associated edema, and enhance drug delivery. Thus, preventing the formation of unstructured and dysfunctional tumor vasculature during tumor recurrence holds promise as a therapeutic strategy for GBM and other highly angiogenic tumors. The involvement of VAMCs in tumor angiogenesis we demonstrated in this study potentially identifies these cells as new therapeutic targets. However, further research is required to evaluate whether pericytes are suitable as target structures for vascular-normalizing therapeutic approaches.

6 Deutsche Zusammenfassung

Das Glioblastom (GBM) ist der häufigste bösartige primäre Hirntumor bei Erwachsenen und hat trotz moderner Therapiestrategien eine sehr schlechte Prognose. Es zeichnet sich unter anderem durch eine sehr ausgeprägte, aber chaotische Vaskularisierung aus, die zu einer insuffizienter Blutversorgung des GBM führt. Kürzlich wurde festgestellt, dass nicht Endothelzellen, sondern vor allem Perizyten zur irregulären Gefäßstruktur im GBM beitragen. *In vitro* Daten deuten darauf hin, dass GBM-sezerniertes TGF-β epithelial-zu-mesenchymal Transition (EMT)-ähnliche Prozesse in humanen Hirnperizyten induziert, assoziiert mit gesteigerter Migration, Proliferation und veränderter Wachstumsmorphologie dieser Zellen.

Ziel dieser Studie war es zu evaluieren, ob TGF-β auch *in vivo,* via Induktion des EMT-Regulators SLUG, die Funktionen von Gefäß-assoziierten muralen Zellen moduliert und ob dies die Entwicklung Tumor-assoziierter Gefäßanomalien beeinflusst. In einem syngenen Maus-GBM-Modell wurde für diese Untersuchungen das Anschalten des EMT-Programms in VAMCs auf zwei unterschiedliche Weisen verhindert: Einerseits durch den Knockout von TGF-β in GBM-Zellen, welcher in der Abschaltung der Sekretion dieses Zytokins durch die Tumorzellen resultiert. Alternativ wurde SLUG spezifisch in VAMCs ausgeknockt, also die TGF-β-vermittelte Induktion des EMT-Programms in VAMCs blockiert. Der Aktivitätsstatus von VAMCs wurde mittels Immunfluoreszenz (IF)-Detektion der Aktivierungs-assoziierten Proteine *Platelet-Derived Growth Factor Receptor* (PDGFR)-β und *Alpha Smooth Muscle Actin* (αSMA) gezeigt. Die intratumorale Gefäßstruktur wurde mittels IF-Färbung für den Endothelzellmarker CD31 untersucht.

Die Anzahl aktivierter, PDGFRβ- oder αSMA-positiver VAMCs war signifikant reduziert, wenn die Induktion von SLUG und somit EMT-Prozesse in VAMCs unterbunden wurde. Die Effekte waren unabhängig davon, ob TGF-β in den GBM-Zellen oder SLUG in VAMCs ausgeknockt war. Die geringere Zahl an $PDGFR\beta^+$ oder $aSMA^+$ VAMCs im Tumorareal korrelierte mit einer geringeren Gefäßdichte und einer geringeren Anzahl abnormer Gefäße.

Die in dieser Arbeit erhobenen Daten belegen, dass die TGF-β vermittelte SLUG-Hochregulation in VAMCs und damit verbundene EMT-Prozesse auch *in vivo* maßgeblich an der Aktivierung von VAMCs und der Bildung unfunktionaler, chaotischer Gefäße im Tumorareal beteiligt sind. Erkenntnisse aus dieser Studie identifizieren Perizyten damit als mögliche zukünftige Zielstrukturen für gefäß-normalisierende Therapieansätze, dies bedarf jedoch weiterer Untersuchungen.

7 Supplement

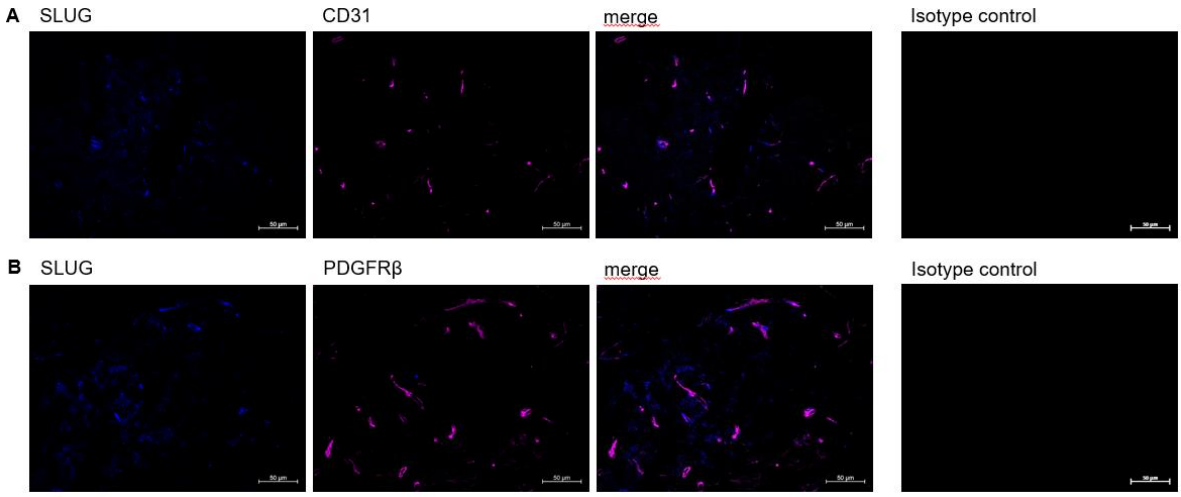

Supplementary Figure 1: Visualization of staining specificity for SLUG plus CD31 and SLUG plus PDGFRβ double staining. *Images show representative areas of SLUG and CD31 (A) or SLUG and PDGFRβ (B) double staining on brain stem tissue of a neonatal C57BL/6 mouse (kindly provided by Dr. Yuanyuan Liu, Research Department Neurology Epileptology, Hertie Institute for Clinical Brain Research). Staining specificity was proven by comparison with negative Isotype controls for either Goat anti-Rabbit Alexa Fluor™ 405, 1:1000, Invitrogen (A) or Goat anti-Rat Alexa Fluor™ 647, 1:1000, Invitrogen (B). Strong staining signals were detected when using antibodies targeting the proteins of interest whereas no signal was detected in the corresponding isotype controls. This indicates that the double stainings for SLUG and αSMA plus either CD31 or PDGFRβ are specific. Stainings were performed in collaboration with Katja Regel under my supervision. All images were taken with 25x magnification. Scale bars: 50 µm.*

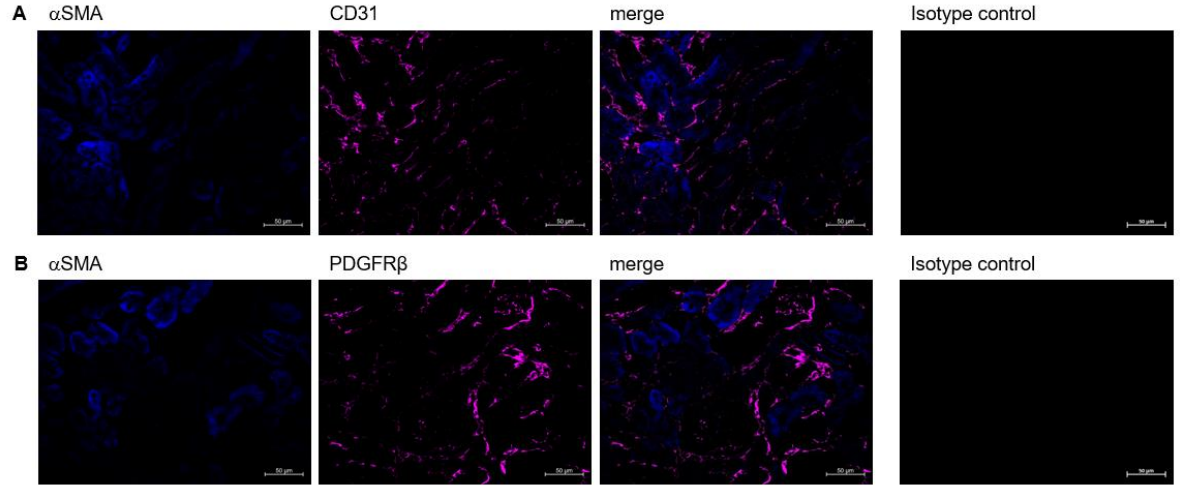

Supplementary Figure 2: Visualization of staining specificity for αSMA plus CD31 and αSMA plus PDGFRβ. *Pictures show representative areas of αSMA and CD31 (A) or αSMA and PDGFRβ (B) double staining on mouse kidney tissue of a RGS5 strain mouse, as kidney tissue is known to express those proteins. Staining specificity was proven by comparison with negative Isotype controls for either Goat anti-Rabbit Alexa Fluor™ 405, 1:1000, Invitrogen (A) or Goat anti-Rat Alexa Fluor™ 647, 1:1000, Invitrogen (B). Strong staining signals were detected when using antibodies targeting the proteins of interest whereas no signal was detected in the corresponding isotype controls. This indicates that the double stainings for αSMA plus either CD31 or PDGFRβ are specific. Stainings were performed in collaboration with Katja Regel under my supervision. All images were taken with 25x magnification. Scale bars: 50 µm.*

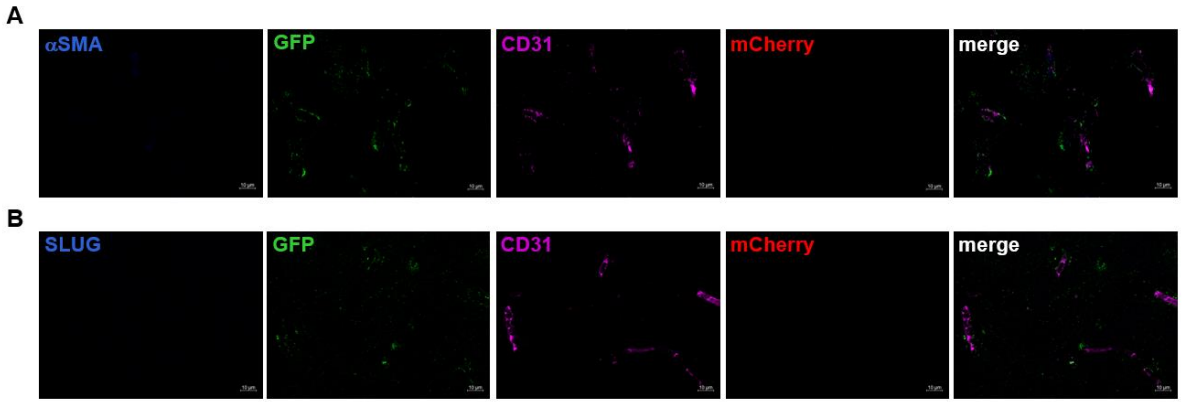

Supplementary Figure 3: Visualization of αSMA and SLUG absence in the non-tumor-bearing hemisphere. *Pictures exemplarily show αSMA (A) and SLUG (B) fluorescence in the non-tumor-bearing hemisphere of RGS5 strain mice. Neither αSMA nor SLUG signal was detectable in the absence of mCherry positive tumor cells. All images were taken in 63x magnification. Scale bars 10 µm.*

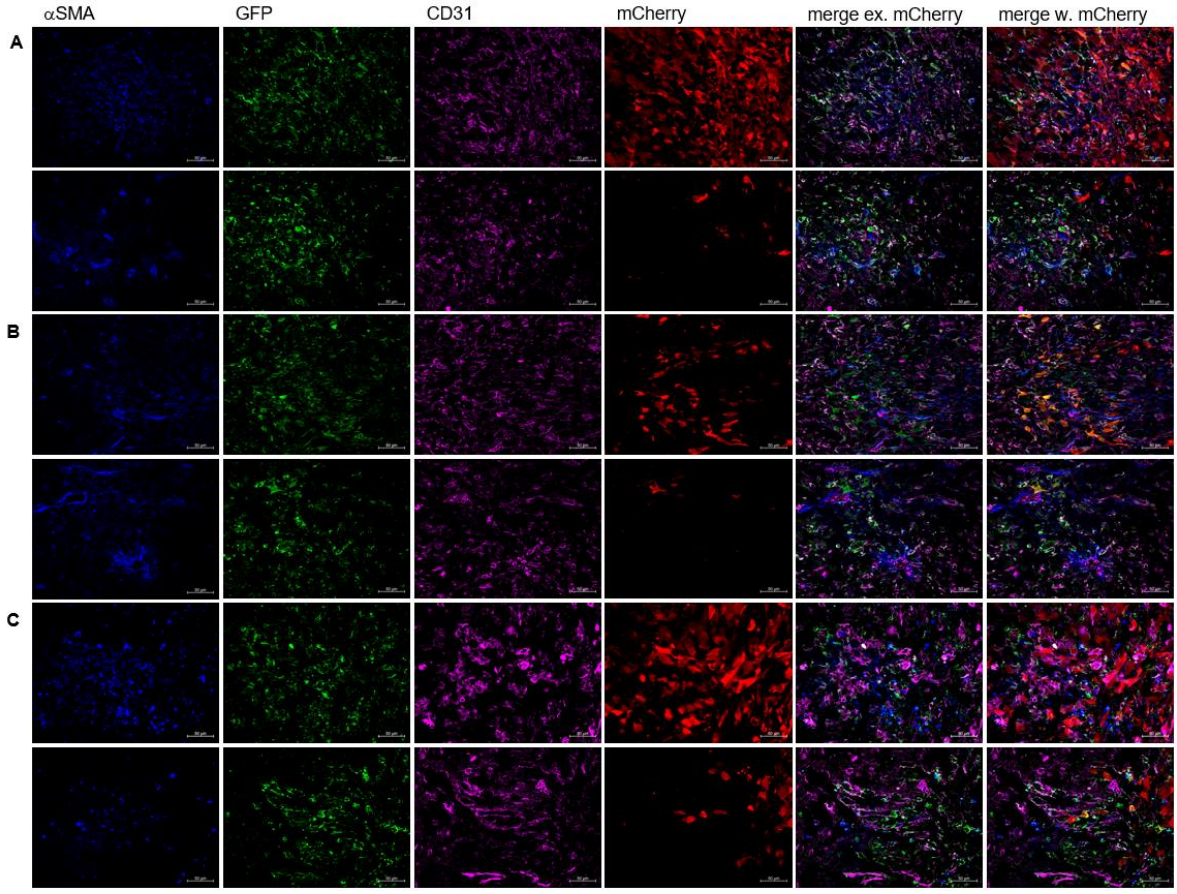

Supplementary Figure 4: Visualization of αSMA and GFP fluorescence adjacent to endothelial cells (CD31$^+$) in PAR GBM bearing RGS5 strain mice. *Images show αSMA, GFP and CD31 signals in representative areas for the tumor core and the infiltration zone for each of the three examined mice (A, B, C). Merge pictures show overlays of all staining including the tumor (merge w. mCherry) or excluding GBM cells (merge ex. mCherry). All images were taken with 25x magnification (n=3 mice; Scale bars: 50 µm).*

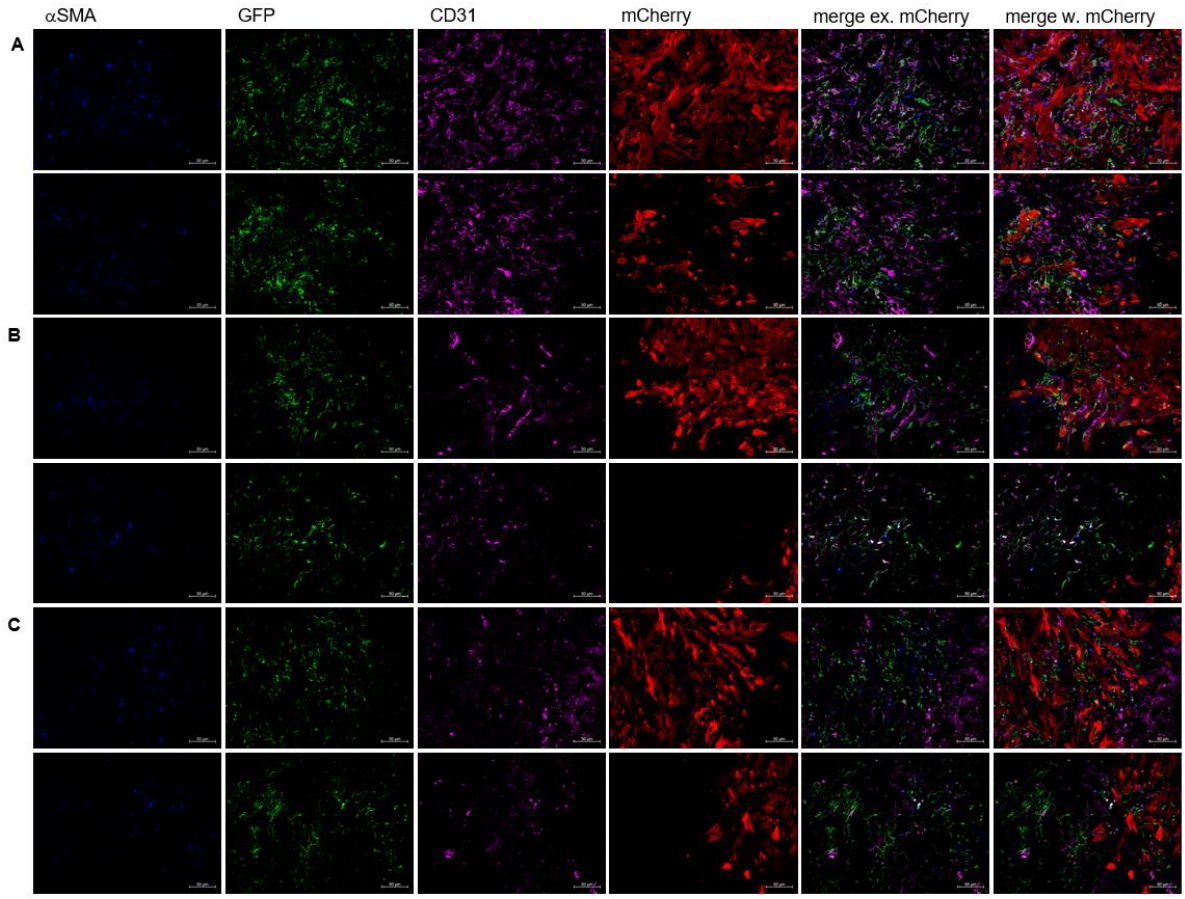

Supplementary Figure 5: Visualization of αSMA and GFP fluorescence adjacent to CD31⁺ endothelial cells in RGS5 strain mice bearing TGF-β-KO GBM. *Images show αSMA, GFP and CD31 signals in representative areas for the tumor core and the infiltration zone for each of the three examined mice (A, B, C). Merge pictures show overlays of all staining including the tumor (merge w. mCherry) or excluding GBM cells (merge ex. mCherry). All images were taken with 25x magnification (n=3 mice; Scale bars: 50 µm) (partly shown in Merk et al., 2024).*

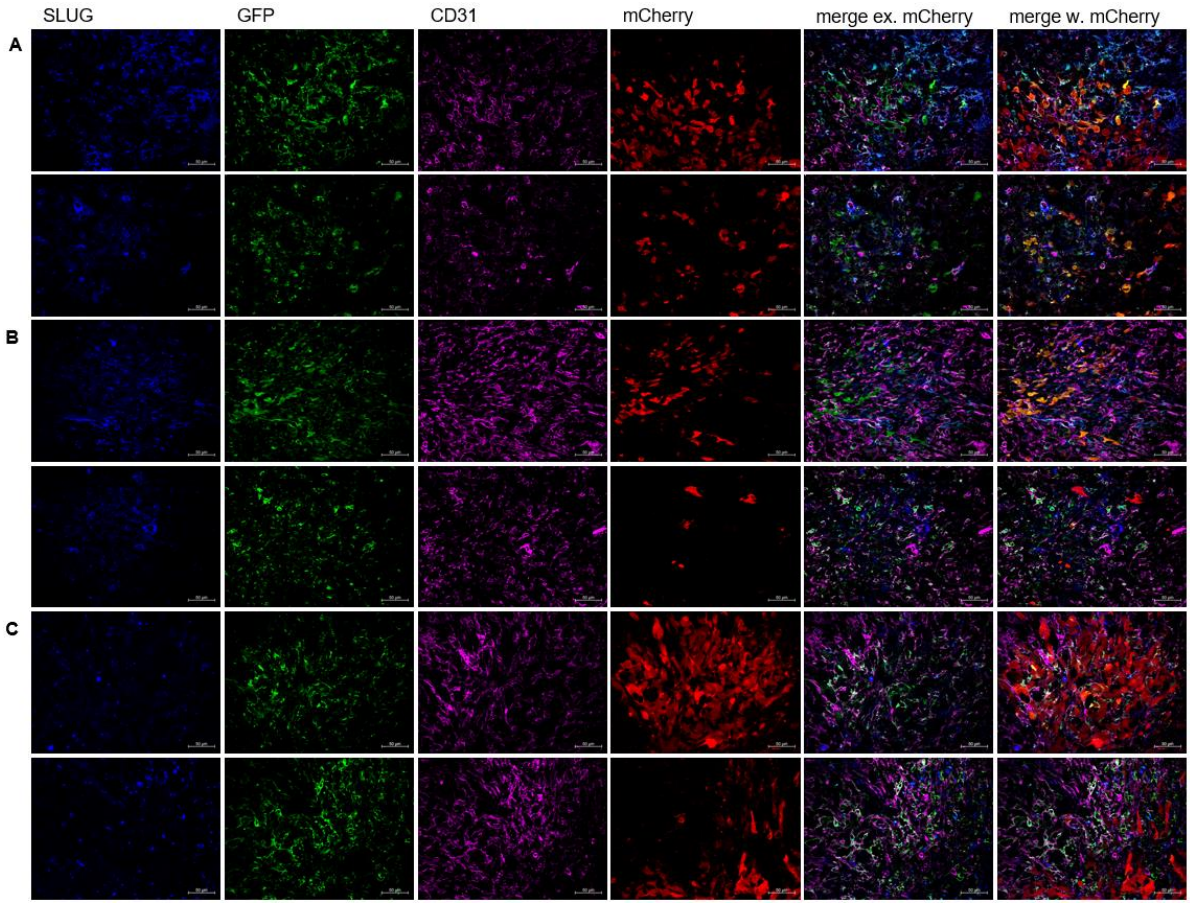

Supplementary Figure 6: Visualization of SLUG and GFP fluorescence adjacent to CD31⁺ endothelial cells in PAR GBM bearing RGS5 strain mice. *Images show SLUG, GFP and CD31 signals in representative areas for the tumor core and the infiltration zone for each mouse of the experimental group (A, B, C). Merge pictures show overlays of all staining including the tumor (merge w. mCherry) or excluding GBM cells (merge ex. mCherry). All images were taken with 25x magnification (n=3 mice; Scale bars: 50 µm).*

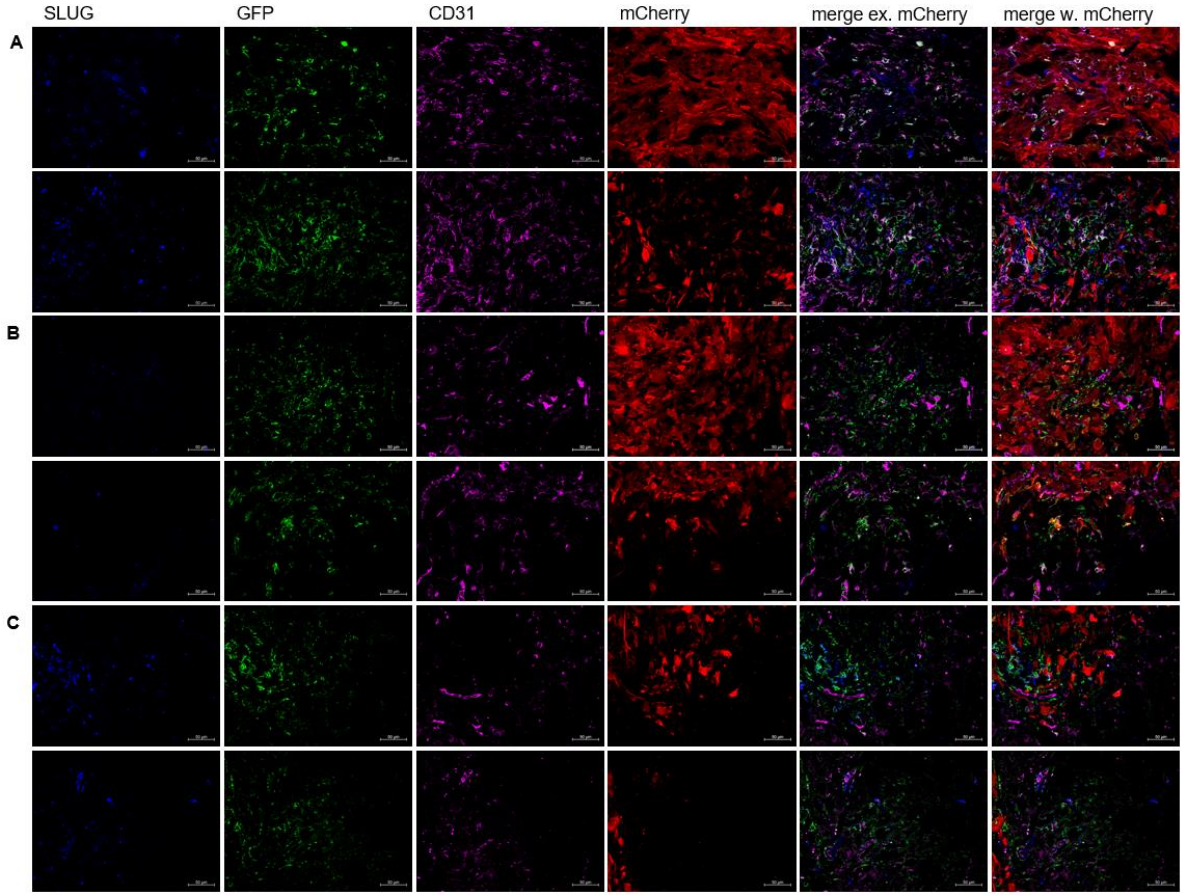

Supplementary Figure 7: Visualization of SLUG and GFP fluorescence adjacent to CD31⁺ endothelial cells in RGS5 strain mice bearing TGF-β-KO GBM. *Images show SLUG, GFP and CD31 signals in representative areas for the tumor core and the infiltration zone for each mouse of the experimental group (A, B, C). Merge pictures show overlays of all staining including the tumor (merge w. mCherry) or excluding GBM cells (merge ex. mCherry). All images were taken with 25x magnification (n=3 mice; Scale bars: 50 µm).*

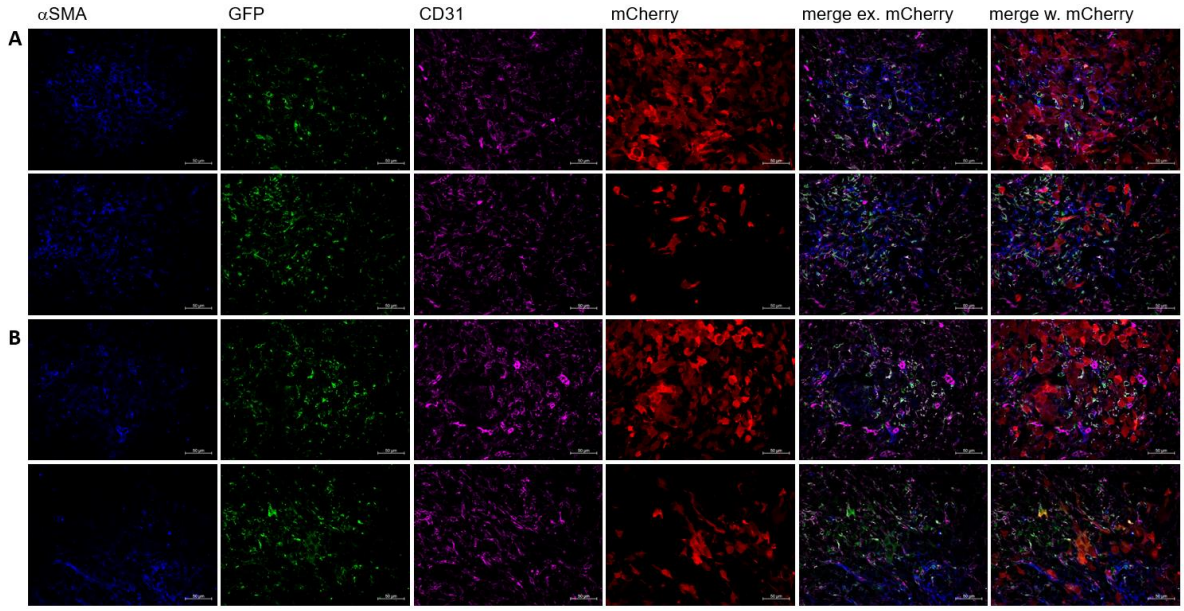

Supplementary Figure 8: Visualization of αSMA and GFP fluorescence adjacent to CD31⁺ endothelial cells in RGS5 strain mice bearing PAR GBM after injection of Lenti-V2. *Photographs show αSMA, GFP and CD31 signals in representative areas for the tumor core and the infiltration zone for each mouse of the experimental group (A, B). Merge pictures show overlays of all staining including the tumor (merge w. mCherry) or excluding GBM cells (merge ex. mCherry). All images were taken with 25x magnification (n=2 mice; Scale bars: 50 µm).*

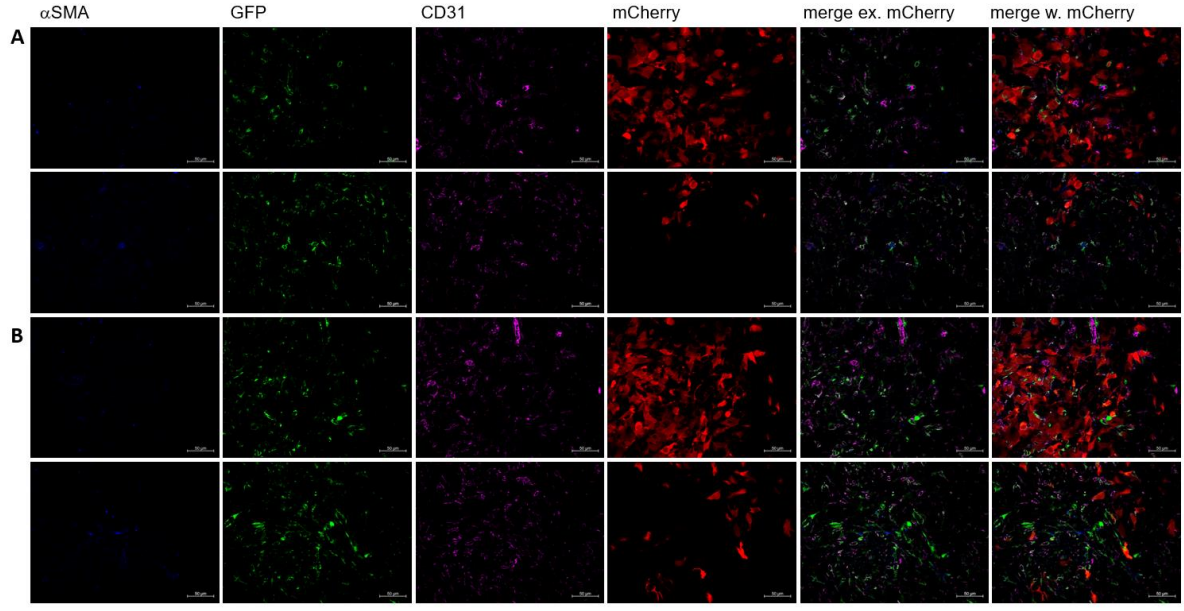

Supplementary Figure 9: Visualization of αSMA and GFP fluorescence adjacent to CD31⁺ endothelial cells in RGS5 strain mice bearing PAR GBM after injection of Lenti-SLUG-KO. *Photographs show αSMA, GFP and CD31 signals in representative areas for the tumor core and the infiltration zone for each mouse of the experimental group (A, B). Merge pictures show overlays of all staining including the tumor (merge w. mCherry) or excluding GBM cells (merge ex. mCherry). All images were taken with 25x magnification (n=2 mice; Scale bars: 50 µm).*

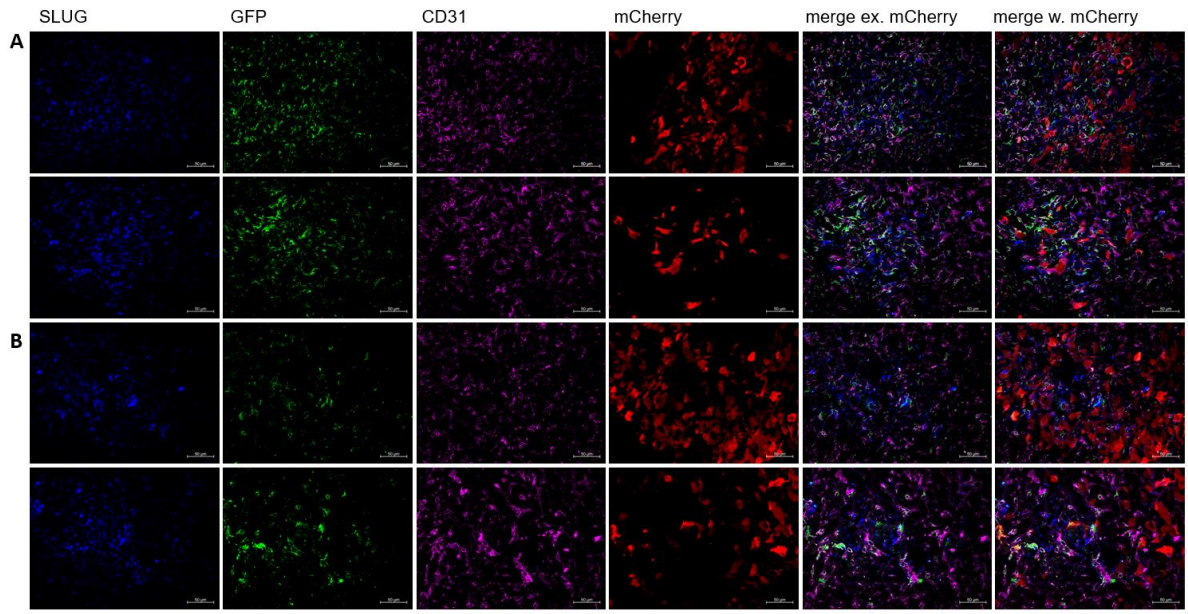

Supplementary Figure 10: Visualization of SLUG and GFP fluorescence adjacent to CD31⁺ endothelial cells in RGS5 strain mice bearing PAR GBM after injection of Lenti-V2. *Photographs show SLUG, GFP and CD31 signals in representative areas for the tumor core and the infiltration zone for each mouse of the experimental group (A, B). Merge pictures show overlays of all staining including the tumor (merge w. mCherry) or excluding GBM cells (merge ex. mCherry). All images were taken with 25x magnification (n=2 mice; Scale bars: 50 µm).*

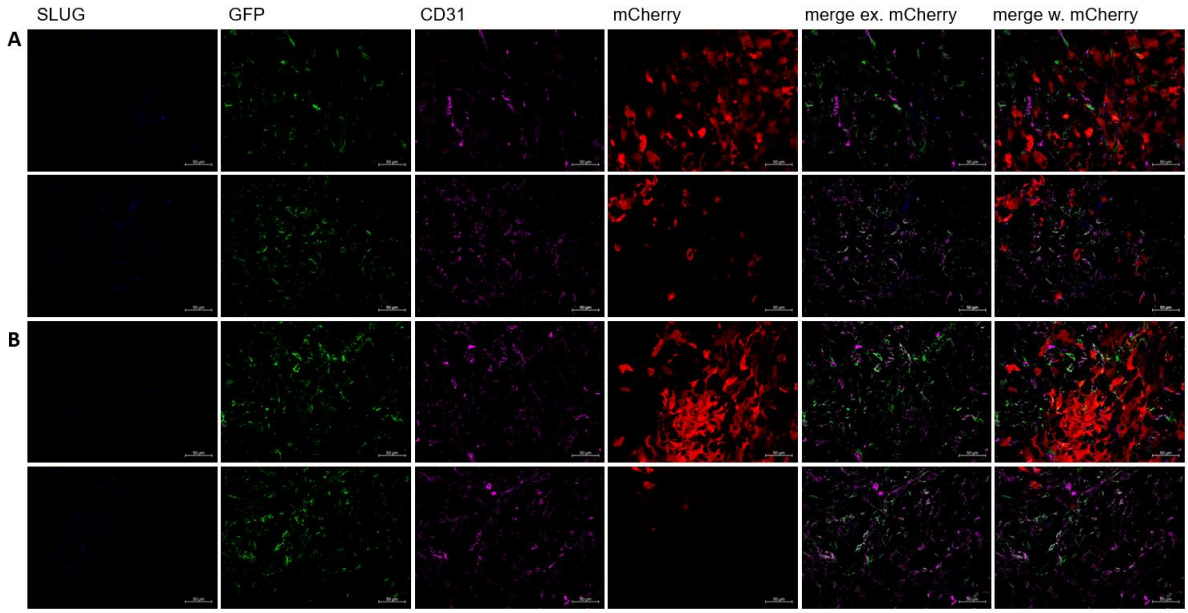

Supplementary Figure 11: Visualization of SLUG and GFP fluorescence adjacent to CD31⁺ endothelial cells in RGS5 strain mice bearing PAR GBM after injection of Lenti-SLUG-KO. *Photographs show SLUG, GFP and CD31 signals in representative areas for the tumor core and the infiltration zone for each mouse of the experimental group (A, B). Merge pictures show overlays of all staining including the tumor (merge w. mCherry) or excluding GBM cells (merge ex. mCherry). All images were taken with 25x magnification (n=2 mice; Scale bars: 50 µm).*

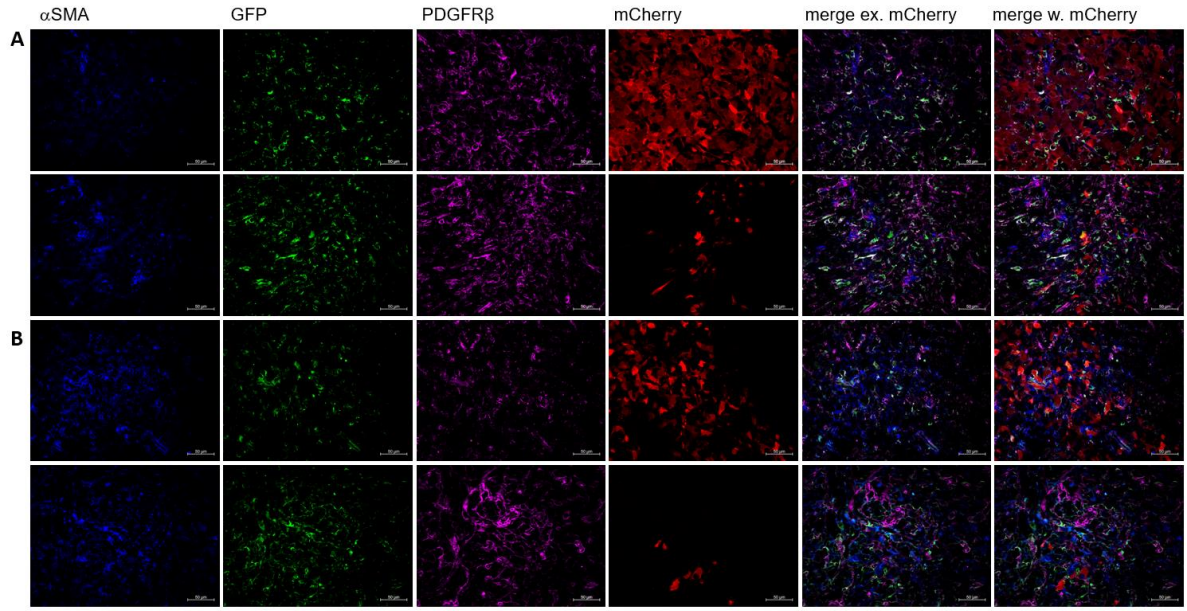

Supplementary Figure 12: Visualization of αSMA, PDGFRβ and GFP in RGS5 strain mice bearing PAR GBM after Lenti-V2 injection. *Images show αSMA, GFP and PDGFRβ fluorescence in representative areas for the tumor core and the infiltration zone for each mouse of the experimental group (A, B). Merge pictures show overlays of all staining including the tumor (merge w. mCherry) or excluding GBM cells (merge ex. mCherry). All images were taken with 25x magnification (n=2 mice; Scale bars: 50 µm).*

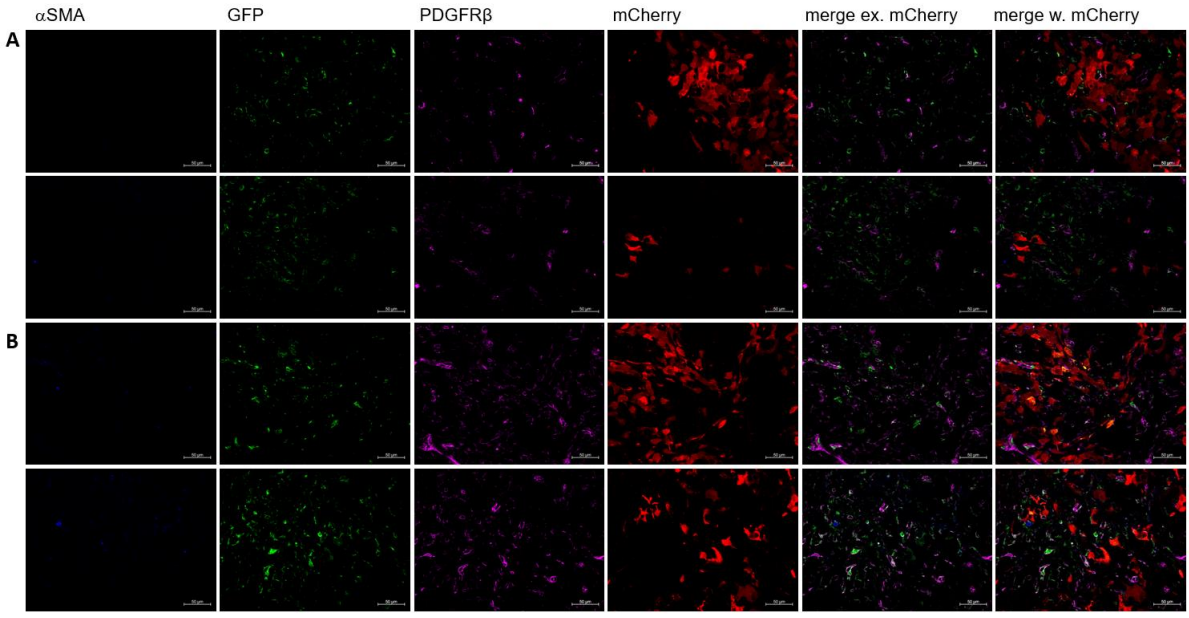

Supplementary Figure 13: Visualization of αSMA, PDGFRβ and GFP in RGS5 strain mice bearing PAR GBM after injection of Lenti-SLUG-KO. *Images show αSMA, GFP and PDGFRβ fluorescence in representative areas for the tumor core and the infiltration zone for each mouse of the experimental group (A, B). Merge pictures show overlays of all staining including the tumor (merge w. mCherry) or excluding GBM cells (merge ex. mCherry). All images were taken with 25x magnification (n=2 mice; Scale bars: 50 µm) (partly shown in Merk et al., 2024).*

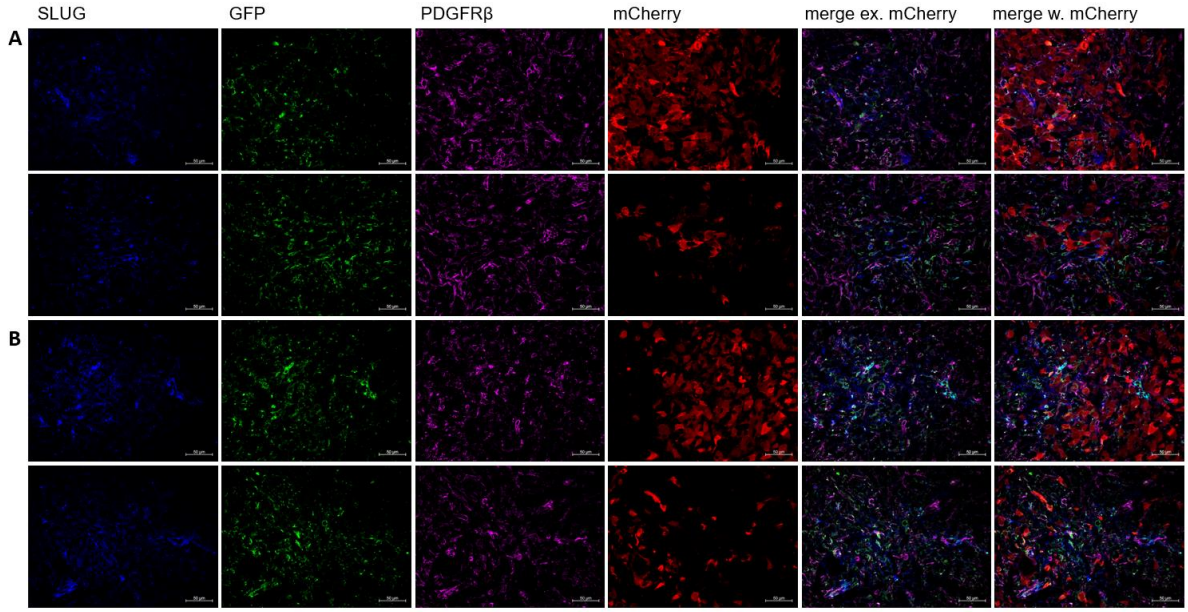

***Supplementary Figure 14*: Visualization of SLUG, PDGFRβ and GFP in RGS5 strain mice bearing PAR GBM after Lenti-V2 injection.** *Images show SLUG, GFP and PDGFRβ fluorescence in representative areas for the tumor core and the infiltration zone for each mouse of the experimental group (A, B). Merge pictures show overlays of all staining including the tumor (merge w. mCherry) or excluding GBM cells (merge ex. mCherry). All images were taken with 25x magnification (n=2 mice; Scale bars: 50 µm) (partly shown in Merk et al., 2024).*

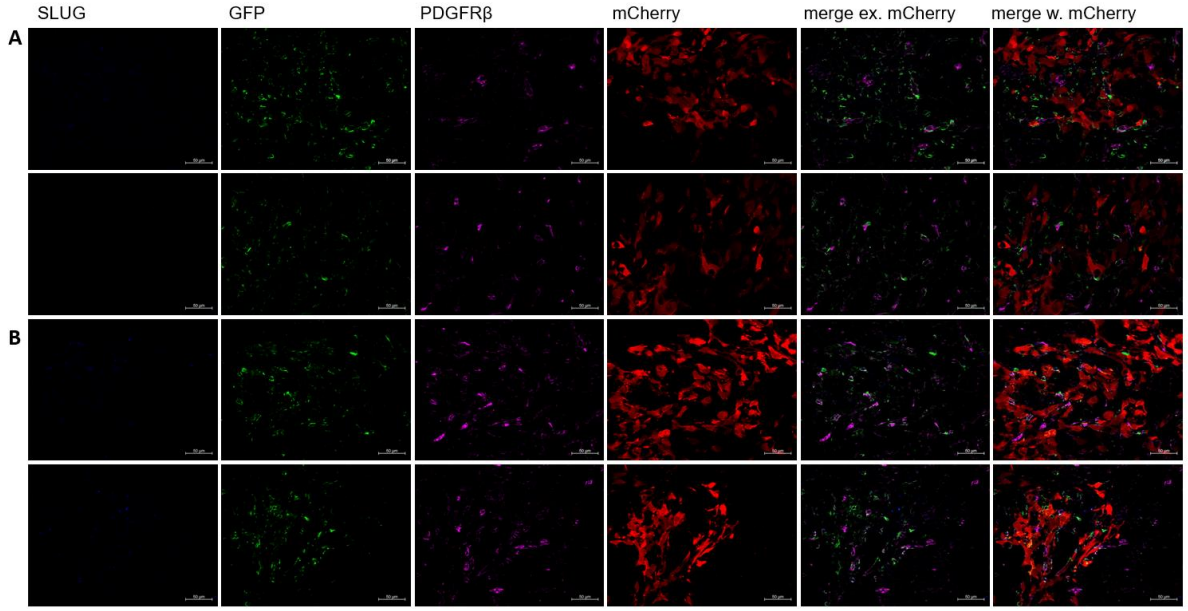

***Supplementary Figure 15*: Visualization of SLUG, PDGFRβ and GFP in RGS5 strain mice bearing PAR GBM after Lenti-SLUG-KO injection.** *Images show SLUG, GFP and PDGFRβ fluorescence in representative areas for the tumor core and the infiltration zone for each mouse of the experimental group (A, B). Merge pictures show overlays of all staining including the tumor (merge w. mCherry) or excluding GBM cells (merge ex. mCherry). All images were taken with 25x magnification (n=2 mice; Scale bars: 50 µm) (partly shown in Merk et al., 2024).*

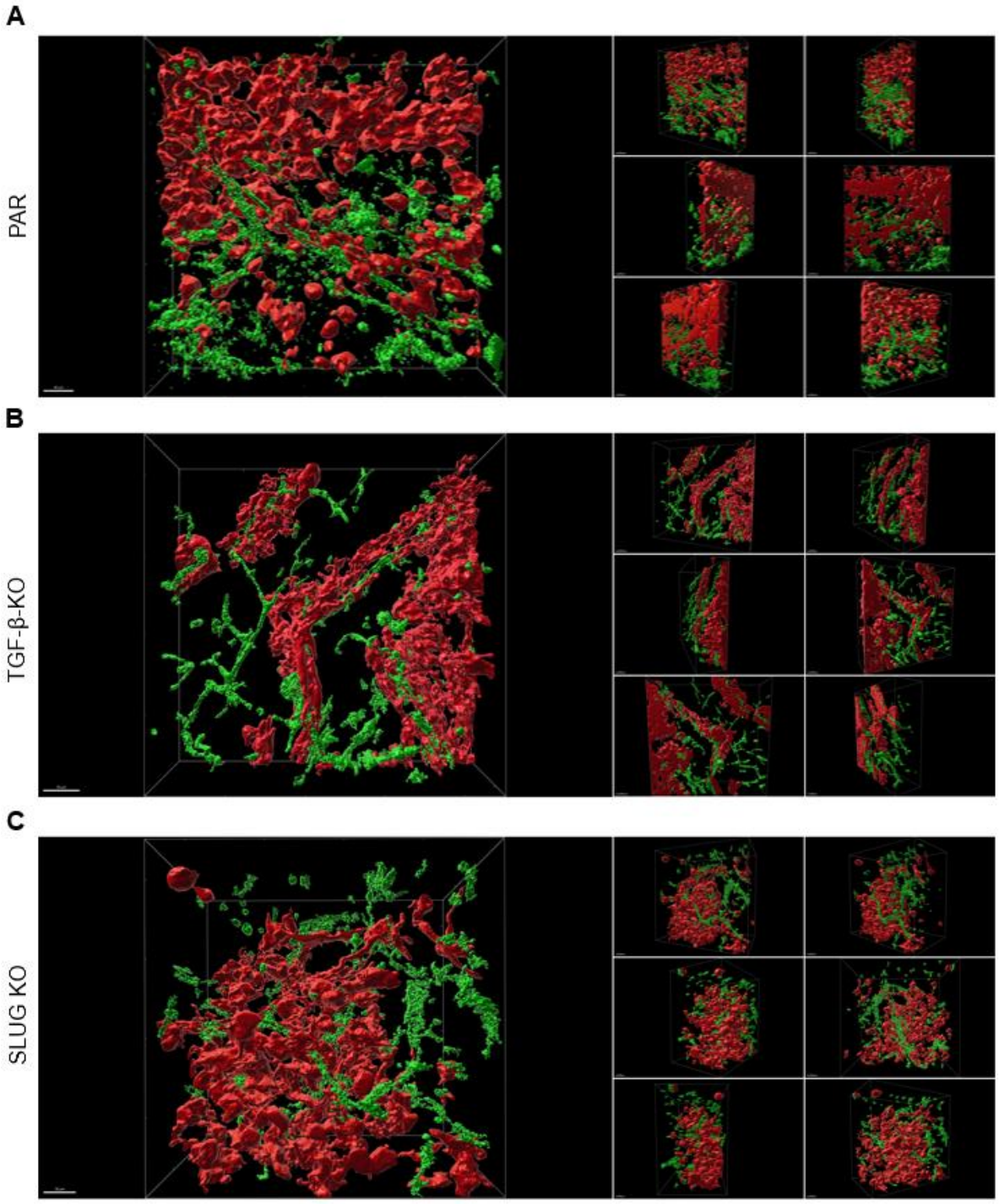

Supplementary Figure 16: Three-dimensional reconstruction of tumor-associated vessels. *Endothelial cells (CD31, green) were shown within the tumor region in RGS5 strain mice bearing either PAR GBM without further treatment (PAR; A), of mice bearing PAR tumors after intrastriatal injection of Lenti-SLUG-KO (SLUG-KO; C), or of mice bearing TGF-β-KO GBMs (TGF-β-KO; B). Tumor region is shown in different angles (smaller pictures, right side). All images are taken at 20x magnification (n=1 mouse per group; Scale bars 50 µm) (partly shown in Merk et al., 2024).*

8 Declaration of personal contribution

The work was conducted under the supervision of Prof. Dr. rer nat. Ulrike Naumann at the Hertie Institute for Clinical Brain Research in Tübingen, research group “Molecular Neurooncology”.

Unless explicitly mentioned otherwise, all work was done independently by the author of this manuscript, Luisa Merk.

The applied SLUG-KO lentiviruses were developed by Marietheres Evers, Master student.

The used TGF-β1/2-KO GBM cells were developed and characterized by Hermann Eckhardt, medical doctoral student.

All *in vivo* experiments, described in 2.2.5, were carried out by the candidate with the support of Prof. Dr. rer nat. Ulrike Naumann.

Staining protocols for all antibodies were developed in collaboration with Katja Regel, a Master student I trained and supervised during the period of my lab work. All work related to Figure 9 and Figure 10 was performed by Katja Regel under my direct supervision.

The sample clearing and staining for CLARITY was performed in collaboration with Ulrich Mattheus and PD Dr. Andreas Mack (Anatomical Institute, University of Tübingen). The following microscopy of the CLARITY samples was conducted independently by the candidate according to instructions of Ulrich Mattheus and PD Dr. Andreas Mack. 3D-Reconstruction of CLARITY samples was performed independently after consultation of Olga Oleksiuk (Responsible person for all high-tech microscopes at the Hertie Institute).

I certify that I have written this manuscript independently and have not used any sources other than those I have indicated.

The manuscript of my publication (Merk et al., 2024) was written in collaboration with Prof. Dr. rer nat. Ulrike Naumann. Therefore, my dissertation served as a template. Some of the passages have been only slightly modified, resulting in a few overlaps between my dissertation thesis and my publication which are highlighted in the text.

Tübingen,

9 Publications

Parts of this dissertation have already been published in the following publication:

Merk, L., et al. (2024). Blocking TGF-β- and Epithelial-to-Mesenchymal Transition (EMT)-mediated activation of vessel-associated mural cells in glioblastoma impacts tumor angiogenesis. *Free Neuropathology*, *5*, 4. https://doi.org/10.17879/freeneuropathology-2024-5188

10 References

Abbott, N. J., Patabendige, A. A., Dolman, D. E., Yusof, S. R., & Begley, D. J. (2010). Structure and function of the blood-brain-barrier. *Neurobiol Dis*, *37*(1), 13-25. https://doi.org/10.1016/j.nbd.2009.07.030

Akhurst, R. J., & Hata, A. (2012). Targeting the TGFβ signalling pathway in disease. *Nat Rev Drug Discov*, *11*(10), 790-811. https://doi.org/10.1038/nrd3810

Alifieris, C., & Trafalis, D. T. (2015). Glioblastoma multiforme: Pathogenesis and treatment. *Pharmacol Ther*, *152*, 63-82. https://doi.org/10.1016/j.pharmthera.2015.05.005

Ameratunga, M., Pavlakis, N., Wheeler, H., Grant, R., Simes, J. & Khasraw, M. (2018). Anti-angiogenic therapy for high-grade glioma. *Cochrane Database Syst Rev*, *11*(11), Cd008218. https://doi.org/10.1002/14651858.CD008218.pub4

Armulik, A., Abramsson, A., & Betsholtz, C. (2005). Endothelial/pericyte interactions. *Circ Res*, *97*(6), 512-523. https://doi.org/10.1161/01.RES.0000182903.16652.d7

Armulik, A., Genové, G., & Betsholtz, C. (2011). Pericytes: Developmental, Physiological, and Pathological Perspectives, Problems, and Promises. *Developmental Cell*, *21*(2), 193-215. https://doi.org/10.1016/j.devcel.2011.07.001

Attwell, D., Mishra, A., Hall, C. N., O'Farrell, F. M., & Dalkara, T. (2016). What is a pericyte? *J Cereb Blood Flow Metab*, *36*(2), 451-455. https://doi.org/10.1177/0271678x15610340

Bai, J., Varghese, J., & Jain, R. (2020). Adult Glioma WHO Classification Update, Genomics, and Imaging: What the Radiologists Need to Know. *Top Magn Reson Imaging*, *29*(2), 71-82. https://doi.org/10.1097/rmr.0000000000000234

Barthel, L., Hadamitzky, M., Dammann, P., Schedlowski, M., Sure, U., Thakur, B. K., & Hetze, S. (2022). Glioma: molecular signature and crossroads with tumor microenvironment. *Cancer Metastasis Rev*, *41*(1), 53-75. https://doi.org/10.1007/s10555-021-09997-9

Batchelor, T., et al. (2007). AZD2171, a pan-VEGF receptor tyrosine kinase inhibitor, normalizes tumor vasculature and alleviates edema in glioblastoma patients. *Cancer Cell*, *11*(1), 83-95. https://doi.org/10.1016/j.ccr.2006.11.021

Bergers, G., & Song, S. (2005). The role of pericytes in blood-vessel formation and maintenance. *Neuro Oncol*, *7*(4), 452-464. https://doi.org/10.1215/s1152851705000232

Berthiaume, A., et al. (2018). Dynamic Remodeling of Pericytes In Vivo Maintains Capillary Coverage in the Adult Mouse Brain. *Cell Rep*, *22*(1), 8-16. https://doi.org/10.1016/j.celrep.2017.12.016

Birbrair, A., et al. (2014). Type-2 pericytes participate in normal and tumoral angiogenesis. *Am J Physiol Cell Physiol*, *307*(1), C25-38. https://doi.org/10.1152/ajpcell.00084.2014

Birnbaum, T., Hildebrandt, J., Nuebling, G., Sostak, P., & Straube, A. (2011). Glioblastoma-dependent differentiation and angiogenic potential of human mesenchymal stem cells in vitro. *J Neurooncol*, *105*(1), 57-65. https://doi.org/10.1007/s11060-011-0561-1

Birner, P., et al. (2003). Vascular patterns in glioblastoma influence clinical outcome and associate with variable expression of angiogenic proteins: evidence for distinct angiogenic subtypes. *Brain Pathol*, *13*(2), 133-143. https://doi.org/10.1111/j.1750-3639.2003.tb00013.x

Bohannon, D.G., D. Long, and W.K. Kim, *Understanding the Heterogeneity of Human Pericyte Subsets in Blood-Brain Barrier Homeostasis and Neurological Diseases.* Cells, 2021. 10(4).

Bolós, V., Peinado, H., Pérez-Moreno, M. A., Fraga, M. F., Esteller, M., & Cano, A. (2003). The transcription factor Slug represses E-cadherin expression and induces epithelial to mesenchymal transitions: a comparison with Snail and E47 repressors. *J Cell Sci*, *116*(Pt 3), 499-511. https://doi.org/10.1242/jcs.00224

Bondjers, C., et al. (2003). Transcription Profiling of Platelet-Derived Growth Factor-B-Deficient Mouse Embryos Identifies RGS5 as a Novel Marker for Pericytes and Vascular Smooth Muscle Cells. *The American Journal of Pathology*, *162*(3), 721-729. https://doi.org/https://doi.org/10.1016/S0002-9440(10)63868-0

Bradbury, M. W. (1993). The blood-brain barrier. *Exp Physiol*, *78*(4), 453-472. https://doi.org/10.1113/expphysiol.1993.sp003698

Brat, D. J., et al. (2020). cIMPACT-NOW update 5: recommended grading criteria and terminologies for IDH-mutant astrocytomas. *Acta Neuropathol*, *139*(3), 603-608. https://doi.org/10.1007/s00401-020-02127-9

Bruna, A., et al. (2007). High TGFbeta-Smad activity confers poor prognosis in glioma patients and promotes cell proliferation depending on the methylation of the PDGF-B gene. *Cancer Cell*, *11*(2), 147-160. https://doi.org/10.1016/j.ccr.2006.11.023

Cano, A., et al. (2000). The transcription factor snail controls epithelial-mesenchymal transitions by repressing E-cadherin expression. *Nat Cell Biol*, *2*(2), 76-83. https://doi.org/10.1038/35000025

Carmeliet, P., & Jain, R. K. (2011). Molecular mechanisms and clinical applications of angiogenesis. *Nature*, *473*(7347), 298-307. https://doi.org/10.1038/nature10144

Carvey, P. M., Hendey, B., & Monahan, A. J. (2009). The blood-brain barrier in neurodegenerative disease: a rhetorical perspective. *J Neurochem*, *111*(2), 291-314. https://doi.org/10.1111/j.1471-4159.2009.06319.x

Caspani, E. M., Crossley, P. H., Redondo-Garcia, C., & Martinez, S. (2014). Glioblastoma: a pathogenic crosstalk between tumor cells and pericytes. *PLoS One*, *9*(7), e101402. https://doi.org/10.1371/journal.pone.0101402

Chandrasekharan, B., & Neish, A. S. (2021). Imaging the Gut with "CLARITY". *J Vis Exp*(172). https://doi.org/10.3791/62143

Cheng, J., Korte, N., Nortley, R., Sethi, H., Tang, Y., & Attwell, D. (2018). Targeting pericytes for therapeutic approaches to neurological disorders. *Acta Neuropathol*, *136*(4), 507-523. https://doi.org/10.1007/s00401-018-1893-0

Cheng, L., et al. (2013). Glioblastoma stem cells generate vascular pericytes to support vessel function and tumor growth. *Cell*, *153*(1), 139-152. https://doi.org/10.1016/j.cell.2013.02.021

Chung, K., & Deisseroth, K. (2013). CLARITY for mapping the nervous system. *Nature Methods*, *10*(6), 508-513. https://doi.org/10.1038/nmeth.2481

Chung, K., et al. (2013). Structural and molecular interrogation of intact biological systems. *Nature*, *497*(7449), 332-337. https://doi.org/10.1038/nature12107

Cicatiello, V., et al. (2015). Powerful anti-tumor and anti-angiogenic activity of a new anti-vascular endothelial growth factor receptor 1 peptide in colorectal cancer models. *Oncotarget*, *6*(12), 10563-10576. https://doi.org/10.18632/oncotarget.3384

Cohen, M. H., Shen, Y. L., Keegan, P., & Pazdur, R. (2009). FDA drug approval summary: bevacizumab (Avastin) as treatment of recurrent glioblastoma multiforme. *Oncologist*, *14*(11), 1131-1138. https://doi.org/10.1634/theoncologist.2009-0121

Colman, H., et al. (2010). A multigene predictor of outcome in glioblastoma. *Neuro Oncol*, *12*(1), 49-57. https://doi.org/10.1093/neuonc/nop007

D'Alessio, A., Proietti, G., Sica, G., & Scicchitano, B. M. (2019). Pathological and Molecular Features of Glioblastoma and Its Peritumoral Tissue. *Cancers (Basel)*, *11*(4). https://doi.org/10.3390/cancers11040469

Daneman, R., & Prat, A. (2015). The blood-brain barrier. *Cold Spring Harb Perspect Biol*, *7*(1), a020412. https://doi.org/10.1101/cshperspect.a020412

Daneman, R., Zhou, L., Kebede, A. A., & Barres, B. A. (2010). Pericytes are required for blood-brain barrier integrity during embryogenesis. *Nature*, *468*(7323), 562-566. https://doi.org/10.1038/nature09513

Darefsky, A. S., King, J. T., Jr., & Dubrow, R. (2012). Adult glioblastoma multiforme survival in the temozolomide era: a population-based analysis of Surveillance, Epidemiology, and End Results registries. *Cancer*, *118*(8), 2163-2172. https://doi.org/10.1002/cncr.26494

Daumas-Duport, C., Scheithauer, B., O'Fallon, J., & Kelly, P. (1988). Grading of astrocytomas: A simple and reproducible method. *Cancer*, *62*(10), 2152-2165. https://doi.org/10.1002/1097-0142(19881115)62:10

Davis, M. E. (2016). Glioblastoma: Overview of Disease and Treatment. *Clin J Oncol Nurs*, *20*(5 Suppl), S2-8. https://doi.org/10.1188/16.Cjon.S1.2-8

De Craene, B., Gilbert, B., Stove, C., Bruyneel, E., van Roy, F., & Berx, G. (2005). The transcription factor snail induces tumor cell invasion through modulation

of the epithelial cell differentiation program. *Cancer Res*, *65*(14), 6237-6244. https://doi.org/10.1158/0008-5472.Can-04-3545

Derynck, R., & Zhang, Y. E. (2003). Smad-dependent and Smad-independent pathways in TGF-beta family signaling. *Nature*, *425*(6958), 577-584. https://doi.org/10.1038/nature02006

Diaz, R. J., Ali, S., Qadir, M. G., De La Fuente, M. I., Ivan, M. E., & Komotar, R. J. (2017). The role of bevacizumab in the treatment of glioblastoma. *Journal of Neuro-Oncology*, *133*(3), 455-467. https://doi.org/10.1007/s11060-017-2477-x

Dieterich, L. C., et al. (2012). Transcriptional profiling of human glioblastoma vessels indicates a key role of VEGF-A and TGFβ2 in vascular abnormalization. *The Journal of Pathology*, *228*(3), 378-390. https://doi.org/https://doi.org/10.1002/path.4072

Du, H., Hou, P., Zhang, W., & Li, Q. (2018). Advances in CLARITY-based tissue clearing and imaging. *Exp Ther Med*, *16*(3), 1567-1576. https://doi.org/10.3892/etm.2018.6374

Dubrac, A., et al. (2018). NCK-dependent pericyte migration promotes pathological neovascularization in ischemic retinopathy. *Nat Commun*, *9*(1), 3463. https://doi.org/10.1038/s41467-018-05926-7

Eigenbrod, S., et al. (2014). Molecular stereotactic biopsy technique improves diagnostic accuracy and enables personalized treatment strategies in glioma patients. *Acta Neurochirurgica*, *156*(8), 1427-1440. https://doi.org/10.1007/s00701-014-2073-1

Eilken, H. M., et al. (2017). Pericytes regulate VEGF-induced endothelial sprouting through VEGFR1. *Nature Communications*, *8*(1), 1574. https://doi.org/10.1038/s41467-017-01738-3

Elias, M. C., Tozer, K. R., Silber, et al. (2005). TWIST is expressed in human gliomas and promotes invasion. *Neoplasia*, *7*(9), 824-837. https://doi.org/10.1593/neo.04352

Fisher, M. (2009). Pericyte signaling in the neurovascular unit. *Stroke*, *40*(3 Suppl), S13-15. https://doi.org/10.1161/strokeaha.108.533117

Fricano-Kugler, C. J., Williams, M. R., Salinaro, J. R., Li, M., & Luikart, B. (2016). Designing, Packaging, and Delivery of High Titer CRISPR Retro and Lentiviruses via Stereotaxic Injection. *J Vis Exp*(111). https://doi.org/10.3791/53783

Fuxe, J., & Karlsson, M. C. (2012). TGF-β-induced epithelial-mesenchymal transition: a link between cancer and inflammation. *Semin Cancer Biol*, *22*(5-6), 455-461. https://doi.org/10.1016/j.semcancer.2012.05.004

Gerhardt, H., & Betsholtz, C. (2003). Endothelial-pericyte interactions in angiogenesis. *Cell Tissue Res*, *314*(1), 15-23. https://doi.org/10.1007/s00441-003-0745-x

Gerhardt, H., et al. (2003). VEGF guides angiogenic sprouting utilizing endothelial tip cell filopodia. *J Cell Biol*, *161*(6), 1163-1177. https://doi.org/10.1083/jcb.200302047

Gieryng, A., Pszczolkowska, D., Walentynowicz, K. A., Rajan, W. D., & Kaminska, B. (2017). Immune microenvironment of gliomas. *Lab Invest*, *97*(5), 498-518. https://doi.org/10.1038/labinvest.2017.19

Gilbert, M. R., et al. (2014). A randomized trial of bevacizumab for newly diagnosed glioblastoma. *N Engl J Med*, *370*(8), 699-708. https://doi.org/10.1056/NEJMoa1308573

Greenberg, J. I., et al. (2008). A role for VEGF as a negative regulator of pericyte function and vessel maturation. *Nature*, *456*(7223), 809-813. https://doi.org/10.1038/nature07424

Guerra, D. A. P., et al. (2018). Targeting glioblastoma-derived pericytes improves chemotherapeutic outcome. *Angiogenesis*, *21*(4), 667-675. https://doi.org/10.1007/s10456-018-9621-x

Hajra, K. M., Chen, D. Y., & Fearon, E. R. (2002). The SLUG zinc-finger protein represses E-cadherin in breast cancer. *Cancer Res*, *62*(6), 1613-1618.

Han, J., Alvarez-Breckenridge, C. A., Wang, Q. E., & Yu, J. (2015). TGF-β signaling and its targeting for glioma treatment. *Am J Cancer Res*, *5*(3), 945-955.

Hanif, F., Muzaffar, K., Perveen, K., Malhi, S. M., & Simjee Sh, U. (2017). Glioblastoma Multiforme: A Review of its Epidemiology and Pathogenesis through Clinical Presentation and Treatment. *Asian Pac J Cancer Prev*, *18*(1), 3-9. https://doi.org/10.22034/apjcp.2017.18.1.3

Hardee, M. E., & Zagzag, D. (2012). Mechanisms of glioma-associated neovascularization. *Am J Pathol*, *181*(4), 1126-1141. https://doi.org/10.1016/j.ajpath.2012.06.030

Hegi, M. E., et al. (2005). MGMT gene silencing and benefit from temozolomide in glioblastoma. *N Engl J Med*, *352*(10), 997-1003. https://doi.org/10.1056/NEJMoa043331

Hellström, M., Gerhardt, H., Kalén, M., Li, X., Eriksson, U., Wolburg, H., & Betsholtz, C. (2001). Lack of pericytes leads to endothelial hyperplasia and abnormal vascular morphogenesis. *J Cell Biol*, *153*(3), 543-553. https://doi.org/10.1083/jcb.153.3.543

Holash, J., et al. (1999). Vessel Cooption, Regression, and Growth in Tumors Mediated by Angiopoietins and VEGF. *Science*, *284*(5422), 1994-1998. https://doi.org/10.1126/science.284.5422.1994

Holderfield, M. T., & Hughes, C. C. (2008). Crosstalk between vascular endothelial growth factor, notch, and transforming growth factor-beta in vascular morphogenesis. *Circ Res*, *102*(6), 637-652. https://doi.org/10.1161/circresaha.107.167171

Hoque, M. M., Abdelazim, H., Jenkins-Houk, C., Wright, D., Patel, B. M., & Chappell, J. C. (2020). The cerebral microvasculature: Basic and clinical perspectives on stroke and glioma. *Microcirculation*, *28*(3), e12671. https://doi.org/10.1111/micc.12671

Hosono, J., Morikawa, S., Ezaki, T., Kawamata, T., & Okada, Y. (2017). Pericytes promote abnormal tumor angiogenesis in a rat RG2 glioma model. *Brain Tumor Pathol*, *34*(3), 120-129. https://doi.org/10.1007/s10014-017-0291-y

Huang, B., et al. (2020). Current Immunotherapies for Glioblastoma Multiforme. *Front Immunol*, *11*, 603911. https://doi.org/10.3389/fimmu.2020.603911

Huang, H., Wright, S., Zhang, J., & Brekken, R. A. (2019). Getting a grip on adhesion: Cadherin switching and collagen signaling. *Biochim Biophys Acta Mol Cell Res*, *1866*(11), 118472. https://doi.org/10.1016/j.bbamcr.2019.04.002

Iacob, G., & Dinca, E. B. (2009). Current data and strategy in glioblastoma multiforme. *J Med Life*, *2*(4), 386-393.
Ikenouchi, J., Matsuda, M., Furuse, M., & Tsukita, S. (2003). Regulation of tight junctions during the epithelium-mesenchyme transition: direct repression of the gene expression of claudins/occludin by Snail. *J Cell Sci*, *116*(Pt 10), 1959-1967. https://doi.org/10.1242/jcs.00389
Ikushima, H., & Miyazono, K. (2010). TGFbeta signalling: a complex web in cancer progression. *Nat Rev Cancer*, *10*(6), 415-424. https://doi.org/10.1038/nrc2853
Iwadate, Y. (2016). Epithelial-mesenchymal transition in glioblastoma progression. *Oncol Lett*, *11*(3), 1615-1620. https://doi.org/10.3892/ol.2016.4113
Jackson, S., ElAli, A., Virgintino, D., & Gilbert, M. R. (2017). Blood-brain barrier pericyte importance in malignant gliomas: what we can learn from stroke and Alzheimer's disease. *Neuro Oncol*, *19*(9), 1173-1182. https://doi.org/10.1093/neuonc/nox058
Jain, R. K., di Tomaso, E., Duda, D. G., Loeffler, J. S., Sorensen, A. G., & Batchelor, T. T. (2007). Angiogenesis in brain tumours. *Nat Rev Neurosci*, *8*(8), 610-622. https://doi.org/10.1038/nrn2175
Jensen, K. H. R., & Berg, R. W. (2017). Advances and perspectives in tissue clearing using CLARITY. *Journal of Chemical Neuroanatomy*, *86*, 19-34. https://doi.org/https://doi.org/10.1016/j.jchemneu.2017.07.005
Joseph, J. V., Balasubramaniyan, V., Walenkamp, A., & Kruyt, F. A. E. (2013). TGF-β as a therapeutic target in high grade gliomas – Promises and challenges. *Biochemical Pharmacology*, *85*(4), 478-485. https://doi.org/https://doi.org/10.1016/j.bcp.2012.11.005
Kahlert, U. D., Nikkhah, G., & Maciaczyk, J. (2013). Epithelial-to-mesenchymal(-like) transition as a relevant molecular event in malignant gliomas. *Cancer Letters*, *331*(2), 131-138. https://doi.org/https://doi.org/10.1016/j.canlet.2012.12.010
Kane, J. R. (2019). The Role of Brain Vasculature in Glioblastoma. *Mol Neurobiol*, *56*(9), 6645-6653. https://doi.org/10.1007/s12035-019-1561-y
Katsuno, Y., Lamouille, S., & Derynck, R. (2013). TGF-β signaling and epithelial-mesenchymal transition in cancer progression. *Curr Opin Oncol*, *25*(1), 76-84. https://doi.org/10.1097/CCO.0b013e32835b6371
Kerbel, R. S. (2008). Tumor angiogenesis. *N Engl J Med*, *358*(19), 2039-2049. https://doi.org/10.1056/NEJMra0706596
Keunen, O., et al. (2011). Anti-VEGF treatment reduces blood supply and increases tumor cell invasion in glioblastoma. *Proc Natl Acad Sci U S A*, *108*(9), 3749-3754. https://doi.org/10.1073/pnas.1014480108
Kjellman, C., et al. (2000). Expression of TGF-beta isoforms, TGF-beta receptors, and SMAD molecules at different stages of human glioma. *Int J Cancer*, *89*(3), 251-258. https://doi.org/10.1002/1097-0215(20000520)89:3<251::aid-ijc7>3.0.co;2-5
Krueger, M., & Bechmann, I. (2010). CNS pericytes: Concepts, misconceptions, and a way out. *Glia*, *58*(1), 1-10. https://doi.org/https://doi.org/10.1002/glia.20898
Kubelt, C., Hattermann, K., Sebens, S., Mehdorn, H. M., & Held-Feindt, J. (2015). Epithelial-to-mesenchymal transition in paired human primary and recurrent

glioblastomas. *Int J Oncol*, *46*(6), 2515-2525. https://doi.org/10.3892/ijo.2015.2944
Kumar, S., & Arbab, A. S. (2013). Neovascularization in Glioblastoma: Current Pitfall in Anti-angiogenic therapy. *Zhong Liu Za Zhi*, *1*(3), 16-19.
Kunz, J., Krause, D., Kremer, M., & Dermietzel, R. (1994). The 140-kDa protein of blood-brain barrier-associated pericytes is identical to aminopeptidase N. *J Neurochem*, *62*(6), 2375-2386. https://doi.org/10.1046/j.1471-4159.1994.62062375.x
Liebner, S., Dijkhuizen, R. M., Reiss, Y., Plate, K. H., Agalliu, D., & Constantin, G. (2018). Functional morphology of the blood-brain barrier in health and disease. *Acta Neuropathol*, *135*(3), 311-336. https://doi.org/10.1007/s00401-018-1815-1
Lindahl, P., Johansson, B. R., Levéen, P., & Betsholtz, C. (1997). Pericyte loss and microaneurysm formation in PDGF-B-deficient mice. *Science*, *277*(5323), 242-245. https://doi.org/10.1126/science.277.5323.242
Liu, A. K., et al. (2016). Bringing CLARITY to the human brain: visualization of Lewy pathology in three dimensions. *Neuropathol Appl Neurobiol*, *42*(6), 573-587. https://doi.org/10.1111/nan.12293
Liu, A. Y., & Ouyang, G. (2013). Tumor angiogenesis: a new source of pericytes. *Curr Biol*, *23*(13), R565-568. https://doi.org/10.1016/j.cub.2013.05.023
Liu, Y., et al. (2014). Multidimensional analysis of gene expression reveals TGFB1I1-induced EMT contributes to malignant progression of astrocytomas. *Oncotarget*, *5*(24), 12593-12606. https://doi.org/10.18632/oncotarget.2518
Louis, D. N., et al. (2007). The 2007 WHO classification of tumours of the central nervous system. *Acta Neuropathol*, *114*(2), 97-109. https://doi.org/10.1007/s00401-007-0243-4
Louis, D. N., et al. (2016). The 2016 World Health Organization Classification of Tumors of the Central Nervous System: a summary. *Acta Neuropathologica*, *131*(6), 803-820. https://doi.org/10.1007/s00401-016-1545-1
Louis, D. N., et al. (2021). The 2021 WHO Classification of Tumors of the Central Nervous System: a summary. *Neuro Oncol*, *23*(8), 1231-1251. https://doi.org/10.1093/neuonc/noab106
Mäder, L., et al. (2018). Pericytes/vessel-associated mural cells (VAMCs) are the major source of key epithelial-mesenchymal transition (EMT) factors SLUG and TWIST in human glioma. *Oncotarget*, *9*.
Mäe, M. A., et al. (2021). Single-Cell Analysis of Blood-Brain Barrier Response to Pericyte Loss. *Circ Res*, *128*(4), e46-e62. https://doi.org/10.1161/circresaha.120.317473
Mahabir, R., et al. (2014). Sustained elevation of Snail promotes glial-mesenchymal transition after irradiation in malignant glioma. *Neuro Oncol*, *16*(5), 671-685. https://doi.org/10.1093/neuonc/not239
Martin, J. D., Seano, G., & Jain, R. K. (2019). Normalizing Function of Tumor Vessels: Progress, Opportunities, and Challenges. *Annu Rev Physiol*, *81*, 505-534. https://doi.org/10.1146/annurev-physiol-020518-114700
Merk, L., et al. (2024). Blocking TGF-β- and Epithelial-to-Mesenchymal Transition (EMT)-mediated activation of vessel-associated mural cells in glioblastoma impacts tumor angiogenesis. *Free Neuropathology*, *5*, 4.

https://doi.org/10.17879/freeneuropathology-2024-5188
Miyazono, K., Ehata, S., & Koinuma, D. (2012). Tumor-promoting functions of transforming growth factor-β in progression of cancer. *Ups J Med Sci*, *117*(2), 143-152. https://doi.org/10.3109/03009734.2011.638729
Moreno-Bueno, G., Portillo, F., & Cano, A. (2008). Transcriptional regulation of cell polarity in EMT and cancer. *Oncogene*, *27*(55), 6958-6969. https://doi.org/10.1038/onc.2008.346
Morikawa, S., Baluk, P., Kaidoh, T., Haskell, A., Jain, R. K., & McDonald, D. M. (2002). Abnormalities in pericytes on blood vessels and endothelial sprouts in tumors. *Am J Pathol*, *160*(3), 985-1000. https://doi.org/10.1016/s0002-9440(10)64920-6
Moustakas, A., & Heldin, C. H. (2005). Non-Smad TGF-beta signals. *J Cell Sci*, *118*(Pt 16), 3573-3584. https://doi.org/10.1242/jcs.02554
Moustakas, A., & Heldin, P. (2014). TGFβ and matrix-regulated epithelial to mesenchymal transition. *Biochimica et Biophysica Acta (BBA) - General Subjects*, *1840*(8), 2621-2634. https://doi.org/https://doi.org/10.1016/j.bbagen.2014.02.004
Mustafa, D., et al. (2013). Structural and expression differences between the vasculature of pilocytic astrocytomas and glioblastomas. *Journal of neuropathology and experimental neurology*, *72*(12), 1171-1181. https://doi.org/10.1097/nen.0000000000000015
Nakada, M., et al. (2011). Aberrant signaling pathways in glioma. *Cancers (Basel)*, *3*(3), 3242-3278. https://doi.org/10.3390/cancers3033242
Narayana, A., et al. (2009). Antiangiogenic therapy using bevacizumab in recurrent high-grade glioma: impact on local control and patient survival. *Journal of neurosurgery*, *110*(1), 173-180. https://doi.org/10.3171/2008.4.17492
Nduom, E. K., Weller, M., & Heimberger, A. B. (2015). Immunosuppressive mechanisms in glioblastoma. *Neuro Oncol*, *17 Suppl 7*(Suppl 7), vii9-vii14. https://doi.org/10.1093/neuonc/nov151
Nehls, V., Denzer, K., & Drenckhahn, D. (1992). Pericyte involvement in capillary sprouting during angiogenesis in situ. *Cell and Tissue Research*, *270*(3), 469-474. https://doi.org/10.1007/BF00645048
Nehls, V., & Drenckhahn, D. (1991). Heterogeneity of microvascular pericytes for smooth muscle type alpha-actin. *J Cell Biol*, *113*(1), 147-154. https://doi.org/10.1083/jcb.113.1.147
Nisancioglu, M. H., et al. (2008). Generation and characterization of rgs5 mutant mice. *Mol Cell Biol*, *28*(7), 2324-2331. https://doi.org/10.1128/mcb.01252-07
Noch, E. K., Ramakrishna, R., & Magge, R. (2018). Challenges in the Treatment of Glioblastoma: Multisystem Mechanisms of Therapeutic Resistance. *World Neurosurg*, *116*, 505-517. https://doi.org/10.1016/j.wneu.2018.04.022
Oberoi, R. K., Parrish, K. E., Sio, T. T., Mittapalli, R. K., Elmquist, W. F., & Sarkaria, J. N. (2015). Strategies to improve delivery of anticancer drugs across the blood–brain barrier to treat glioblastoma. *Neuro-Oncology*, *18*(1), 27-36. https://doi.org/10.1093/neuonc/nov164
Ochs, K., et al. (2013). Immature mesenchymal stem cell-like pericytes as mediators of immunosuppression in human malignant glioma. *Journal of*

Neuroimmunology, *265*(1), 106-116. https://doi.org/https://doi.org/10.1016/j.jneuroim.2013.09.011
Oh, S. J., et al. (2019). The Role Played by SLUG, an Epithelial–Mesenchymal Transition Factor, in Invasion and Therapeutic Resistance of Malignant Glioma. *Cellular and Molecular Neurobiology*, *39*(6), 769-782. https://doi.org/10.1007/s10571-019-00677-5
Ohgaki, H., & Kleihues, P. (2007). Genetic pathways to primary and secondary glioblastoma. *Am J Pathol*, *170*(5), 1445-1453. https://doi.org/10.2353/ajpath.2007.070011
Ohgaki, H., & Kleihues, P. (2013). The definition of primary and secondary glioblastoma. *Clin Cancer Res*, *19*(4), 764-772. https://doi.org/10.1158/1078-0432.Ccr-12-3002
Omuro, A., & DeAngelis, L. M. (2013). Glioblastoma and other malignant gliomas: a clinical review. *Jama*, *310*(17), 1842-1850. https://doi.org/10.1001/jama.2013.280319
Ostrom, Q. T., Cioffi, G., Waite, K., Kruchko, C., & Barnholtz-Sloan, J. S. (2021). CBTRUS Statistical Report: Primary Brain and Other Central Nervous System Tumors Diagnosed in the United States in 2014-2018. *Neuro Oncol*, *23*(12 Suppl 2), iii1-iii105. https://doi.org/10.1093/neuonc/noab200
Ostrom, Q. T., Gittleman, H., Truitt, G., Boscia, A., Kruchko, C., & Barnholtz-Sloan, J. S. (2018). CBTRUS Statistical Report: Primary Brain and Other Central Nervous System Tumors Diagnosed in the United States in 2011–2015. *Neuro-Oncology*, *20*(suppl_4), iv1-iv86. https://doi.org/10.1093/neuonc/noy131
Ozerdem, U., Grako, K. A., Dahlin-Huppe, K., Monosov, E., & Stallcup, W. B. (2001). NG2 proteoglycan is expressed exclusively by mural cells during vascular morphogenesis. *Dev Dyn*, *222*(2), 218-227. https://doi.org/10.1002/dvdy.1200
Ozerdem, U., & Stallcup, W. B. (2003). Early contribution of pericytes to angiogenic sprouting and tube formation. *Angiogenesis*, *6*(3), 241-249. https://doi.org/10.1023/B:AGEN.0000021401.58039.a9
Parrish, K. E., Sarkaria, J. N., & Elmquist, W. F. (2015). Improving drug delivery to primary and metastatic brain tumors: strategies to overcome the blood-brain barrier. *Clin Pharmacol Ther*, *97*(4), 336-346. https://doi.org/10.1002/cpt.71
Patel, A. P., et al. (2014). Single-cell RNA-seq highlights intratumoral heterogeneity in primary glioblastoma. *Science*, *344*(6190), 1396-1401. https://doi.org/10.1126/science.1254257
Peach, C. J., et al. (2018). Molecular Pharmacology of VEGF-A Isoforms: Binding and Signalling at VEGFR2. *Int J Mol Sci*, *19*(4). https://doi.org/10.3390/ijms19041264
Pickup, M., Novitskiy, S., & Moses, H. L. (2013). The roles of TGFβ in the tumour microenvironment. *Nat Rev Cancer*, *13*(11), 788-799. https://doi.org/10.1038/nrc3603
Pieper, C., Marek, J. J., Unterberg, M., Schwerdtle, T., & Galla, H. J. (2014). Brain capillary pericytes contribute to the immune defense in response to cytokines or LPS in vitro. *Brain Res*, *1550*, 1-8. https://doi.org/10.1016/j.brainres.2014.01.004

Platten, M., Wick, W., & Weller, M. (2001). Malignant glioma biology: role for TGF-beta in growth, motility, angiogenesis, and immune escape. *Microsc Res Tech*, *52*(4), 401-410. https://doi.org/10.1002/1097-0029(20010215)52:4

Poguzhelskaya, E., Artamonov, D., Bolshakova, A., Vlasova, O., & Bezprozvanny, I. (2014). Simplified method to perform CLARITY imaging. *Mol Neurodegener*, *9*, 19. https://doi.org/10.1186/1750-1326-9-19

Polivka, J., et al. (2017). Advances in Experimental Targeted Therapy and Immunotherapy for Patients with Glioblastoma Multiforme. *Anticancer Research*, *37*. https://doi.org/10.21873/anticanres.11285

Poon, M. T. C., Sudlow, C. L. M., Figueroa, J. D., & Brennan, P. M. (2020). Longer-term (≥ 2 years) survival in patients with glioblastoma in population-based studies pre- and post-2005: a systematic review and meta-analysis. *Scientific Reports*, *10*(1), 11622. https://doi.org/10.1038/s41598-020-68011-4

Profaci, C. P., Munji, R. N., Pulido, R. S., & Daneman, R. (2020). The blood-brain barrier in health and disease: Important unanswered questions. *J Exp Med*, *217*(4). https://doi.org/10.1084/jem.20190062

Ribatti, D., Nico, B., & Crivellato, E. (2011). The role of pericytes in Angiogenesis. *The International journal of developmental biology*, *55*, 261-268. https://doi.org/10.1387/ijdb.103167dr

Ricci-Vitiani, L., et al. (2010). Tumour vascularization via endothelial differentiation of glioblastoma stem-like cells. *Nature*, *468*(7325), 824-828. https://doi.org/10.1038/nature09557

Richardson, D. S., & Lichtman, J. W. (2015). Clarifying Tissue Clearing. *Cell*, *162*(2), 246-257. https://doi.org/10.1016/j.cell.2015.06.067

Rock, K., et al. (2012). A clinical review of treatment outcomes in glioblastoma multiforme- the validation in a non-trial population of the results of a randomised Phase III clinical trial: has a more radical approach improved survival? *Br J Radiol*, *85*(1017), e729-733. https://doi.org/10.1259/bjr/83796755

Roy, L. O., Poirier, M. B., & Fortin, D. (2015). Transforming growth factor-beta and its implication in the malignancy of gliomas. *Target Oncol*, *10*(1), 1-14. https://doi.org/10.1007/s11523-014-0308-y

Rucker, H. K., Wynder, H. J., & Thomas, W. E. (2000). Cellular mechanisms of CNS pericytes. *Brain Res Bull*, *51*(5), 363-369. https://doi.org/10.1016/s0361-9230(99)00260-9

Rustenhoven, J., et al. (2016). TGF-beta1 regulates human brain pericyte inflammatory processes involved in neurovasculature function. *J Neuroinflammation*, *13*, 37. https://doi.org/10.1186/s12974-016-0503-0

Sattiraju, A., & Mintz, A. (2019). Pericytes in Glioblastomas: Multifaceted Role Within Tumor Microenvironments and Potential for Therapeutic Interventions. *Adv Exp Med Biol*, *1147*, 65-91. https://doi.org/10.1007/978-3-030-16908-4_2

Scandella, V., Paolicelli, R. C., & Knobloch, M. (2020). A novel protocol to detect green fluorescent protein in unfixed, snap-frozen tissue. *Scientific Reports*, *10*(1), 14642. https://doi.org/10.1038/s41598-020-71493-x

Schiffer, D., Annovazzi, L., Casalone, C., Corona, C., & Mellai, M. (2018). Glioblastoma: Microenvironment and Niche Concept. *Cancers (Basel)*, *11*(1). https://doi.org/10.3390/cancers11010005

Schulz-Schaeffer, W. J. (2016). Neuerungen der WHO-Klassifikation der Hirntumore von 2016. *Der Radiologe*, *57*(9), 701-706. https://doi.org/10.1007/s00117-017-0290-3

Schumacher, L., et al. (2023). TGF-Beta Modulates the Integrity of the Blood Brain Barrier In Vitro, and Is Associated with Metabolic Alterations in Pericytes. *Biomedicines*, *11*(1), 214. https://www.mdpi.com/2227-9059/11/1/214

Sena, I. F. G., et al. (2018). Glioblastoma-activated pericytes support tumor growth via immunosuppression. *Cancer Med*, *7*(4), 1232-1239. https://doi.org/10.1002/cam4.1375

Siemann, D. W. (2011). The unique characteristics of tumor vasculature and preclinical evidence for its selective disruption by Tumor-Vascular Disrupting Agents. *Cancer Treat Rev*, *37*(1), 63-74. https://doi.org/10.1016/j.ctrv.2010.05.001

Smith, C., & Ironside, J. W. (2007). Diagnosis and pathogenesis of gliomas. *Current Diagnostic Pathology*, *13*(3), 180-192. https://doi.org/https://doi.org/10.1016/j.cdip.2007.04.002

Stenzel, D., Nye, E., Nisancioglu, M., Adams, R. H., Yamaguchi, Y., & Gerhardt, H. (2009). Peripheral mural cell recruitment requires cell-autonomous heparan sulfate. *Blood*, *114*(4), 915-924. https://doi.org/https://doi.org/10.1182/blood-2008-10-186239

Stupp, R., et al. (2005). Radiotherapy plus concomitant and adjuvant temozolomide for glioblastoma. *N Engl J Med*, *352*(10), 987-996. https://doi.org/10.1056/NEJMoa043330

Sun, H., et al. (2014). Hyperplasia of pericytes is one of the main characteristics of microvascular architecture in malignant glioma. *PLoS One*, *9*(12), e114246. https://doi.org/10.1371/journal.pone.0114246

Sung, H., et al. (2021). Global Cancer Statistics 2020: GLOBOCAN Estimates of Incidence and Mortality Worldwide for 36 Cancers in 185 Countries. *CA Cancer J Clin*, *71*(3), 209-249. https://doi.org/10.3322/caac.21660

Svensson, A., Özen, I., Genové, G., Paul, G., & Bengzon, J. (2015). Endogenous brain pericytes are widely activated and contribute to mouse glioma microvasculature. *PLoS One*, *10*(4), e0123553. https://doi.org/10.1371/journal.pone.0123553

Sweeney, M., & Foldes, G. (2018). It Takes Two: Endothelial-Perivascular Cell Cross-Talk in Vascular Development and Disease. *Front Cardiovasc Med*, *5*, 154. https://doi.org/10.3389/fcvm.2018.00154

Sweeney, M. D., Ayyadurai, S., & Zlokovic, B. V. (2016). Pericytes of the neurovascular unit: key functions and signaling pathways. *Nat Neurosci*, *19*(6), 771-783. https://doi.org/10.1038/nn.4288

Tan, A. C., Ashley, D. M., López, G. Y., Malinzak, M., Friedman, H. S., & Khasraw, M. (2020). Management of glioblastoma: State of the art and future directions. *CA Cancer J Clin*, *70*(4), 299-312. https://doi.org/10.3322/caac.21613

Tesileanu, C. M. S., et al. (2020). Survival of diffuse astrocytic glioma, IDH1/2 wildtype, with molecular features of glioblastoma, WHO grade IV: a confirmation of the cIMPACT-NOW criteria. *Neuro Oncol*, *22*(4), 515-523. https://doi.org/10.1093/neuonc/noz200

Thakkar, J. P., et al. (2014). Epidemiologic and molecular prognostic review of glioblastoma. *Cancer Epidemiol Biomarkers Prev*, *23*(10), 1985-1996. https://doi.org/10.1158/1055-9965.Epi-14-0275

Thanabalasundaram, G., Pieper, C., Lischper, M., & Galla, H. J. (2010). Regulation of the blood-brain barrier integrity by pericytes via matrix metalloproteinases mediated activation of vascular endothelial growth factor in vitro. *Brain Res*, *1347*, 1-10. https://doi.org/10.1016/j.brainres.2010.05.096

Thanabalasundaram, G., Schneidewind, J., Pieper, C., & Galla, H. J. (2011). The impact of pericytes on the blood-brain barrier integrity depends critically on the pericyte differentiation stage. *Int J Biochem Cell Biol*, *43*(9), 1284-1293. https://doi.org/10.1016/j.biocel.2011.05.002

Thomas, W. E. (1999). Brain macrophages: on the role of pericytes and perivascular cells. *Brain Res Brain Res Rev*, *31*(1), 42-57. https://doi.org/10.1016/s0165-0173(99)00024-7

Tomer, R., Ye, L., Hsueh, B., & Deisseroth, K. (2014). Advanced CLARITY for rapid and high-resolution imaging of intact tissues. *Nat Protoc*, *9*(7), 1682-1697. https://doi.org/10.1038/nprot.2014.123

Tucha, O., Smely, C., Preier, M., & Lange, K. W. (2000). Cognitive deficits before treatment among patients with brain tumors. *Neurosurgery*, *47*(2), 324-333; discussion 333-324. https://doi.org/10.1097/00006123-200008000-00011

Uemura, A., et al. (2021). VEGFR1 signaling in retinal angiogenesis and microinflammation. *Prog Retin Eye Res*, *84*, 100954. https://doi.org/10.1016/j.preteyeres.2021.100954

Verhaak, R. G., et al. (2010). Integrated genomic analysis identifies clinically relevant subtypes of glioblastoma characterized by abnormalities in PDGFRA, IDH1, EGFR, and NF1. *Cancer Cell*, *17*(1), 98-110. https://doi.org/10.1016/j.ccr.2009.12.020

Vredenburgh, J., et al.. (2007). Bevacizumab plus irinotecan in recurrent glioblastoma multiforme. *J Clin Oncol*, *25*(30), 4722-4729. https://doi.org/10.1200/jco.2007.12.2440

Weller, M., et al. (2017). European Association for Neuro-Oncology (EANO) guideline on the diagnosis and treatment of adult astrocytic and oligodendroglial gliomas. *Lancet Oncol*, *18*(6), e315-e329. https://doi.org/10.1016/s1470-2045(17)30194-8

Wesseling, P., Ruiter, D. J., & Burger, P. C. (1997). Angiogenesis in brain tumors; pathobiological and clinical aspects. *Journal of Neuro-Oncology*, *32*(3), 253-265. https://doi.org/10.1023/A:1005746320099

Winkler, E. A., Bell, R. D., & Zlokovic, B. V. (2010). Pericyte-specific expression of PDGF beta receptor in mouse models with normal and deficient PDGF beta receptor signaling. *Mol Neurodegener*, *5*, 32. https://doi.org/10.1186/1750-1326-5-32

Winkler, E. A., Bell, R. D., & Zlokovic, B. V. (2011). Central nervous system pericytes in health and disease. *Nat Neurosci*, *14*(11), 1398-1405. https://doi.org/10.1038/nn.2946

Wirsik, N. M., et al. (2021). TGF-beta activates pericytes via induction of the epithelial-to-mesenchymal transition protein SLUG in glioblastoma.

Neuropathol Appl Neurobiol, *47*(6), 768-780. https://doi.org/10.1111/nan.12714

Xiao, Q., Yang, S., Ding, G., & Luo, M. (2018). Anti-vascular endothelial growth factor in glioblastoma: a systematic review and meta-analysis. *Neurological Sciences*, *39*(12), 2021-2031. https://doi.org/10.1007/s10072-018-3568-y

Xu, J., Lamouille, S., & Derynck, R. (2009). TGF-beta-induced epithelial to mesenchymal transition. *Cell Res*, *19*(2), 156-172. https://doi.org/10.1038/cr.2009.5

Yamada, N., et al. (1995). Enhanced expression of transforming growth factor-beta and its type-I and type-II receptors in human glioblastoma. *Int J Cancer*, *62*(4), 386-392. https://doi.org/10.1002/ijc.2910620405

Yang, H. W., Menon, L. G., Black, P. M., Carroll, R. S., & Johnson, M. D. (2010). SNAI2/Slug promotes growth and invasion in human gliomas. *BMC Cancer*, *10*, 301. https://doi.org/10.1186/1471-2407-10-301

Yi, Y., Hsieh, I. Y., Huang, X., Li, J., & Zhao, W. (2016). Glioblastoma Stem-Like Cells: Characteristics, Microenvironment, and Therapy. *Front Pharmacol*, *7*, 477. https://doi.org/10.3389/fphar.2016.00477

Yushchenko, D. A., & Schultz, C. (2013). Tissue clearing for optical anatomy. *Angew Chem Int Ed Engl*, *52*(42), 10949-10951. https://doi.org/10.1002/anie.201306039

Zhang, X. N., et al. (2021). Pericytes augment glioblastoma cell resistance to temozolomide through CCL5-CCR5 paracrine signaling. *Cell Res*, *31*(10), 1072-1087. https://doi.org/10.1038/s41422-021-00528-3

Zhang, Z. S., Zhou, H. N., He, S. S., Xue, M. Y., Li, T., & Liu, L. M. (2020). Research advances in pericyte function and their roles in diseases. *Chin J Traumatol*, *23*(2), 89-95. https://doi.org/10.1016/j.cjtee.2020.02.006

Zhou, W., et al. (2017). Targeting Glioma Stem Cell-Derived Pericytes Disrupts the Blood-Tumor Barrier and Improves Chemotherapeutic Efficacy. *Cell Stem Cell*, *21*(5), 591-603.e594. https://doi.org/10.1016/j.stem.2017.10.002

11 Acknowledgement

I would like to take this opportunity to express my gratitude to all the people who supported and accompanied me during the course of my work.

My special thanks go to Ulrike Naumann, who not only gave me the opportunity to do my doctoral research in her department, but also supported me whenever I needed it. Thank you very much!

Furthermore, I would like to thank Dr. Andreas Mack and Ulrich Mattheus, our cooperation partners, for their assistance and the excellent collaboration.

Moreover, thanks also to Olga Oleksiuk for her support and great advice.

In addition, I would like to thank all the members of the neurooncology research group with whom I was lucky to work together during the course of my work, you were a really great team! Many heartfelt thanks especially to Ali El-Ayoubi, whom I could always turn to no matter what, and of course Katja Regel for the great work she contributed to this project.

Apart of that, I would also like to express my appreciation to the IZKF doctoral program at the University of Tübingen for their ideal and financial support.

Last but not least, special thanks to my family and my friends who always believed in me and supported me unconditionally. I am very grateful to have you in my life!